Characterization of Hydrogen and Helium Implanted Silicon Carbide

by

Jacques Herman O'Connell

Submitted in partial fulfilment of the requirements for the degree

Magister Scientiae

in the Faculty of Science at the Nelson Mandela Metropolitan University

Supervisor: Prof. J.H. Neethling January 2009

ACKNOWLEDGEMENTS

My sincere thanks to the following people and organisations:

- My supervisor, Professor J.H. Neethling for his guidance and encouragement throughout this project.

- All of the staff and students from the NMMU Physics department who helped me in any way, both with my work and for their encouragement and stimulating conversation.

- My family and friends for their continual support and encouragement.

- SANHARP for financial assistance.

- PBMR Company for financial assistance.

- NovaSiC for supplying the SiC used in the study.

- CORE for the ion implantation of the SiC.

LIST OF ABBREVIATIONS

Abbreviation	**Meaning**
AFM	Atomic Force Microscope
appm	Atomic Parts Per Million
at. %	Atomic Percent
BF	Bright Field
BSE	Back Scattered Electrons
CVD	Chemical Vapour Deposition
DPA	Displacements Per Atom
fcc	Face Centred Cubic
FIMA	Fissions per Initial Metal Atom
HTR	High Temperature Reactor
HTTR	High Temperature Test Reactor
IPyC	Inner Pyrolytic Carbon
keV	Kilo Electron Volt
MeV	Mega Electron Volt
MPBR	Modular Pebble Bed Reactor (PBMR)
OPyC	Outer Pyrolytic Carbon
PBMR	Pebble Bed Modular Reactor
SAD	Selected Area Diffraction
SE	Secondary Electron
SEM	Scanning Electron Microscope
SIMS	Secondary Ion Mass Spectroscopy
TEM	Transmission Electron Microscope
TRISO	Tri-Isotropic
wt. %	Weight Percent

SUMMARY

This dissertation focuses on the characterization of hydrogen implanted 3C-SiC and helium implanted 6H-SiC and the interaction of silver and palladium with the SiC. The main technique used for the analysis of the implanted SiC was transmission electron microscopy (TEM), although scanning electron microscopy (SEM) and nanoindentation hardness testing were also used. Both H and He implantations were done at an ion energy of 100 keV and the total dose for both species was 10^{17} ions/cm^2. Specimens were annealed at 1000 °C for 20 min in an inert atmosphere.

The observed depth of ion damage agreed closely with that predicted by TRIM 2008. The damaged region in the He implanted specimens had a high density of small bubbles but no cracks were observed. Severe cracking was observed along the damaged region in the H implanted specimens. A second phase hexagonal (4H-SiC) was detected in two grains in the 3C-SiC and some grown in voids were also observed.

The wettability of SiC by a 2:1 by volume mixture of Ag and Pd is extremely low but is significantly increased through the addition of Si to the mixture. The Si containing metal mixture was found to migrate along the grain boundaries of polycrystalline 3C-SiC while sealing the point of entry. Pd attacks SiC and severe etching was observed on the surface of 6H-SiC. An epitaxially orientated Pd_2Si inclusion was observed in the 6H-SiC.

No effect of implantation damage on the interaction of Pd and Ag with SiC was observed. Pd etched the surface of the He implanted 6H-SiC down through the damaged region with no evidence of implantation damage left after 67 hours of annealing and thus no conclusions could be drawn. The metal mixture interacted with the non implanted surface of the H implanted 3C-SiC after dissolving the Si substrate and therefore the effect of the ion damage on the interaction could not be investigated.

Nanoindentation hardness measurements showed a marked increase in hardness of He implanted 6H-SiC annealed for 20 min at 1000 °C over that of as implanted and virgin material. There was also a large decrease in hardness corresponding to the depth of the ion damage.

TABLE OF CONTENTS

CHAPTER ONE

INTRODUCTION

SiC is an important material for use in future semiconductor applications due to its high thermal conductivity, high bandgap of ≈ 3 eV and high saturation velocity of electrons (Nagasawa *et al*. (2002)). Its high hardness also makes it well suited as a cutting material and because of its excellent radiation and temperature resistance it is used in the Tri-Isotropic (TRISO) coating of high temperature reactor (HTR) fuel (Helary *et al.* (2006)) and has also been suggested as a cladding material for the inner walls of future fusion reactors (McDonnel Douglas Aerospace Team (1992)). The use of SiC in TRISO coatings is of particular interest since South-Africa has embarked on development and marketing of fourth generation Pebble Bed Modular Reactors (PBMR). The PBMR is a high temperature, helium cooled; nuclear reactor which employs TRISO coated UO_2 fuel as shown in Fig. 1.1.

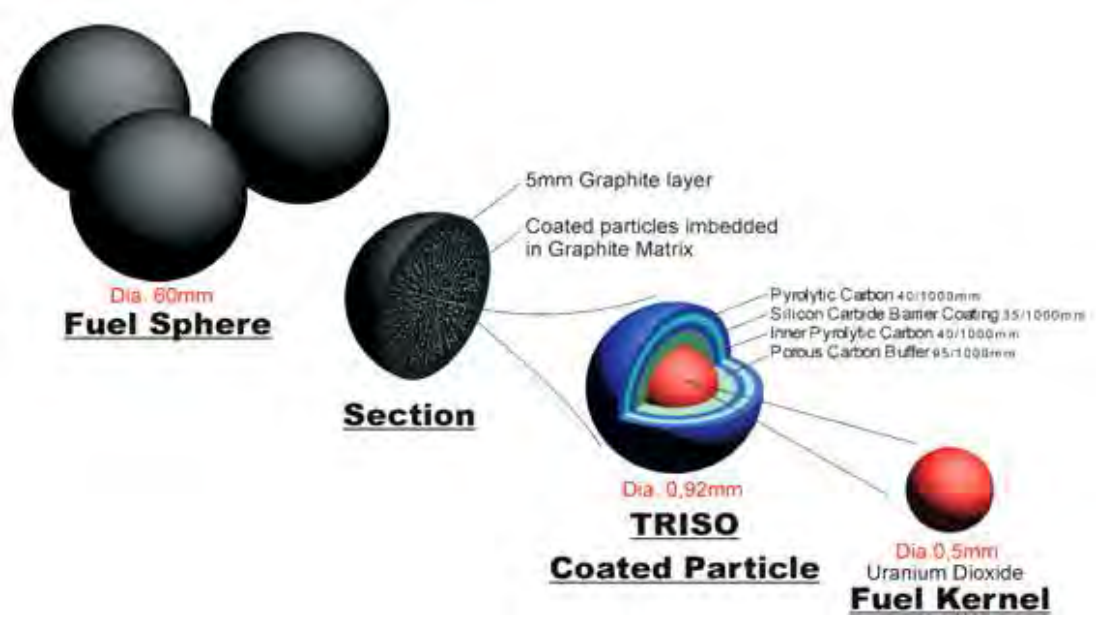

Fig. 1.1. Schematic representation of the TRISO fuel particle employed in the PBMR design (www.pbmr.co.za).

The fuel consists of a UO_2 kernel covered by a layer of porous pyrolytic carbon in order to provide void space for gaseous fission products as well as to accommodate kernel swelling at high operating temperatures. Covering this layer is a layer of dense pyrolytic carbon called the inner pyrolytic carbon (IPyC) which gives structural support to a layer of SiC around it. The SiC is the main barrier against fission product release and its performance for extended periods under high temperature and neutron fluxes is of critical importance if the fuel design is to be effective. The final coating layer is again high density pyrolytic carbon called the outer pyrolytic carbon (OPyC) and also serves as structural support for the underlying SiC. Since the SiC acts as the main fission product barrier it is important to understand the material's behaviour under irradiation with respect to microstructural changes.

It has been demonstrated by numerous authors such as Nabielek *et al*. (2001) and Pearson *et al*. (1982) that some of the metallic fission products such as Ag are released by the particles at high temperatures. The release of ^{110m}Ag is a major problem since it plates the inside of the reactor and turbines and because of its radioactivity severely complicates and increases the cost of maintenance and repair work on these parts. It is the aim of this work to investigate the effect that high doses of H and He ions has on the microstructure if SiC as well as the transport of Pd and Ag through SiC. H and He are produced inside the SiC by neutron transmutation and may compromise the structural integrity of SiC leading to the release of metallic fission products.

Polycrystalline 3C-SiC was implanted with 100 keV H^+ ions and single crystalline 6H-SiC was implanted with 100 keV He^+ ions and their microstructure after implantation as well as consequent annealing at 1000 °C was investigated using transmission electron microscopy (TEM). Nanoindentation hardness measurements were taken from unimplanted, as implanted and implanted and annealed 6H-SiC to determine the effect of implantation on the hardness of the material. Finally a 2:1 by volume mixture of Ag and Pd powders respectively was annealed for 67 hours at 1000 °C on the surface of both implanted and unimplanted 3C-SiC and 6H-SiC in order to investigate the effect of ion implantation on the transport of these metals through the material. The results of these experiments are presented in Chapter 6 and conclusions are presented in Chapter 7.

CHAPTER TWO

REVIEW OF LITERATURE ON SiC

2.1 Introduction

In this chapter, a brief overview of the crystal structure, defects and physical properties of SiC and in particular the 3C and 6H polytypes of SiC is presented. The description of defects is limited in detail and the aim is only to provide sufficient background in order for the reader to fully understand the discussion of experimental results presented later in the text. The chapter concludes with a review of previous work on the behaviour of SiC under irradiation and in particular He and H irradiation as well as a discussion of previous investigations into the transport of various fission products in SiC. Emphasis is placed on Ag and Pd transport through TRISO coatings because of their importance in the nuclear industry. ^{110m}Ag is of great concern in the design of TRISO coated fuel particles and Pd has been shown by various authors to chemically attack SiC.

2.2 The Structure of SiC

Roughly 200 different polytypes of SiC have been reported according to Fisher *et al.* (1990); the only difference between these polytypes lie in the way in which the Si-C close packed planes are stacked as explained by Jepps *et al.* (1983), Pirouz *et al.* (1993) and Shaffer (1968). Of these polytypes, the most commonly found are the 3C, 4H, 6H and 15R where the number indicates the repetition of the Si-C pair and the letters C, H and R indicates that the structure is either cubic, hexagonal or

rhombohedral respectively. The basic building block of all these polytypes is a covalently bonded tetrahedron consisting of a C atom at each vertex with a Si atom in the middle or vice versa. The nature of the bond between Si and C is not purely covalent but has a slight ionic character because of the difference in electronegativity between Si and C. The result, according to Snead *et al*. (2007), is that the only truly stable compounds are formed at the stoichiometric composition.

Fig. 2.1 shows the four main SiC polytypes as mentioned above with reference to the close packed stacking sequence.

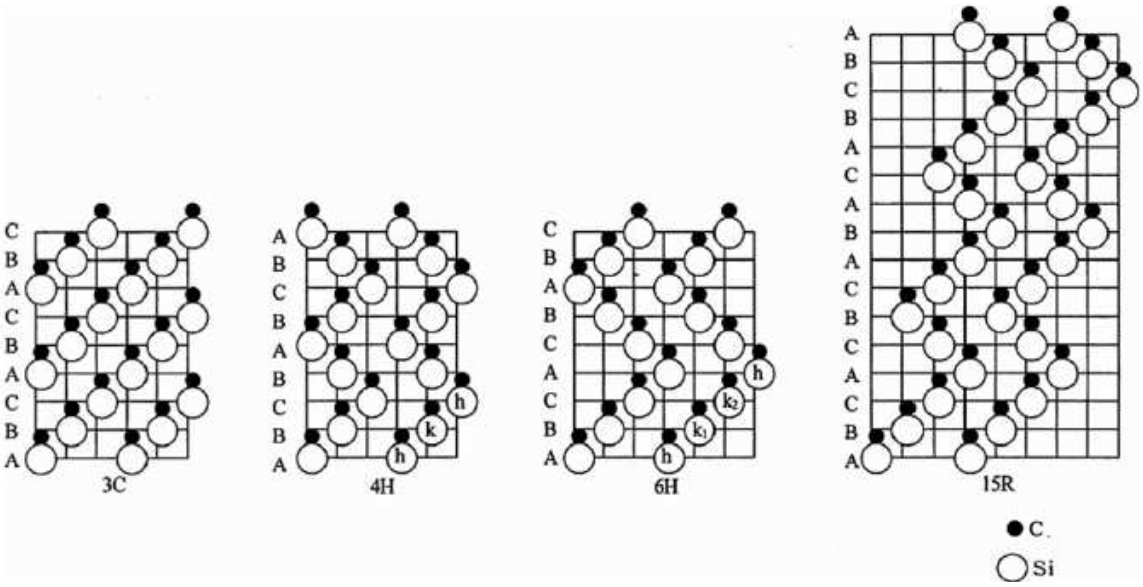

Fig. 2.1. The difference in stacking sequences of the four most common SiC polytypes (Iwami (2001)).

The only polytype to exhibit cubic symmetry is the 3C polytype, also known as β-SiC, the other non-cubic polytypes are all classified as α-SiC. It is evident from Fig. 2.1 that the only difference between the 3C and 6H polytypes is that the order of the B and C layers reverses on every other layer in the 6H stacking sequence whereas they remain constant for all layers of the 3C polytype.

Fig. 2.2 shows 3-dimentional representations of the 3C-SiC and 6H-SiC crystal lattices used in this study. The cubic 3C-SiC crystallizes in the zinc-blende structure

which can be seen as the diamond structure with basis atoms at 000 and $\frac{1}{4}\frac{1}{4}\frac{1}{4}$ except that the C atom at $\frac{1}{4}\frac{1}{4}\frac{1}{4}$ is replaced by a Si atom. The diamond lattice in itself can be considered as two interpenetrating fcc lattices displaced from each other by $\frac{1}{4}\frac{1}{4}\frac{1}{4}$ along the unit cell diagonal (Kittel (1976)). For the 6H-SiC structure, the 6-step stacking sequence is evident from the diagram.

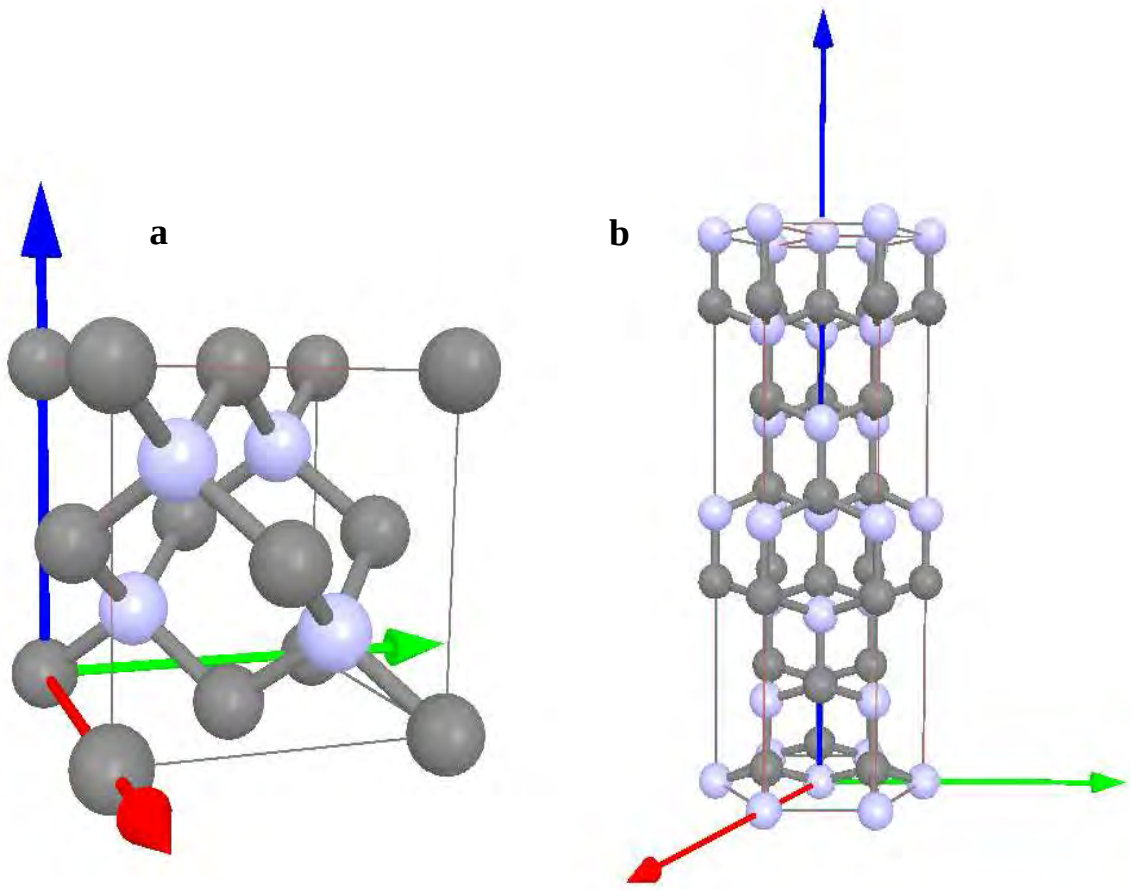

Fig. 2.2. (a) The 3C-SiC unit cell and (b) the 6H SiC unit cell.

The stability of the different polytypes is mainly a function of temperature as shown in Fig. 2.3 and according to Knippenberg (1963), the 3C polytype is more stable than the 6H polytype below 2373 K. There are, however, some authors such as Weltner (1969) and Griffiths (1966) who dispute this conclusion.

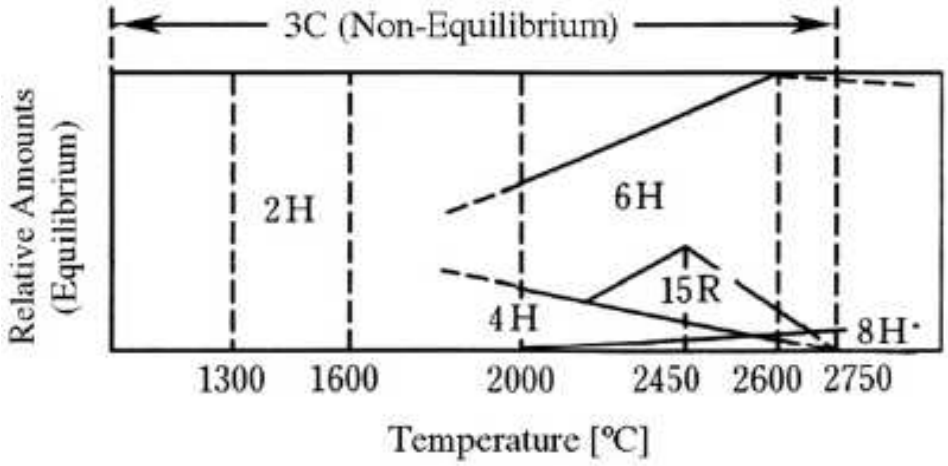

Fig. 2.3. Phase stability diagram of SiC polytypes (Jepps (1983)).

2.3 Point Defects

The simplest form of crystal defect is the point defect generated when the perfect periodicity of the lattice is destroyed through the absence of an atom at a lattice site or the insertion of an extra atom in the lattice. There are three possibilities:

1. Vacancies, produced when an atom is missing and its lattice site is left vacant.

2. Interstitials, produced when extra atoms are inserted into the voids between atoms of the normal lattice.

3. Impurities, produced when a lattice site is occupied by a foreign atom.

Vacancies are sometimes called Shottky defects especially when discussing ionic crystals. The defect pair formed when a displaced atom is forced into an interstitial position is called a Frenkel pair and is of particular importance when discussing radiation damage such as that experienced by materials used in the manufacture of nuclear reactors. When a defect arises from atoms coming from the parent lattice it is termed an intrinsic defect otherwise if the atom in question is an impurity then it is

called an extrinsic defect. Impurity atoms can be either substitutional if they occupy a position normally occupied by an atom in the lattice or they can manifest as interstitial impurities in the voids between lattice atoms. Fig. 2.4 illustrates the difference between a vacancy and an interstitial point defect while Fig. 2.5 shows extrinsic substitutional and interstitial point defects. Defects are present in any real crystal; intrinsic point defects are introduced into crystals by temperature alone. At any temperature T > 0 K, there exists a thermodynamically stable equilibrium concentration of both vacancies and interstitials because of the increase in entropy associated with the way in which these defects distort the lattice.

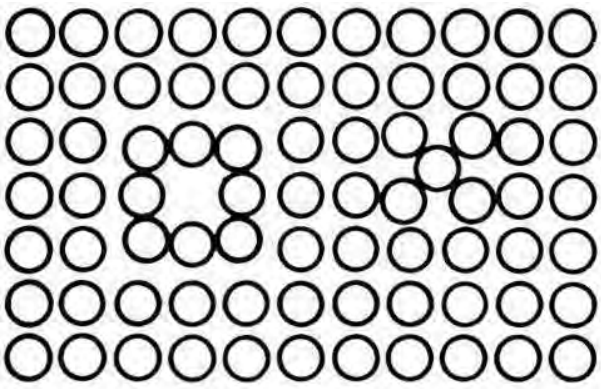

Fig. 2.4. A vacancy (left) and an interstitial (right) defect (Hull et al. (1984)).

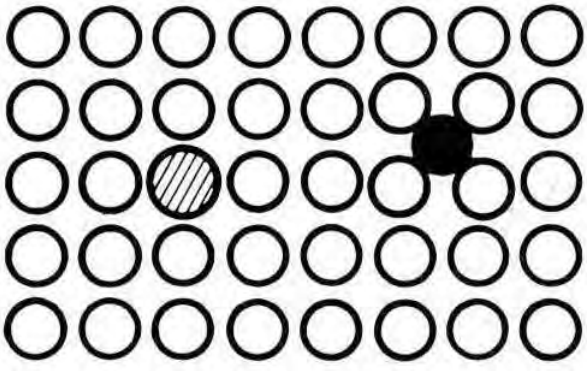

Fig. 2.5. Extrinsic substitutional (left) and interstitial (right) defects (Hull et al. (1984)).

The change in free energy, ΔF, associated with the introduction of n vacancies or interstitials into a crystal is given by Hull *et al*. (19984) as

$$\Delta F = nE_f - T\Delta S \qquad \ldots(2.1)$$

where E_f is the energy of formation of one defect and ΔS is the change in entropy of the crystal. The quantity nE_f is thus relatively large and positive but it is offset by the increase in configurational entropy as a result of the defects. The equilibrium fraction of defects for a minimum energy is thus given by

$$n_{eq} = n_t \exp\left(-\frac{E_f}{kT}\right) \qquad \ldots(2.2)$$

where n_t is the total number of atomic sites and k is Boltzmann's constant. For a vacancy, E_f^v is the energy required to remove one atom from the lattice and place it on the surface of the crystal. According to Hull *et al*. (1984), this energy is roughly two to four times less than E_f^i, the energy required to take an atom from the surface of the crystal and place it into an interstitial site. The result is that at any given temperature the equilibrium concentration of vacancies is substantially larger than that of interstitials.

2.4 Point Defect Diffusion

The atoms in a crystal are not stationary but vibrate around their respective lattice sites due to thermal excitation. On average these vibrational amplitudes are small and the atom's energy remains well below the energy required to jump into a different lattice position (activation energy). Occasionally however, an atom may gain enough energy through a thermal spike (or collision with a fast particle incident on the crystal) in order to move into a different lattice position. Every vibration of the atom can be seen as an attempt to jump to a different lattice site but this attempt is normally unsuccessful due to the relatively high activation energy required. The frequency of atomic jumps according to Girifalco (1964), may thus be represented by the product

of the frequency of vibration of the atom in question and the probability that the atom has energy higher than E^*, the activation energy

$$\Gamma = \nu p \qquad \ldots.(2.3)$$

where Γ is the atomic jump frequency, ν is the atomic vibration frequency and p is the probability that the atom has energy greater than E^*. The probability p can be calculated through statistical mechanical considerations if E^* is known (Girifalco (1964)) and the atomic jump frequency can thus be expressed as

$$\Gamma = \nu e^{-E^*/kT} \qquad \ldots(2.4)$$

The jump frequency indicates how often atoms will leave their original positions but does not indicate in which direction motion will occur. Since the time that an atom spends at any given site is long compared to the atomic vibrational frequency, the atom completely equilibrates with its new surroundings before moving on and the direction of the next jump is thus random. This path is said to constitute a random walk; since a particular jump has no correlation with a previous jump, the motion is said to be uncorrelated. However, not all random walks are uncorrelated. For example, the motion of a substitutional impurity that jumps through a vacancy mechanism needs a vacancy alongside it in order to jump. For the motion to be uncorrelated, all sites alongside the atom after the jump must have an equal probability of being vacant. Clearly this is not so since the vacancy will now reside in the atom's original place and thus its random walk is correlated.

Since atoms move through crystals via random walks, if the crystal contains a high concentration of impurity atoms located in a specific area of the crystal, these impurity atoms will eventually disperse throughout the crystal by means of random walks until eventually there is an equal concentration of impurity atoms throughout the crystal. Mass transport thus occurs spontaneously from a high to low concentration region. Fick's first law of diffusion relates this flux of matter from high to low concentration to the concentration of the species of interest. Mathematically, this law is expressed as follows

$$J = -D\frac{\partial C}{\partial x} \qquad \ldots(2.5)$$

Here J is the flux of matter across an imaginary boundary between the high and low concentration areas, D is the diffusion coefficient and C is the concentration of the species in question. The flux is thus proportional to the negative of the concentration gradient, the negative implying that the flow of matter is in the direction from high to low concentration. D is highly dependent on temperature and is also a function of the diffusing species as well as the material through which it diffuses. This equation holds for all types of diffusion, even in liquids and gasses although D would be different in each case. In particular, the definition of D for vacancy diffusion must include the probability of a vacancy being present at the initial position.

A more useful equation however, is Fick's second law of diffusion. This law is expressed as (Girifalco (1964))

$$\frac{\partial C}{\partial t} = D\frac{\partial^2 C}{\partial x^2} \qquad \ldots(2.6)$$

Here, $C(t)$ is the concentration of the species of interest as a function of time. The advantage of this equation lies in that if the concentration is known at some earlier time $t = 0$, then the concentration at a later time can be calculated provided that the diffusion coefficient D is known. If the concentration can be experimentally determined for different times, then D can be calculated from Fick's second law. D itself can be expressed as some constant D_0 which is independent of temperature but dependent on the atomic properties that control diffusion like jump frequency, vacancy mechanism etc. multiplied with an exponential factor illustrating the temperature dependence of D. Thus according to Girifalco (1964)

$$D = D_0 e^{-Q/kT} \qquad \ldots(2.7)$$

where Q has dimensions of energy and D_0 and Q are defined differently for different mechanisms of diffusion. In general, the average distance, $<x>$, that a diffusing species will move into a material, whether the diffusing species is a different material or self interstitials or vacancies, is given by (Casey *et al*. (1975))

$$< x > \approx \sqrt{Dt} \qquad \ldots(2.8)$$

2.5 Definition of Dislocation Line and Burgers Vector

Consider the crystal shown in Fig. 2.6(a). If a cut is made into the crystal and the resulting two sides are pulled apart by a translation vector of the lattice (Fig. 2.6(b)) and the missing material is then filled in (Fig. 2.6(c)), then at the bottom of this plane of "extra" material resides an area of strongly distorted material known as an edge dislocation.

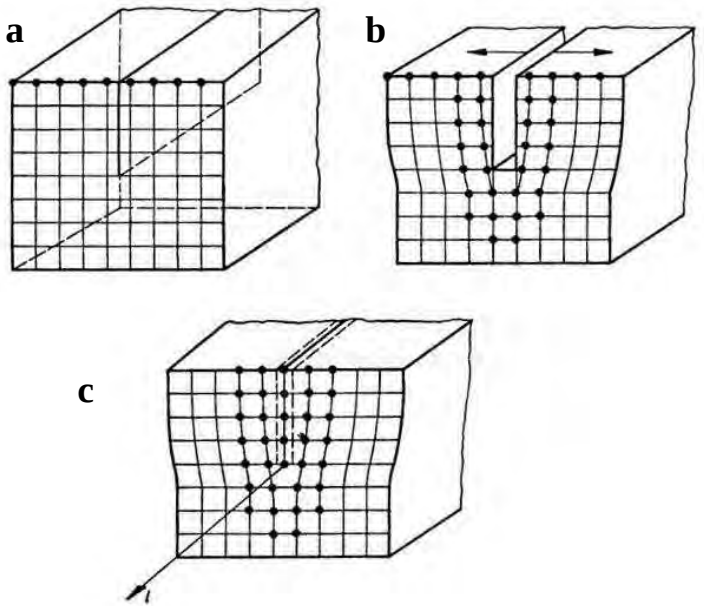

Fig. 2.6. (a) A cut is made in a perfect crystal and the resulting two parts (b) are pulled apart by a translation vector of the lattice. (c) Missing material is added in and the result is an edge dislocation lying along the bottom of the inserted plane. (Bollmann (1970)).

The line of distorted material beneath the extra plane is called the dislocation line. A screw dislocation like the one shown in Fig. 2.7(a-c) is produced when a cut ABCD is made into the crystal and the resulting two sides are sheared apart with a lattice translation vector. Fig. 2.7(d) shows the resulting screw dislocation line with the atom positions around the dislocation forming a structure similar to that of the thread of a screw (hence the name screw dislocation).

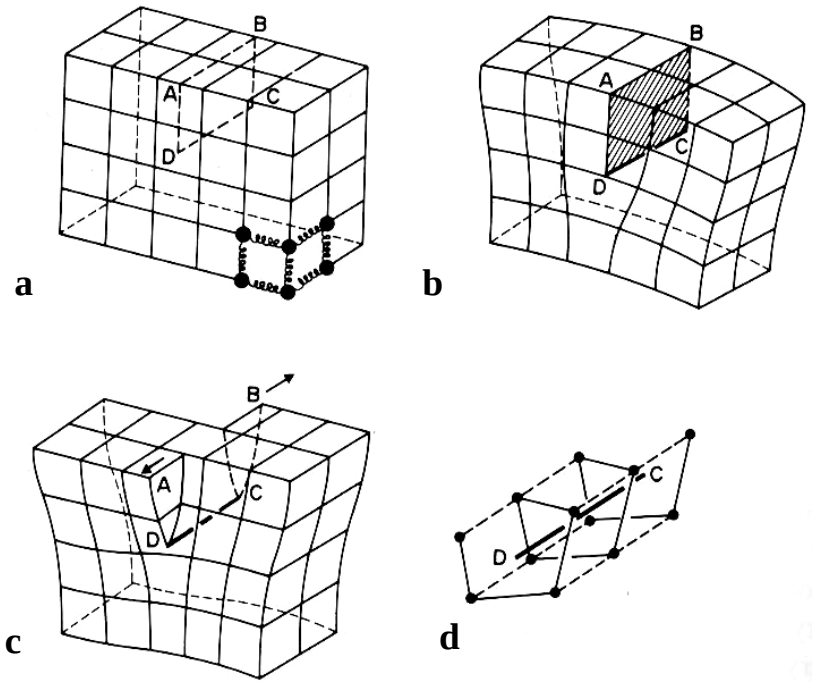

Fig. 2.7. (a) and (b) A cut is made into a perfect crystal and (c) the resulting two sides are sheared apart by a lattice translation vector. (d) The resulting screw dislocation with spiralling atomic planes astound it. (Hull et al. (1984)).

In order to characterise a dislocation, two pieces of information are required.

1. The path of the dislocation line in the crystal.

2. The Burgers vector of the dislocation.

The dislocation line has been defined above and the Burgers vector is an indication of the severity of the dislocation and is defined as follows:

Consider the edge dislocation in Fig. 2.8(a), if one moves around the dislocation in a clockwise manner from M to Q, moving from lattice point to lattice point to form a closed loop and repeat the procedure in a perfect crystal (Fig. 2.8(b)) but only moving by the same number of lattice points then the loop in the perfect crystal will not be closed. The Burgers vector is defined as the vector required to bring the end point of the circuit in the perfect crystal to coincide with the starting point as shown in Fig. 2.8(b). Similarly, a Burgers vector can be defined for a screw dislocation by following the same procedure as shown in Fig. 2.8(c) and (d).

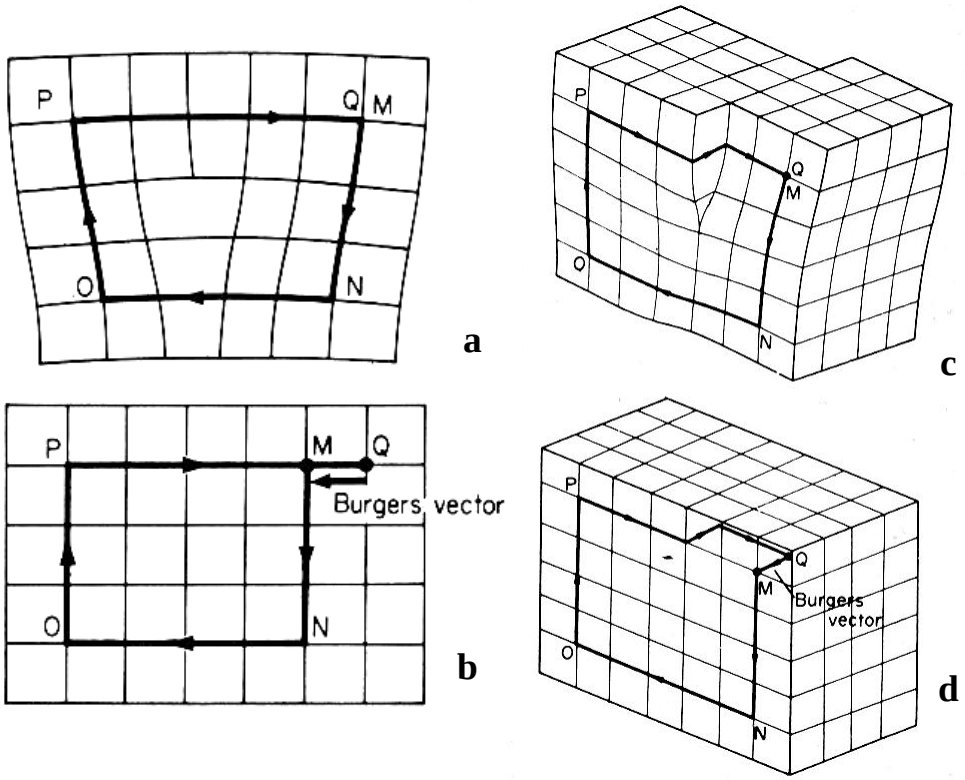

Fig. 2.8. (a) and (c) Burgers circuits in dislocated lattices and their corresponding Burgers circuits in perfect lattices ((b) and (d)) defining the respective Burgers vectors. (Hull et al. (1984)).

From the above it is clear that the dislocation line and Burgers vectors of an edge dislocation are normal to each other while those of a screw dislocation are parallel. In general, dislocations exhibit both edge and screw characteristics and thus have both edge and screw Burgers vector components given by:

- Edge component $b_{edge} = b\sin(\alpha)$
- Screw component $b_{screw} = b\cos(\alpha)$

where α is the angle between the dislocation line $\bar{l}$ and the Burgers vector $\bar{b}$ of the dislocation.

2.6 Movement of Dislocations

Two basic types of motion exist for dislocations (Hull *et al.* (1984)). These are called glide, where the dislocation moves in the surface that contains both the dislocation line and Burgers vector (glide plane), and climb in which the dislocation moves out of the glide plain, normal to the Burgers vector. Glide of many dislocations is called slip and is one of the most common manifestations of plastic deformation in crystals. Fig. 2.9 illustrates the concept of glide. Glide takes place on the {111} close packed planes for fcc and zinc-blende structures and on the {0001} basal planes for the 6H-SiC structure.

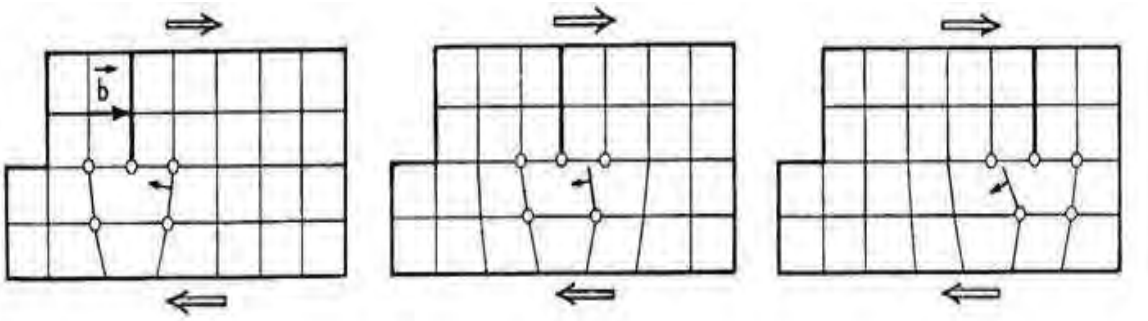

Fig. 2.9. Representation of dislocation glide in a crystal (Bollmann (1970)).

Fig. 2.10 illustrates the concept of dislocation climb by means of ejecting interstitials. It is only possible if the dislocation has an edge component and requires sufficiently high temperatures and stress for the interstitials to diffuse away.

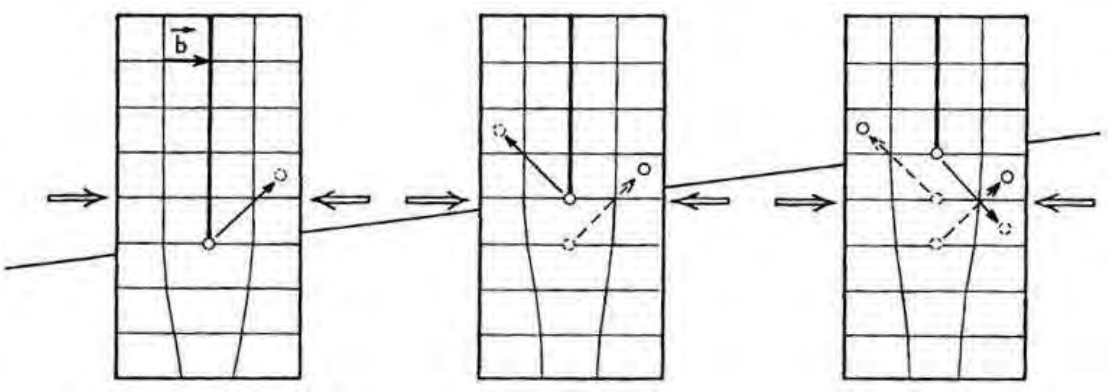

Fig. 2.10. Representation of dislocation climb in a crystal (Bollmann (1970)).

2.7 Stacking Faults

Stacking faults occur when there is a local disruption in the sequence of atomic planes in a crystal. For the zinc-blende structure, the {111} close packed planes have a stacking sequence of ABCABCA… According to the hard sphere model, a close packed layer of atoms resting on an A layer can geometrically rest equally well on a B or C layer. It is thus conceivable that the regular stacking sequence can be locally disrupted for instance: ABCACBABC… Fig. 2.11 shows the two different stacking faults observed in fcc or zinc-blende structures.

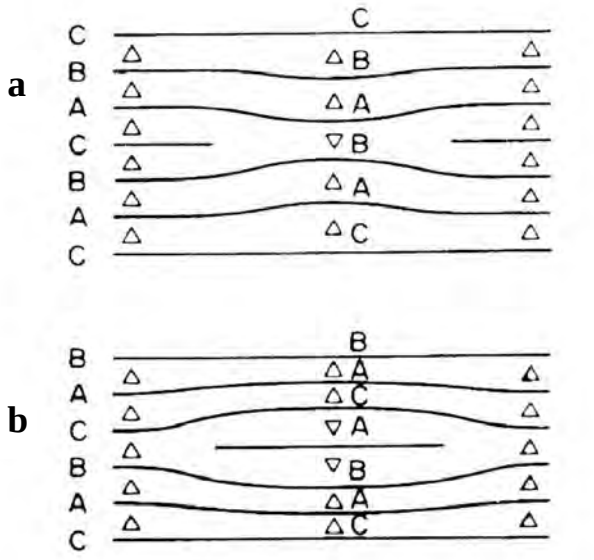

Fig. 2.11. Intrinsic (a) and extrinsic (b) stacking faults in an fcc lattice. (Hull et al. (1984)).

Fig. 2.11(a) demonstrates an intrinsic stacking fault, part of a C layer is removed and the stacking sequences of the remaining top and bottom parts remain continuous up to the fault plane. In Fig. 2.11(b) part of an extra A plane has been inserted into the crystal and the resulting fault is called an extrinsic stacking fault since the extra layer does not belong to the sequence of ether the top or the bottom planes. In a similar way, the ABCACBA… stacking sequence of the {0001} planes of the 6H-SiC crystal structure can also be rearranged through deletion or insertion of crystal planes between existing layers.

2.8 Vacancy and Interstitial Loops

The large number of excess vacancies resulting from quenching a specimen from high temperature may precipitate out in the form of a disc on a close packed plane. If this disc is large enough it may collapse to form a stacking fault (intrinsic) bound by a dislocation. The resulting structure is called a dislocation loop and the Burgers vector of the dislocation is normal to the plane of the loop. This loop is also known as a Frank dislocation loop. This process is depicted below in Fig. 2.12.

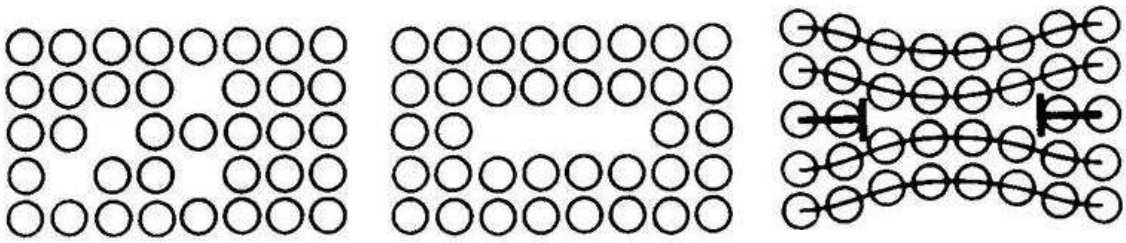

a **b** **c**

Fig. 2.12. Interstitials come together (a) and collect in the form of a disc on a close packed plane (b), if the disc is big enough it may collapse to form a stacking fault bound by a dislocation to form a Frank dislocation loop (c) (Hull et al. (1984)).

Frank dislocation loops may also be formed by the precipitation of interstitials into platelets in the close packed planes. These interstitials may be produced during bombardment with energetic particles. If a cluster of vacancies come together in the

presence of a gas, the resulting disc of vacancies might be prevented from collapsing into a vacancy dislocation loop as a result of the gas pressure inside the void.

2.9 Physical Properties of SiC

2.9.1 Lattice Parameter

Snead *et al.* (2007) has published an extensive list of properties of SiC for use in TRISO fuel particle design and in the following section some of these properties as well as some from other sources will be presented. Table 2.1 shows a list of densities and lattice parameters determined through x-ray diffraction at room temperature for selected SiC polytypes. Note that the *a* values for all polytypes except the 3C are very similar.

Table 2.1. Densities and lattice parameters at room temperature for selected SiC polytypes (Snead et al. (2007))

Polytype	Density (g/cm^3)	Lattice parameter (nm)
2H	3.219	$a = 0.3081$, $c = 0.5031$
3C	3.215	$a = 0.43589$
4H	3.215	$a = 0.3081$, $c = 1.0061$
6H	3.215	$a = 0.3081$, $c = 1.5092$
15R	–	$a = 0.3073$, $c = 3.770$
21R	–	$a = 0.3073$, $c = 5.278$

The lattice parameter of SiC varies very little with temperature which gives it a low thermal expansion coefficient. According to Snead *et al*. (2007), the lattice parameter for β-SiC (in nm) can be expressed as

$$a = 0.43577 + 1.3887 \times 10^{-6} T + 7.8494 \times 10^{-10} T^2 - 2.4434 \times 10^{-13} T^3 \quad \ldots(2.9)$$

where T is temperature in °C. Equation 2.9 has an accuracy of $\pm 2.6\times10^{-5}$ nm. Using equation 2.9 yields a lattice parameter of 0.43580 $\pm 2.6\times10^{-5}$ nm for β-SiC at 20 °C which agrees with the value of 0.43589 nm quoted in Table 2.1. The change in lattice parameter at elevated temperatures thus leads to thermal expansion at elevated temperatures although the thermal expansion coefficient of SiC is rather low.

2.9.2 Hardness

The hardness of SiC is dependent on the fabrication process, impurities and composition according to Snead *et al*. (2007) who lists various hardness measurements such as Vickers, Knoop and nanoindentation hardness reported by various researchers (see Table 2.2). From the table it is evident that for the most part, Vickers and Knoop measurements agree closely while nanoindentation hardness measurements tend to yield higher values. Nanoindentation hardness measurements are extremely sensitive to local variations and surface effects due to the small near surface volumes that are probed. Balog *et al*. (2005) found that nanohardness is generally about 5-7 GPa higher than macrohardness due to factors such as grain boundary phase differences, porosity, indentation size effect and microstructure.

Table 2.2. Various hardness values for different types of SiC (Snead et al. (2007))

Material	Sintering additives	Vickers hardness (GPa)	Knoop hardness (GPa)	Nano hardness (GPa)
Sintered α-SiC[a]	B, C	24.9–26.7	22.4–27.4	n/a
Hot-pressed α-SiC[b]	Al_2O_3, WC, Co	19.3	22.3	n/a
Hot isostatic pressed α-SiC	AlN	25.0–27.3	n/a	n/a
CVD β-SiC[c]	–	20.7–24.5	24.5	32.5–40.6
Sintered β-SiC	B, C	21.1–23.9	20.9	n/a
Hot-pressed β-SiC	Al	26.7–29.7	n/a	n/a
Hot-pressed β-SiC	Al_2O_3, RE_2O_3 (RE = La, Nd, Y, Yb)	3.4–21.2	n/a	n/a

[a] Carborundum Co., Hexoloy-SA.
[b] Norton Co., NC-203.
[c] Morton Advanced Materials (presently Rohm and Haas Advanced Materials).

2.10 Behaviour of SiC Under Irradiation

By using theoretical considerations and comparing to experimental results, Ryazanov *et al*. (2002) demonstrated that neutron irradiation induced swelling of SiC due to point defect accumulation in the matrix may exceed 1% at temperatures below 400 °C. They also observed a monotonous decrease of radiation induced swelling at higher temperatures up to 1200 °C. Heinisch *et al*. (2004) calculated transmutation and activation for SiC irradiated with neutrons for 10 full power years with a total damage accumulation of 4.4 DPA in the Modular Pebble Bed Reactor (MPBR). Significant concentrations of P, H, He, Mg and Be were produced and their concentrations are listed as atomic parts per million (appm) and atomic parts per million per displacements per atom (appm/dpa) in Table 2.3. These transmutants increased linearly over the 10 full power years in the PBMR neutron spectrum. The gasses H and He are of particular concern according to Heinisch *et al*. (2004), since their high mobility could allow them to concentrate at undesirable locations within the microstructure leading to mechanical failure.

Table 2.3. Most abundant transmutants in SiC after 10 full power years of neutron irradiation (Heinisch et al. (2004)).

Element	MPBR	
	appm	appm/dpa
P	36	8.2
H	8.0	1.8
He	5.8	1.3
Mg	3.6	0.8
Be	1.5	0.3

Lebedev *et al*. (1997) found that irradiating (0001) single crystal 6H-SiC with Al^+ ions at elevated temperatures produced a phase change from 6H-SiC to 3C-SiC due to the creation of interstitial loops starting at Al precipitates and terminating at a dislocation. They also found that the Al tends to precipitate epitaxially in the SiC

crystal. Their results were explained in the light of earlier work done on Si by Fedina *et al*. (1986) who claimed that increasing the implantation temperature facilitates the interaction of interstitials with dislocations and enables the interstitial atoms to occupy positions along the dislocation line.

Audren *et al*. (2007) found through Rutherford Backscattering experiments that amorphization of (0001) bulk single crystal 6H-SiC occurred under irradiation at room temperature with 300 keV Cs ions at about 0.25 DPA. Heat treatments revealed that the annealing of the disordered regions between the crystalline and amorphous regions started at about 600 °C but appreciable recrystallization of the amorphous region only started at 1050 °C.

Hasegawa *et al*. (1999) reported on He bubble formation in SiCf/SiC composites under 3 MeV He ion irradiation to a concentration of 10 000 appm at 100 °C and annealing for 1 hour at 1667 K. Sasase *et al*. (2003) found that irradiating (0001) single crystal SiC with 3 MeV He^{2+} ions at 300 K to a fluence of $1x10^{17}$ ions/cm^2 produced a damaged crystalline region within the material with He bubbles with a mean diameter of 2.5 nm. In contrast, Nakata *et al*. (1991) reported that 400 keV He ions with a total fluence of 10^{16} ions/cm^2 produced a buried amorphous layer in 6H-SiC at 300 K. Oliviero *et al*. (2004) also observed amorphization of 4H-SiC (8° off c-axis) implanted with 1.6 MeV He ions to a fluence of $5x10^{16}$ ions/cm^2 at room temperature. At a fluence of $1x10^{17}$ ions/cm^2 they observed 1-2 nm He bubbles in the amorphous region which were either too small to be resolved or not present at the lower fluence. In both cases the amorphous region was bordered by crystalline regions exhibiting dark contrast under TEM observation which they ascribed to high densities of point defects in those regions. Beaufort, *et al*. (2002) reported an amorphous region in 1.6 MeV He^+ implanted (0001) 4H-SiC to a dose of $1x10^{17}$ ions/cm^2 at room temperature. Total recrystallization of the amorphous region occurred after annealing at 1500 °C for 30 min under high vacuum. Annealing also facilitated precipitation of He bubbles in the damaged region. Frangis *et al*. (1996) found diamond crystallites in both the crystalline and amorphous regions of single crystal 6H-SiC implanted at room temperature with 1 MeV He^+ ions to a fluence of $2x10^{17}$ ions/cm^2.

Tong *et al.* (1997) found that implanting 6H-SiC with H ions below 200 °C and annealing above 650 °C produced H filled micro-cracks which eventually led to layer splitting. Jiang *et al.* (2000) investigated damage accumulation in 6H-SiC implanted with 100 keV H_2^+ ions at 100 °C and 300 °C for doses up to $1x10^{17}$ ions/cm^2. They found that thermal recovery of disorder on the Si sublattice proceeded gradually over a wide temperature range. At a fluence of $1x10^{17}$ ions/cm^2, annealing for 20 min at 1070 K resulted in blister formation at a depth corresponding to the H^+ projected range. About 30 % of the H atoms were released form the 100 °C sample after annealing at 1070 K for 20 min.

Tromas *et al*. (2008) reported that for 4H-SiC implanted at room temperature with 50 keV He ions up to $1x10^{17}$ ions/cm^2, the near surface nanohardness was dependent on He fluence tending to decrease with increasing fluence. At high fluences a buried amorphous layer contributed to a "constrained coating" effect in hardness versus depth measurements. At the maximum fluence of $1x10^{17}$ ions/cm^2 a decrease of 50 % in measured hardness was observed. Park *et al*. (2002) implanted polycrystalline β-SiC with 5.1 MeV Si^{2+} and 1.0 MeV He^+ ions at varying fluences and found through microindentation that the unirradiated SiC exhibited the lowest hardness of about 33 GPa. Hardness was found to increase with radiation damage and simultaneous irradiation of Si and He ions was found to enhance the radiation induced hardening effect compared to single Si ion irradiation. They explained their observations by postulating that the irradiation induced point defect clusters and He production acted as barriers for dislocation movements.

2.11 Fission Product Transport Through SiC

Minato *et al*. (1993) annealed irradiated TRISO coated UO_2 particles in the temperature range 1600 °C to 1900 °C in order to monitor the release of various fission products such as ^{137}Cs and ^{110m}Ag. They found that the SiC pressure vessels remained intact during irradiation up to 3.6 % FIMA corresponding to the maximum burnup in the Japanese High Temperature Test Reactor (HTTR), as well as during

post-irradiation heating experiments. Ceramographic observation showed no evidence of palladium attack or thermal decomposition of the SiC layer. ^{137}Cs, ^{134}Cs, ^{110m}Ag, ^{154}Eu and ^{155}Eu were released through the coating layers during post irradiation annealing. The diffusion constants of ^{137}Cs (see equation 2.7) were reported as $D_0 = 2.5\times10^{-2}$ m^2/s and $Q = 503$ kJ/mol. Fractional release measurements suggested that the diffusion coefficient of ^{110m}Ag in SiC is even larger. MacLean *et al*. (2006) implanted CVD grown polycrystalline β-SiC with 93 and 161 MeV Ag ions with peak concentrations of approximately 26 wt. % and annealed specimens for 210 h and 480 h at 1500 °C in order to investigate the migration of Ag in SiC. They observed no Ag migration, neither through the bulk of the SiC crystals nor along grain boundaries. They observed phase separated Ag crystals within the recrystallized regions after annealing. They speculated that the release of silver by TRISO particles could be as a result of vapour transport through microcracks in the SiC coatings that could have been introduced during the fabrication process or generated during the neutron irradiation followed by high temperature annealing. Further support for this argument is given by MacLean (2004) who showed that He leak rates of specially prepared spherical SiC shells increased after heat treatment. Since He leaks can only occur if mechanical paths are present, this gives support to the suggestion that vapour transport might be occurring. Ag release rates from these shells showed the same variability as that from TRISO particles. Nabielek *et al*. (2001) presented Ag release data from several experiments at different temperatures which indicate a significant drop in Ag release below the melting point of Ag. This observation also supports the idea of Ag migration along mechanical paths such as microcracks.

Nabielek *et al*. (1977) also found that ^{110m}Ag is released from TRISO particles above 1200 °C while caesium, strontium, barium and cerium are retained virtually completely up to 1500 °C. They speculated that Ag might form a liquid with free Si at SiC grain boundaries and so propagate through the layer. However, no free Si was detected in the SiC layer up to the detection limit of 0.2-0.3 %. Pearson *et al*. (1982) observed that rare earths, including Pd, migrate through the SiC layers of TRISO particles along grain boundaries. Small metal–Si nodules were observed to move along grain boundaries as shown in Fig. 2.13 while leaving the grains intact.

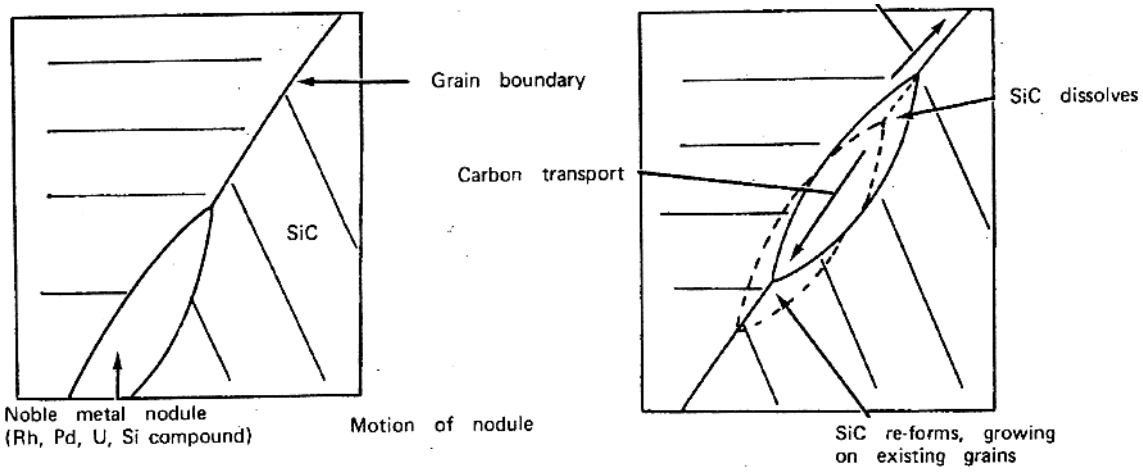

Fig. 2.13. Noble metal transport in SiC TRISO layers (Pearson et al. (1982)).

It was believed that this process occurred by SiC dissolving in the nodule at the leading edge and redepositing at the trailing edge directly on the original material maintaining the same orientation and leaving the original microstructure virtually unchanged. No microstructural changes or Ag transport through SiC was observed after 2000 h annealing. No second phase nodules or grain boundary films of Ag was detected. However, the authors suggested that further STEM investigations of the grain boundaries were needed to confirm this conclusion. Li (1994) investigated the wetting behaviour of monocrystalline α-SiC by liquid Ag in Ar atmosphere in the temperature range from the melting point of Ag to 1430 °C. It was found that below 1130 °C, the contact angle does not significantly change with temperature which indicates the absence of appreciable chemical reactions at the interface. Above this temperature, the contact angle decreased rapidly from 128° to 60° and further temperature increases caused an oscillation in contact angle between 110° and 60°. This behaviour has been attributed to the repeated dissolution of SiC into the metal. Adding 10 at. % Si to the Ag suppressed the dissolution of SiC in the metal and no oscillating behaviour of the contact angle was observed with only a slight decrease in contact angle with increasing temperature. However, it was also shown that the addition of Si to Ag results in a significant reduction in contact angle of the Ag/SiC system. By repeating the experiment with Cu instead of Ag, it was reported that the contact angle of the metal/SiC interface decreased rapidly from 116° to 70° at 1165 °C and above this temperature the Cu continued to spread with the formation if solid SiC at the top of the drop.

Sawa et al. (2004) investigated the interaction of Pd with SiC by measuring the depth of penetration of the resulting intermetallic compound into the SiC layer. They found that the maximum penetration depth depended on the amount of Pd released from the kernel through a cubic root function. Using surface techniques to study the interface formation of Pd deposited on a Si-rich (0001) 6H-SiC single crystal, Veuillen *et al.* (1999) found that Pd reacts with SiC at room temperature to form Pd_2Si at the interface. Annealing the 20 Å layer at 600 °C produced Pd_2Si islands only partially covering the SiC surface. C did not react with the Pd. For a 120 Å thin Pd layer, annealed at 800 °C, the surface became very rough and consisted of high micrometre sized islands of Pd_2Si surrounded by amorphous carbon.

CHAPTER THREE

ION IMPLANTATION AND RADIATION DAMAGE

3.1 Introduction

In this chapter a brief overview of the Lindhard, Sharff and Shiott theory of ion ranges in solids is presented followed by a discussion of the different types of damage cascades that are produced by different implanted ions. A brief overview of the theory of displacement damage developed by Kinchen and Pease is also presented as it illustrates the technique employed by the Stopping and Range of Ions in Matter (SRIM) program used to estimate implanted ion ranges in the present study. The simulation portion of SRIM is known as TRIM and will be referred to throughout the rest of the text.

3.2 Lindhard, Scharff and Schiott (LSS) Theory of Ion Ranges

Ions penetrating a material will be slowed down by two different processes. Elastic collisions, collisions between ions and atomic nuclei, and inelastic collisions between the ions and the electrons around the atoms. The latter is called inelastic since the energy absorbed by the electrons is not returned to the ions or nuclei but released from the system through other means such as photons.

The rate of energy loss with distance, $-\frac{dE}{dx}$, is given by Carter *et al*. (1976) as

$$-\frac{dE}{dx} = N\{S_n(E) + S_e(E)\} \qquad \ldots(3.1)$$

where N is the number of target atoms per unit volume and S_n and S_e are the nuclear and electronic stopping powers respectively. According to Carter *et al*. (1976), the nuclear stopping power S_n can be expressed as

$$S_n = \int T d\sigma \qquad \ldots(3.2)$$

where $d\sigma$ is the differential cross-section and T is the energy transferred during the collision. The electronic stopping power S_e is proportional to the velocity of the ion and thus proportional to $\sqrt{E_k}$, where E_k is the kinetic energy of the ion. From equation 3.1 the total distance travelled by an ion of initial energy E_0 can be expressed as follows (Carter *et al*. (1976))

$$R = \frac{1}{N} \int_0^{E_0} \frac{dE}{S_n(E) + S_e(E)} \qquad \ldots(3.3)$$

The total path length R does not correspond to the range of the ion normal to the implanted surface since a multitude of scattering events prevents to ion from following a straight path. Fig, 3.1 shows the relationship between the range, R, the projected range, R_p, and the associated range, $R_\perp$, perpendicular to the projected range for a single ion track in a solid.

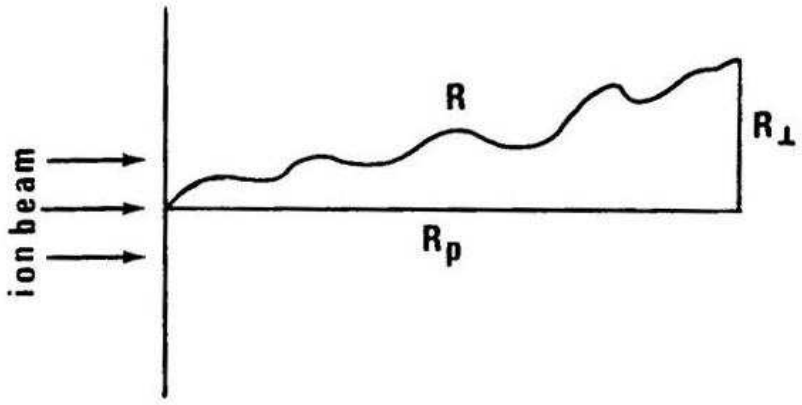

Fig. 3.1. The geometrical interpretation of the ranges R, R_p and $R_\perp$ (Neethling (1980)).

The solving of equation 3.3 is complicated by the need to know the stopping powers *S(E)* for the energy range in question. Calculating stopping powers involve solving equation 3.2 which requires $d\sigma$ which in turn depends on a knowledge of the interatomic potential *V(r)*. In most cases an exact solution of the problem is not possible and one is forced to resort to numerical methods.

In the LSS theory, the interatomic potential is approximated by a Thomas-Fermi statistical model and is of the form (Carter *et al*. (1976))

$$V(r) = \frac{Z_1 Z_2 e^2}{4\pi\varepsilon_0 r}\phi\left(\frac{r}{a}\right) \qquad \ldots(3.4)$$

where $a = a_0(Z_1^{2/3} + Z_2^{2/3})^{-1/2}$, ϕ is the Thomas-Fermi screening function and has been tabulated numerically, and Z_1 and Z_2 are the atomic numbers of the incident ion and struck atom respectively. The function ϕ may be approximated by (Carter *et al*. (1976))

$$\phi\left(\frac{r}{a}\right) = \left\{\frac{\frac{r}{a}}{\left[\frac{r^2}{a} + c^2\right]^{\frac{1}{2}}}\right\} \qquad \ldots(3.5)$$

where $c = \sqrt{3}$ resulting in the best average fit to the Thomas-Fermi potential.

Energies and distances can be expressed in terms of dimensionless parameters ε and ρ where

$$\varepsilon = E\frac{aM_2}{Z_1 Z_2 e^2 (M_1 + M_2)} \qquad \ldots(3.6)$$

and $$\rho = RN4\pi a^2 \frac{M_1 M_2}{(M_1 + M_2)^2} \qquad \ldots(3.7)$$

By using these so called reduced energy and distance parameters, the nuclear stopping power, $S_n = \left\{\frac{d\varepsilon}{d\rho}\right\}_n$, is a function of ε only and therefore independent of incoming particle or stopping substance so that the plot in Fig. 3.2 indicates a universal stopping power. In the same units, the electronic stopping power is given by

$$\left\{\frac{d\varepsilon}{d\rho}\right\}_e = k\varepsilon^{\frac{1}{2}} \qquad \ldots(3.8)$$

where $$k = \xi_e \frac{0.0793 Z_1^{\frac{1}{2}} Z_2^{\frac{1}{2}} (M_1 + M_2)^{3/2}}{(Z_1^{\frac{2}{3}} Z_2^{\frac{2}{3}})^{3/4} M_1^{\frac{3}{2}} M_2^{\frac{1}{2}}} \qquad \ldots(3.9)$$

and $$\xi \approx Z_1^{1/6}$$

Unfortunately, since the parameter *k* depends on the nature of the colliding atoms, a universal curve can not be obtained for electronic stopping power.

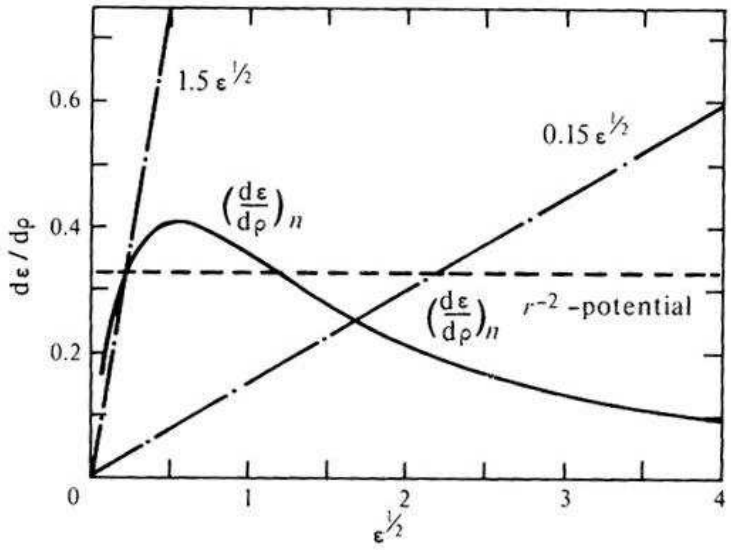

Fig. 3.2. Nuclear and electronic stopping powers in reduced units. Full-drawn curve represents the Thomas-Fermi nuclear stopping power, the dot and dash lines the electronic stopping for k=0.15 and k=1.5. The dashed line gives the nuclear stopping power for the r^{-2} potential (Carter et al. (1976)).

If $Z_1 > Z_2$, k is of the order of *0.1 - 0.2* and only when $Z_1 << Z_2$ does k become greater than unity. The average total path length ρ can now be calculated from

$$\rho = \int_0^{\varepsilon} \frac{d\varepsilon}{S_n(\varepsilon) + S_e(\varepsilon)} \quad \ldots(3.10)$$

Curves of ρ as a function of ε may now be obtained by numerical integration of equation 3.10. Plots of ρ as a function of ε for different values of k are shown in Fig. 3.3. At high energies, $v > \frac{e^2}{h} Z_1^{2/3}$, the ion tends to move in a straight line and only undergoes appreciable angular deflection at the end of its track once its kinetic energy has decreased sufficiently for nuclear stopping to become the dominant factor. Under these situations the average total path length R and the projected range R_p are approximately equal.

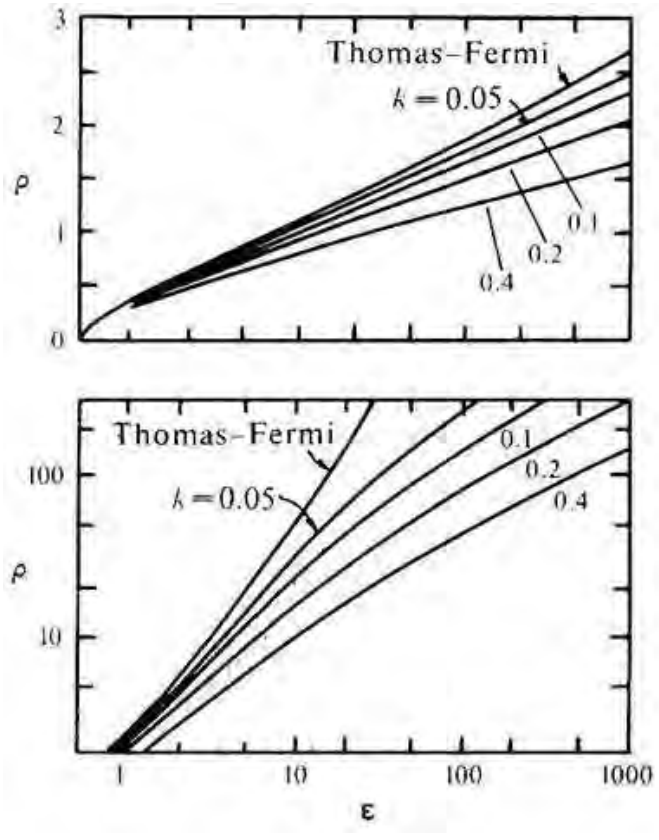

Fig. 3.3. Reduced range-energy plots for various values of k (Carter et al. (1976)).

If R is expressed in μg/cm^2 and E in keV then

$$\rho = R\frac{166M_1}{(Z_1^{2/3} + Z_2^{2/3})(M_1 + M_2)^2} \qquad \ldots(3.11)$$

and $$\varepsilon = E\frac{32.5M_2}{Z_1Z_2(Z_1^{2/3} + Z_2^{2/3})^{1/2}(M_1 + M_2)} \qquad \ldots(3.12)$$

3.3 Defect Production due to Ion Implantation

Following the arguments of the preceding section, it is conceivable that the bombardment of a crystal with energetic ions will lead to damage of the crystal. This damage peaks at the end of the ion track where the probability of displacing atoms from their lattice sites becomes very high. Atoms may be displaced from their lattice sites into interstitial sites resulting in the production of vacancies at the original atom positions. The vacancy-interstitial pair so formed is known as a Frenkel pair. Implanted ions may also come to rest in interstitial sites or they may occupy already vacant sites in the crystal to form substitutional impurities. Displacement damage occurs whenever a lattice atom recoils with energy in excess of some minimum value E_d known as the displacement energy. The displaced atom, called the primary recoil atom, can continue to displace other atoms if it has sufficient energy and this process may continue producing a displacement cascade as long as the energy remains higher than E_d. Carter *et al.* (1976) explains that the main process of energy loss for an implanted ion at high energy is that of electronic excitation of the crystal atoms. At these energies the ion has sufficient energy to penetrate the electron cloud of the matrix atoms and is able to ionize these atoms through Rutherford collisions with their electrons. As the ion loses energy, its degree of ionisation also decreases as it captures electrons from the crystal and it becomes unable to penetrate the electron clouds of the matrix atoms (Kelly (1966)). Collisions now become more like hard sphere collisions between the neutral implanted atom and the matrix atoms and these collisions are responsible for producing atomic displacements. In this region of hard

sphere collisions, the incident ion (now a neutral atom) loses its remaining energy over a relatively short distance since the average distance between collisions approaches that of the interatomic distances.

There is a marked difference in the way in which lattice damage is produced depending on the charge and mass of the ions bombarding the material. The following list describes the main differences between these different types:

1. **Neutron irradiation**

   Neutrons are neutral and thus only interact when colliding elastically with the nuclei of the atoms in the solid. Neutron damage is thus less per unit dose than that of other particles because of the lack of any Coulomb interactions.

2. **Heavy ion irradiation**

   These ions interact with the matrix atoms through knock-on collisions with a transfer of kinetic energy and with the electrons of the solid through ionization and excitation. The stopping cross-section for heavy ions is large with the result that the total range of the ion is comparable to that of the collision cascades produced by the primary recoil atoms.

3. **Light ion irradiation**

   Because of the smaller stopping cross-section of light ions, they generally penetrate much deeper into the material than the individual collision cascades. Only a few atomic displacements occur within cascades with the majority formed as isolated defects along the ion track.

4. **Proton irradiation**

   Proton irradiation represents the extreme case of light ion irradiation. The primary interactions in this form of radiation are long range unscreened Coulomb interactions with little large energy transfer events occurring. According to Nelson (1975), it is unlikely that any amorphization of the target material will occur and most of the defects are created in ones and twos.

5. **Electron irradiation**

   Finally, in the case of electron irradiation the primary recoils have energies just above the displacement energy resulting in well spread out collisions of normally no more than one displaced atom. Kimberling *et al.* (1975) found that 1 MeV electron damage is very similar to 400 keV proton damage.

Fig. 3.4 schematically illustrates the difference in collision events for heavy ions, light ions and electrons. Note the relative depth of penetration compared to that of the collision cascades produced.

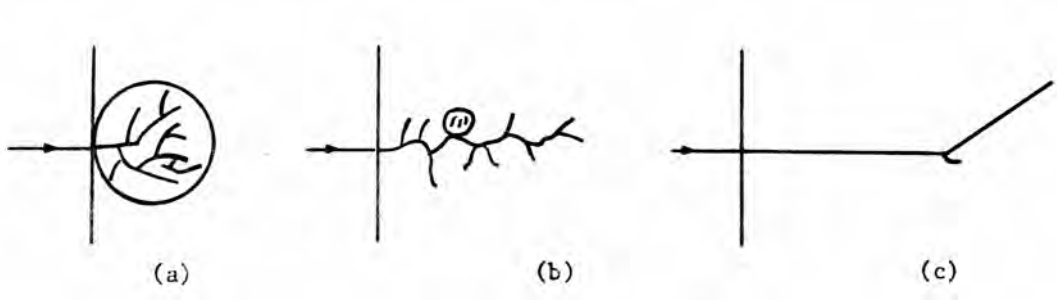

Fig. 3.4. Representation of collision events under irradiation with (a) heavy ions, (b) light ions and (c) electrons (Neethling (1980)).

3.5 Theory of Displacement Damage

A knowledge of the displacement energy, E_d, of a material enables one to determine the minimum energy required by an incident ion in order to produce damage in the crystal. If a hard sphere model is considered and classical, non-relativistic mechanics is used while considering only elastic collisions, then the maximum kinetic energy T that a particle of mass M_1 and kinetic energy E can transfer to a stationary particle of mass M_2 is given by Kelly (1966)) as

$$T = \frac{4M_1M_2}{(M_1 + M_2)^2} E \qquad \ldots(3.13)$$

Therefore the minimum energy E_m required to produce a displacement is given by

$$E_m = \frac{(M_1 + M_2)^2}{4M_1M_2} E_d \qquad \ldots(3.14)$$

In order to approximate the transition from Rutherford scattering to hard sphere scattering, Kinchen and Pease (1955) developed a model that is discussed briefly in the following section. The theory is based on the assumption that the presence of the electron cloud completely cuts off the Coulomb interaction between the nuclei of the ion and stationary atom at a separation distance r_0 given by

$$r_0 = \frac{a_0}{(Z_1^{2/3} + Z_2^{2/3})^{1/2}} \qquad \ldots(3.15)$$

where a_0 is the Bohr radius. Hard sphere collisions are therefore assumed to take place when the ion's kinetic energy becomes less that the Coulomb potential between the moving and stationary nuclei. The kinetic energy, L_A, at which the transition from Rutherford collisions to hard sphere collisions occur is given by

$$L_A = \frac{2E_R Z_1 Z_2 (Z_1^{2/3} + Z_2^{2/3})^{1/2} (M_1 + M_2)}{M_1} \qquad \ldots(3.16)$$

where E_R is the Rydberg energy. Seitz *et al.* (1956) showed that the assumption of Rutherford scattering only holds for scattering angles of the order of b/a where b is the distance of closest approach. Kinchen and Pease assume that collisions occur only if the impact parameter is less than r_0 with a minimum transferred energy of E^* given by

$$E^* = \frac{4E_R^{\,2} Z_1^{\,2} Z_2^{\,2} (Z_1^{2/3} + Z_2^{2/3})^{1/2}}{E} \frac{M_1}{M_2} \qquad \ldots(3.17)$$

Thus at high energies, the incident ion experiences Rutherford collisions where some atoms get displaced. Once the ion's energy falls below L_B, where

$$L_B = 4\frac{E_R^{\ 2}}{E_d^{\ 2}} Z_1^{\ 2} Z_2^{\ 2} (Z_1^{2/3} + Z_2^{2/3}) \frac{M_1}{M_2} \qquad \ldots(3.18)$$

all Rutherford collisions displace atoms. Half of the energy above this threshold value is lost to atoms which receive less than E_d and are therefore not displaced. This energy leads to thermal spikes and is dissipated through lattice vibrations. As the ion loses more energy, the screening effect of the electrons around the atoms become more significant until the colliding atoms behave as hard spheres. Kinchen and Pease defined an energy L_c above which all energy loss is due to electronic excitation and below which all energy loss is due to collisions of the hard sphere type. For an insulator with energy band gap ΔE_g, this energy is given by

$$L_c \approx \frac{1}{4}\frac{M_1}{m_e}\Delta E_g \qquad \ldots(3.19)$$

where m_e is the mass of an electron. According to Kinchen and Pease, a moving atom with $E >> L_B$ and $E >> L_A$ will displace ΔN atoms while losing energy ΔE where

$$\Delta N = P\frac{\Delta E}{E_d}\ , \qquad \ldots(3.20)$$

P is given by $$P = \frac{m_e Z_1 (1 + \ln(\Lambda E / 2E_d))}{4M_1 \left(\frac{Z_{1eff}}{Z}\right)^2 \ln\left(\frac{4m_e E}{M_2 I}\right)}$$

and $$\Lambda = \frac{4M_1 M_2}{(M_1 + M_2)^2}$$

with $I = 8.8Z_2$, the mean ionization potential of the atoms in the solid. If the ions are light, then the total number of atoms displaced, N_d, while slowing down to rest from and initial energy of E may be expressed as

$$N_d = \left(\frac{P(E - L_c) + bL_c}{E_d} \right) \qquad \ldots(3.21)$$

where $b = 0.5$ if $L_B > L_C$ and $b = 0.25$ if $L_B << L_C$. In obtaining these results the solid was treated as a gas with the correct density wherein all atoms receiving energy in excess of E_d were displaced. In real solids the actual structure plays an important role when determining N_d. Kelly (1966) showed that simple displacement models generally over estimate the number of displaced atoms produced.

CHAPTER FOUR

EXPERIMENTAL TECHNIQUES – THEORY AND PRACTICE

4.1 Introduction

In this chapter the reader is presented with a background on the physical principles underlying the different experimental techniques employed during this work. The theory of electron diffraction and image contrast in the transmission electron microscope (TEM) is discussed in great detail in the literature for example Hirsch *et al*. (1965), De Graef (2003) and Eddington (1975) and therefore only a brief overview is presented here followed by a description of the main TEM techniques used in the current investigation. Following this, an overview of the operating principles of the scanning electron microscope (SEM) is presented together with a discussion of energy dispersive x-ray spectrometry (EDX). The chapter concludes with a description of the physical principles governing nanoindentation hardness measurements.

4.2 Transmission Electron Microscope (TEM)

4.2.1 Theory of Electron Diffraction

4.2.1.1 Direct Space Bragg Equation

Fig. 4.1(a) illustrates a planar electron wave incident on atomic planes in a crystal. If one assumes the crystal planes to behave like semi transparent mirrors then part of the

wave will be reflected off the surface of each plane and part of it will be transmitted through the plane towards the lower planes.

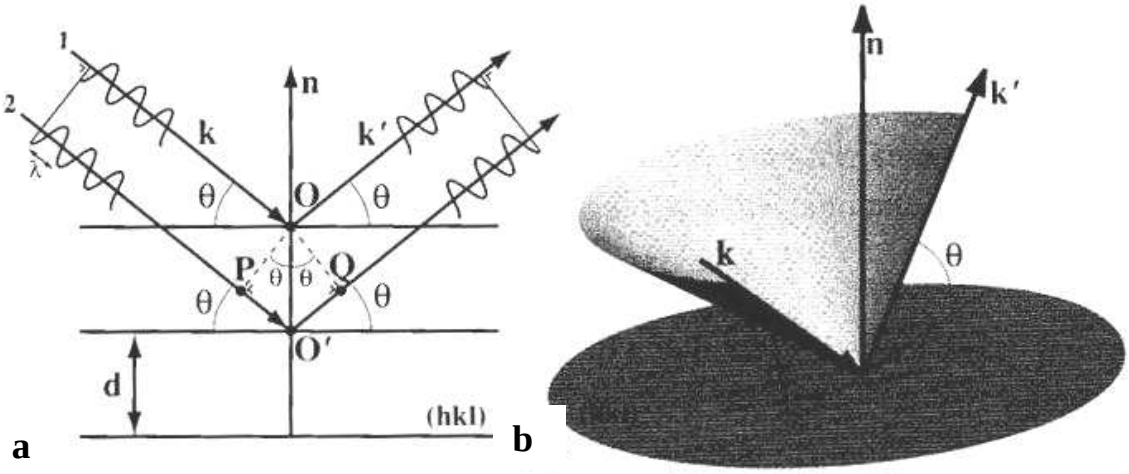

Fig. 4.1. (a) Planar electron waves incident on parallel crystal planes. (b) The incident and diffracted directions together with the crystal plane normal lie in a planar section through a conical surface with its top in the plane. (De Graef (2003)).

For an ideal mirror the angle of reflection is always equal to the angle of incidence Θ. The same reflecting process occurs on the second plane except that the rays travelling to the second plane travel a longer distance than the rays reflected of the top plane. Depending on the interplanar spacing and the electron wavelength, the two waves might interfere constructively or destructively at the observer's position. The path length difference, Δ, between the two rays is given by the sum of the distances *PO'* and *O'Q*. In terms of the interplanar spacing d_{hkl} and the angle Θ

$$\begin{aligned} \Delta &= PO'+O'Q \\ &= d_{hkl}\sin\theta + d_{hkl}\sin\theta \\ &= 2d_{hkl}\sin\theta \end{aligned} \qquad \ldots(4.1)$$

In order for constructive interference to occur, Δ must equal an integral number of wavelengths, that is

$$2d_{hkl}\sin\theta = n\lambda \qquad \ldots(4.2)$$

which is the direct space Bragg equation first derived by Bragg (1915). The integer *n* labels the various diffraction orders for a given set of atomic planes. In practice, the Bragg equation is normally written as

$$2d_{hkl}\sin\theta = \lambda \qquad \ldots(4.3)$$

where *n* has been neglected in favour of considering reflection to take place from planes (nh nk nl) instead of (h k l) planes even if they don't have any atoms on them. The Bragg equation tells us that the incident and diffracted waves must travel in directions which lie on a conical surface with its top in the diffracting plane as shown in Fig. 4.1(b). For all it's simplicity, the Bragg equation in direct space supplies no information about the intensity of the diffracted waves or the direction in which a wave will be diffracted with relation to the crystal orientation. For this reason the use of the direct space Bragg equation is limited to computing the diffraction angle for a given electron wavelength and crystal structure.

4.2.1.2 Reciprocal Space Bragg Equation

In order to address the shortcomings of the direct space Bragg equation it is reformulated in reciprocal space leading to the Ewald sphere construction. According to the de Broglie relation, a plane wave may be represented by its momentum vector $\bar{p} = h\bar{k}$ where $\left|\bar{k}\right| = 1/\lambda$. The wave vector, $\bar{k}$, completely describes the wave with respect to the crystal reference frame and a reciprocal space equivalent of the Bragg equation may be derived since the plane (h k l) may be represented by the vector $\bar{g}_{hkl}$ in reciprocal space. Fig. 4.2(a) shows the incident and diffracted waves from Fig. 4.1(a) represented by their wave vectors $\bar{k}$ and $\bar{k}'$ together with the reciprocal lattice vector $\bar{g}$ representing the diffracting plane. Since a vector may be translated while maintaining its orientation, $\bar{k}'$ may be shifted so that its origin coincides with that of $\bar{k}$ at a point *C* as illustrated in Fig. 4.2(b).

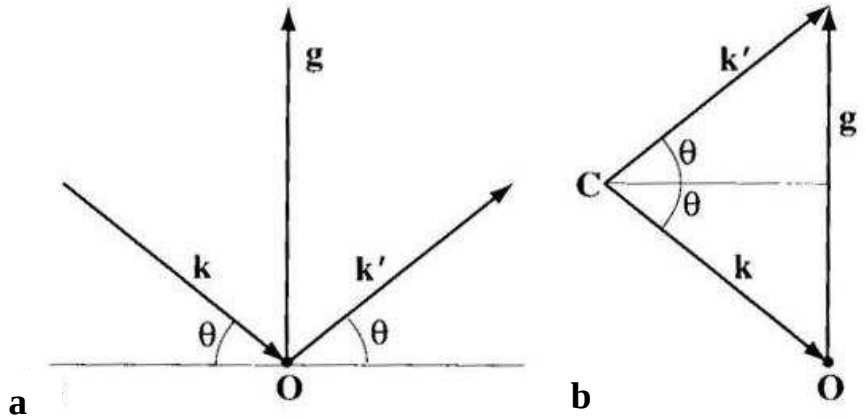

Fig. 4.2. (a) The incident and diffracted wave vectors with reciprocal lattice vector $\bar{g}$ *and (b) the redrawn vector construction (De Graef (2003)).*

The above diagram displays graphically the equation

$$\bar{k}' = \bar{k} + \bar{g} \qquad \ldots(4.4)$$

which, when projected onto the vector $\bar{g}$, yields

$$\begin{aligned} &\bar{k}' \cdot \bar{g} = \bar{k} \cdot \bar{g} + \bar{g} \cdot \bar{g} \\ &\Rightarrow |\bar{k}||\bar{g}| \sin\theta = -|\bar{k}||\bar{g}| \sin\theta + |\bar{g}|^2 \\ &\Rightarrow \frac{\sin\theta}{\lambda} = -\frac{\sin\theta}{\lambda} + \frac{1}{d_{hkl}} \end{aligned} \qquad \ldots(4.5)$$

and is equivalent to the Bragg equation. The Bragg condition is thus satisfied whenever the point *C* falls on the perpendicular bisector plane of the vector $\bar{g}$. The perpendicular bisector plane to the vector $\bar{g}_{hkl}$ consists of all points that are at the same distance from the origin of reciprocal space and the reciprocal lattice point *hkl* which leads to a simple geometric construction for the direction of a diffracted wave when the incident wave vector and crystal orientation are given. Fig. 4.3 shows the Ewald sphere construction for the above mentioned situation. The reciprocal lattice is first drawn originating from a point O. The incident wave vector $\bar{k}$ is then drawn originating from a point C and terminating at O. Point C now becomes the center of a

sphere in reciprocal space (Ewald sphere) with radius $|\bar{k}| = 1/\lambda$ and any reciprocal lattice point falling on the surface of this sphere will satisfy the Bragg condition for diffraction to take place. There may be more than one reciprocal lattice point lying on the sphere (two in this case) and diffraction may take place from all of them. Indeed, the number of reciprocal lattice points that intersect the sphere is further increased for a real specimen since, because the specimen is in the shape of a thin foil with lateral dimensions much larger that its thickness, the reciprocal lattice points elongate into rods leading to a relaxation of the Bragg condition as explained by Hirsch *et al*. (1965).

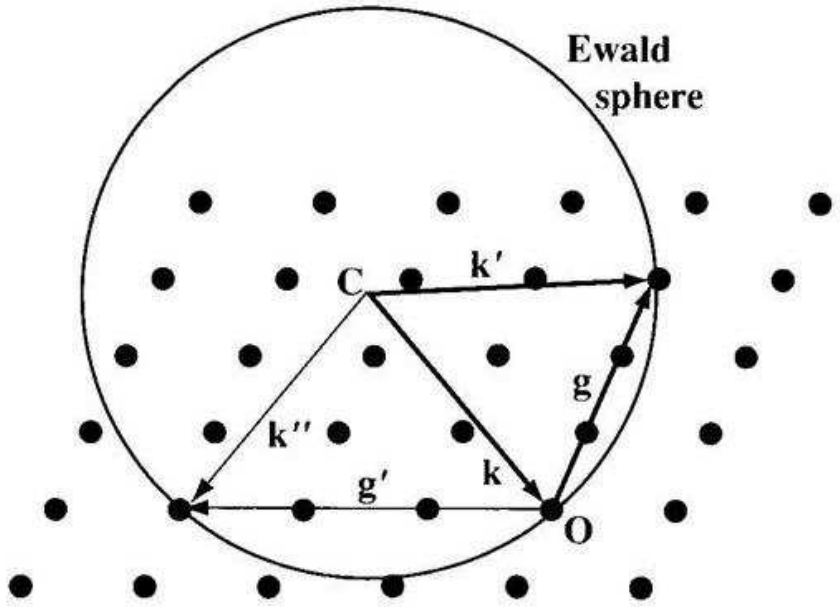

Fig. 4.3. The Ewald sphere construction (De Graef (2003)).

4.2.2 Kinematical Theory of TEM Image Contrast

4.2.2.1 Image contrast in a Perfect Crystal

Hirsch *et al.* (1965) showed that the amplitude of a scattered electron wave exiting the bottom surface of a perfect crystal of thickness *t* is given by

$$\phi_g = \frac{i\pi}{\xi_g}\int_0^t e^{-2\pi isz}dz$$
$$= \frac{i\pi \sin \pi ts}{\xi_g \pi s} e^{-\pi ist} \qquad \ldots(4.6)$$

where *s* is the deviation from the Bragg condition and ξ_g is the extinction distance of the reflection $\bar{g}$ and is related to the wavelength λ and Bragg angle θ by the expression

$$\xi_g = \frac{\pi V \cos\theta}{\lambda F_g} \qquad \ldots(4.7)$$

where F_g is the structure factor of the unit cell and *V* is the volume of the unit cell.

4.2.2.2 Image contrast in an imperfect crystal

Real crystals contain defects such as dislocations which destroy the perfect periodicity of the crystal by displacing certain atoms. Using the same technique as for a perfect crystal, Hirsch *et al*. (1965) showed that the amplitude of a scattered electron wave exiting the bottom surface of an imperfect crystal is given by

$$\phi_g = \frac{i\pi}{\xi_g}\int_0^t e^{-2\pi i\bar{g}\cdot\bar{R}} e^{-2\pi isz}dz \qquad \ldots(4.8)$$

where $\bar{R}$ is the displacement of the unit cell from its proper position. It is evident that a defect will be invisible when $\bar{g}\cdot\bar{R}$ takes on integral values, this leads to the $\bar{g}\cdot\bar{b} = 0$ invisibility criterion for determining the Burgers vector of a dislocation as explained by Edington (1975). Dislocations are usually assumed to be invisible when

$\bar{g} \cdot \bar{b} = 0$ where $\bar{b}$ is the Burgers vector of the dislocation. However, this generally only holds true for screw dislocations where no elastic displacement perpendicular to the slip plane exists. Edge dislocations on the other hand have displacement components parallel and perpendicular to the slip plane and contrast may still be visible even when $\bar{g} \cdot \bar{b} = 0$. In order to ensure complete invisibility, $\bar{g} \cdot \bar{b} \otimes \bar{u} = 0$ must hold where $\bar{u}$ is a unit vector along the positive direction of the dislocation line. By finding the different reflections for which the dislocation becomes invisible, it is possible to determine its Burgers vector.

4.2.3 Image Formation in the TEM

The TEM column typically consists of an electron source at the top of the column together with the required anodes, lenses and apertures to generate a thin monochromatic and coherent electron beam to illuminate the specimen as well as a lens system to magnify and project an image of the specimen onto a phosphorescent screen. Since the electrons in the TEM column move at speeds comparable to the speed of light, it is necessary to consider special relativity when calculating the electron wavelength. The governing equation is of the form (De Graef (2003))

$$\lambda = \frac{h}{\left[2m_0 eE\left(1 + \frac{eE}{2m_0 c^2} \right) \right]^{1/2}} \qquad \ldots(4.9)$$

where λ is in angstrom, h is Planck's constant, m_0 is the electron's rest mass, c is the speed of light and E is the accelerating voltage. The TEM allows one to view both the electron diffraction pattern as well as a magnified image of the specimen itself. Fig. 4.4 shows electron ray diagrams of the part of the column below the specimen for operation in diffraction mode (a) and normal imaging mode (b). The objective lens disperses electrons emerging from the bottom of the specimen to form a diffraction pattern in the back focal plane and recombines them to form an image in the image plain. To see the diffraction pattern on the viewing screen, the intermediate lens

strength is adjusted so that the back focal plane of the objective lens acts as the object plane for the intermediate lens. The diffraction pattern is then projected onto the viewing screen as shown in Fig. 4.4(a). To view an image of the specimen, the intermediate lens strength is adjusted so that its object plane coincides with the image plane of the objective lens. The image is then projected onto the screen as in Fig. 4.4(b). Since the TEM lenses are electromagnetic in nature, electrons tend to spiral down the column. This produces a rotation between the magnified image and diffraction pattern since the two are produced at different lens currents. The angle of rotation required to orient the diffraction pattern correctly relative to the image can be obtained by imaging a specimen of which the orientation of the diffraction pattern relative to the image is known under the same magnification and camera length.

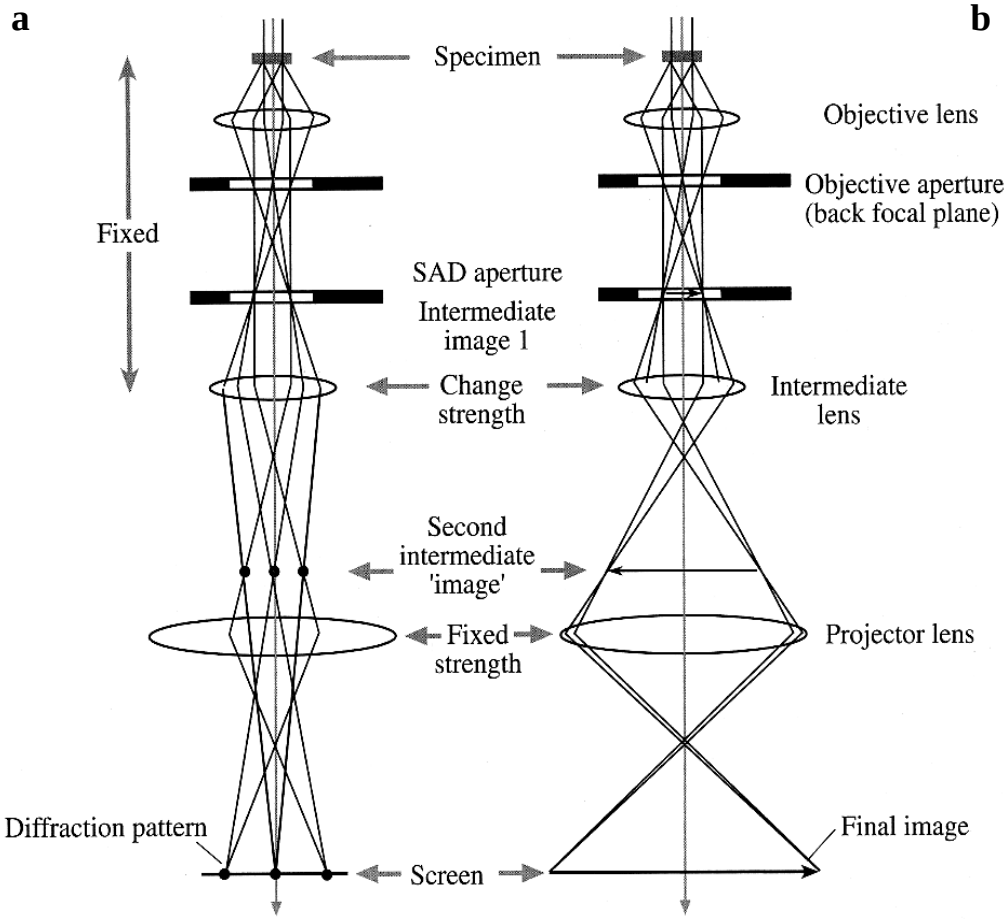

Fig. 4.4. Ray diagrams of a TEM in diffraction mode (a) and imaging mode (b) (Williams and Carter (1996)).

The specimen image is usually observed in bright field (BF) mode. In this mode the objective aperture (see Fig. 4.4) is adjusted to that the transmitted beam is passed

through. The background intensity of the image is high (from where the name bright field) and defects appear darker than the surroundings. Complimentary to this mode of imaging is the dark field (DF) mode where the objective aperture is adjusted to allow through only one of the diffracted beams, the background intensity is low and any feature in the specimen that gives rise to the selected diffracted beam appears bright.

4.2.4 Determination of the Deviation from the Bragg Condition

It is possible to determine the orientation of a crystal in the microscope by making use of the Kukuchi lines present in the diffraction pattern (Edington (1975)). When the exact Bragg condition is satisfied, the *hkl* Kikuchi line will pass through the *hkl* diffracted spot and the $\bar{h}\bar{k}\bar{l}$ Kikuchi line will pass through the origin. The deviation from the exact Bragg condition, *s*, can be calculated by measuring the distance between the bright *hkl* Kikuchi line and its associated diffracted spot as shown in Fig. 4.5.

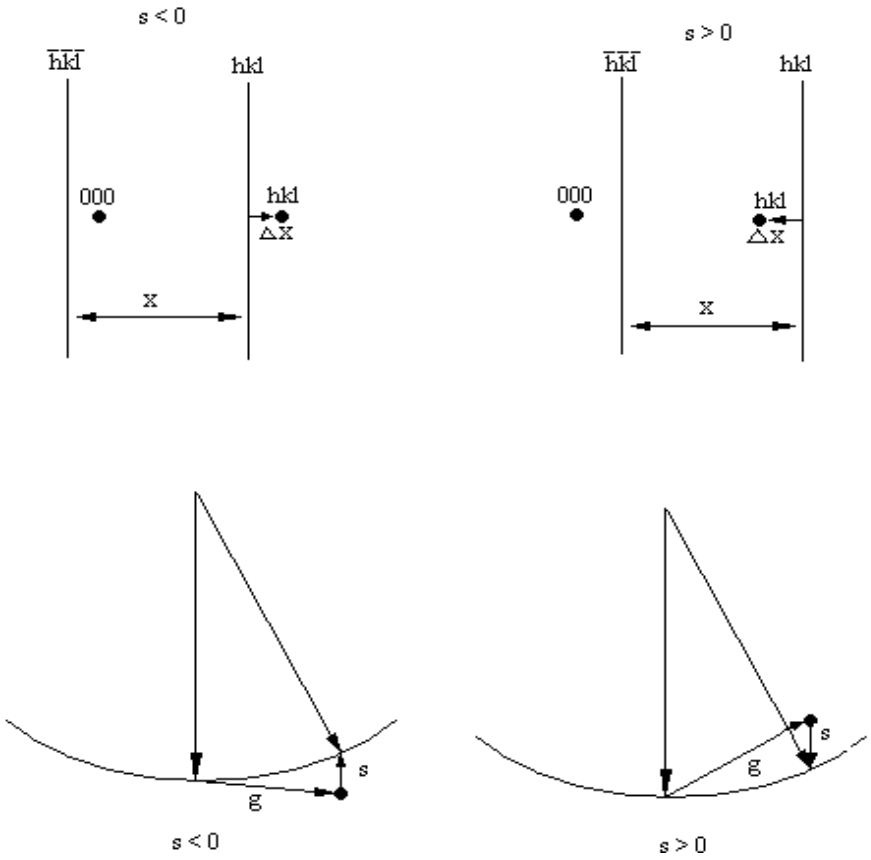

Fig. 4.5. Geometrical arrangement of Kikuchi lines for s negative and positive.

According to Edington (1975), s can be calculated from

$$|s| = \frac{\Delta x \lambda}{x d^2} \qquad \ldots(4.10)$$

where λ is the wavelength of the electrons and d is the spacing between reflecting planes. By convention, s is taken as positive when $\bar{g}$ lies inside the Ewald sphere.

4.2.5 The Method of Inside-Outside Contrast

In order to determine the interstitial or vacancy nature of a dislocation loop, one may employ the method of inside-outside contrast as explained by Edington (1975) as long as the loops are large enough to be viewed comfortably in the microscope. Since dislocation loops often lie on inclined planes, they appear elliptical when projected onto the viewing screen. The loops may consist of an extra inserted plane (interstitial loop) or a missing atomic plane (vacancy loop). Four different configurations of loop-type and orientation thus arise and these are shown in Fig. 4.6 together with their respective projections seen on the viewing screen.

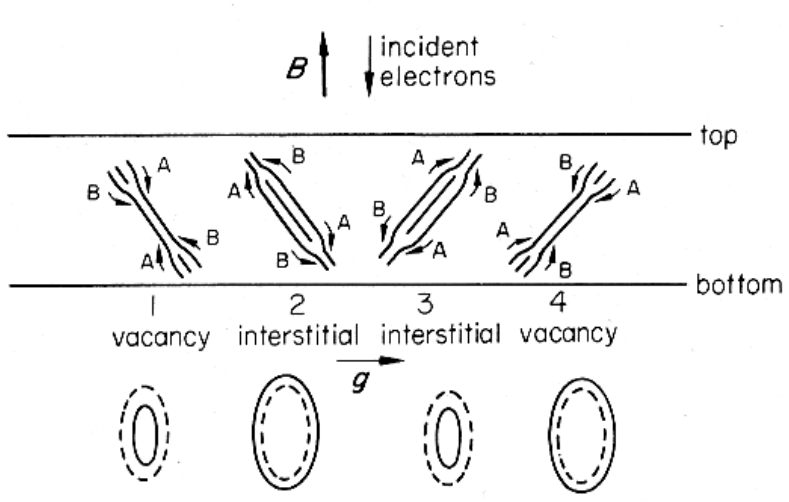

Fig. 4.6. The four possible arrangements of dislocation loops in a specimen together with their respective projections on the microscope viewing screen. The size-orientation relationship can be used to identify the nature of the loops (Edington, (1975)).

The method of inside-outside contrast depends on whether the loop image falls inside or outside the actual loop and can be determined by the sense of rotation of the reflecting planes around the dislocation. Consider the situation depicted in Fig. 4.7(a) with *s* positive. Fig. 4.7(b) shows the rotation of the reflecting planes around an edge dislocation. The reflecting plane XX is rotated clockwise towards *s = 0* by the strain field while plane YY is rotated anti-clockwise away from *s = 0*. In this way, positions in Fig. 4.6 marked with an A correspond to the situation where the reflecting plane is rotated towards *s = 0* and those labelled B correspond to areas where the plane is rotated away from *s = 0*.

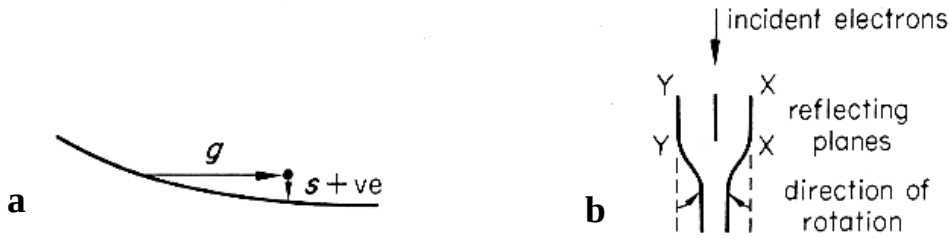

Fig. 4.7. (a) The Ewald sphere construction showing the reciprocal lattice point corresponding to the reflecting plane. (b) The reflecting planes are rotated around the dislocation by the strain field. (Edington, (1975)).

Images thus appear approximately at A relative to the core of the dislocation and the result is the formation of images as in Fig. 4.6 The dashed lines indicate the positions of the dislocation cores and the solid lines indicate the actual images. Contrast is thus inside the core for 1 and 3 while it is outside the core for 2 and 4, this implies that the sign of $\bar{g} \cdot \bar{b}$ is the same for 1 and 3 and opposite for 2 and 4. Fig. 4.8 shows the Burgers vectors of the dislocations as well as the sign of $\bar{g} \cdot \bar{b}$ if the positive direction around the loop is chosen as clockwise when looking down onto the specimen from the electron gun, and using the SF/RH criterion as explained by Hirth *et al*. (1968) to define $\bar{b}$. This definition of $\bar{b}$ allows the following conclusions to be drawn

- If $\bar{g} \cdot \bar{b} > 0$ for positive *s*, then the image lies outside the real position of the loop.

- If $\bar{n} \cdot \bar{b} < 0$, then the loop is a vacancy loop. Otherwise if $\bar{n} \cdot \bar{b} > 0$, then the loop is an interstitial loop. Here $\bar{n}$ is defined as the upward drawn normal to the habit plane of the loop.

It is thus evident that vacancy/interstitial nature of a loop can be determined if both the sense of inclination of the loop as well as the sign of $\bar{g} \cdot \bar{b}$ is known.

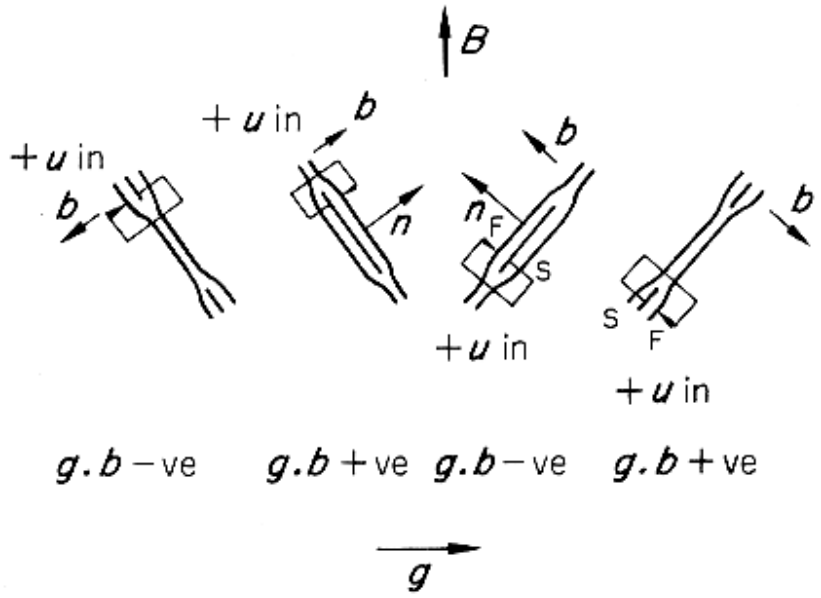

Fig. 4.8. Burgers vectors as well as the sign of $\bar{g} \cdot \bar{b}$ for the four situations depicted in Fig. 4.6. The direction of the dislocation line u is also indicated. (Edington, (1975)).

4.2.6 Moiré Fringes

Moiré fringes are produced when there is an overlap of crystals of differing lattice parameter or orientation. These patterns are characterised by light and dark interference bands usually running parallel to each other. Fig. 4.9 illustrates the production of Moiré patterns due to lattice mismatch. The fringe pattern results from interference between the transmitted and doubly diffracted beams T and DD respectively. The doubly diffracted beam DD is first diffracted from the planes of lattice 1 and then by the planes of lattice 2 in such a way that it leaves the specimen in

a direction not parallel to the transmitted beam but at a slight angle to it. If the two crystals differ from each other only in lattice parameter then a series of fringes will be formed normal to $\bar{g}$ with spacing (Hirsch *et al*. (1965))

$$\Lambda = \frac{d_1 d_2}{d_2 - d_1} \qquad \ldots(4.11)$$

where d_1 and d_2 denote the interplanar spacings of the reflecting planes in the two crystals.

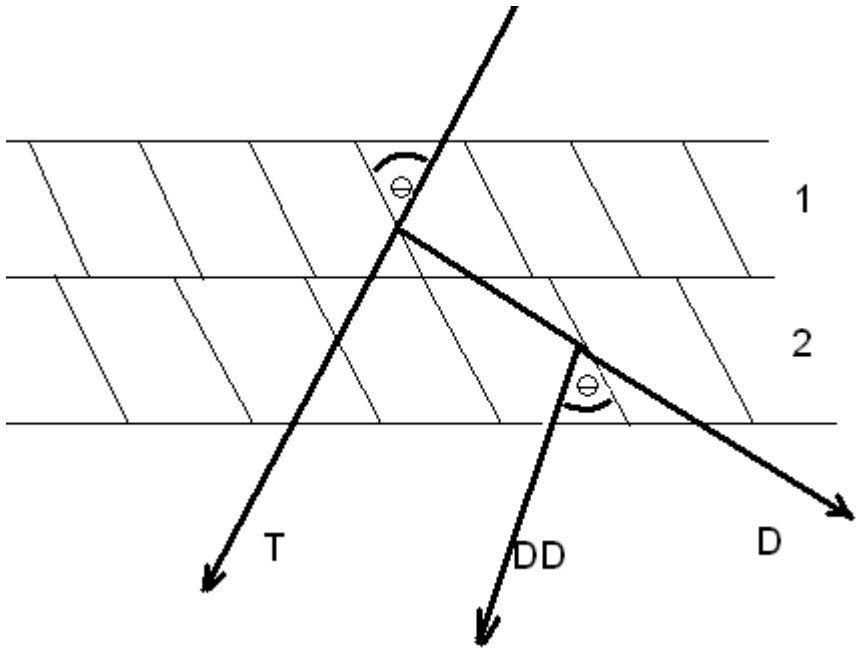

Fig, 4.9. The transmitted (T) and doubly diffracted (DD) rays interfere to form a moiré pattern.

For superimposed crystals that differ in orientation by an angle η about the incident beam, the fringes are parallel to $\bar{g}$ with spacing (Hirsch *et al*. (1965))

$$\Lambda = \frac{d}{\eta} \qquad \ldots(4.12)$$

Since the fringe spacing is related to the interplanar spacings of the different crystals, Moiré fringes enable determination of the lattice parameter of a crystal if the fringe spacing is known together with the lattice parameter of the other crystal.

4.3 Scanning Electron Microscope (SEM)

4.3.1 Backscattered Electrons

It is found experimentally that a significant fraction of the total number of electrons that are normally incident on a flat bulk target escape from the same surface of the target as where they entered (Goldstein (1992)). These electrons are called backscattered electrons and may be scattered by a single event or numerous scattering events adding up to a total deflection of more than 90°. The backscattered fraction is quantified by the backscatter coefficient η, which is defined as (Goldstein (1992))

$$\eta = \frac{n_{BSE}}{n_B} = \frac{i_{BSE}}{i_B} \qquad \ldots(4.13)$$

where n_{BSE} is the number of backscattered electrons, n_B is the number of incident electrons, i_{BSE} is the backscattered electron current and i_B is the bean current. Backscattered electrons are useful in that their intensity is dependent on the atomic number of the target, local specimen surface inclination, crystallography (electron channelling) and internal magnetic fields, This enables the microscope to generate contrast according to these properties. In general the backscatter coefficient increases for increasing atomic number according to the equation (Reuter (1972))

$$\eta = -0.0254 + 0.016Z - 1.86\times10^{-4}Z^2 + 8.3\times10^{-7}Z^3 \qquad \ldots(4.14)$$

where Z is the atomic number of the target material. If the target consists of more than one material then the backscatter coefficient becomes a weighted average of the backscatter coefficients of the constituents according to Heinrich (1966).

4.3.2 Secondary Electrons

Secondary electrons are defined as all emitted electrons with energy less than 50 eV. Although this definition includes some backscattered electrons, their contribution to the secondary electron current is negligible. The secondary electron coefficient is defined in the same way as that of the backscattered electrons and is given by Goldstein (1992) as

$$\eta = \frac{n_{SE}}{n_B} = \frac{i_{SE}}{i_B} \qquad \ldots(4.15)$$

where the symbols have similar meanings as in equation 4.12. Secondary electrons are primarily produced as a result of inelastic interactions between the energetic beam electrons and weakly bound valence or conduction electrons in the specimen according to Streitwolf (1959). Due to the large energy differences only a small amount of kinetic energy can be transferred efficiently and therefore the secondary electrons emerge with typical energies of only 2 – 5 eV (Goldstein (1992)). The intensity of secondary electrons at these low energies is rather high and they can easily be detected through Everhart-Thornley detectors with a positively charged grid in front of the detector to attract the low energy electrons. Secondary electron emission is not generally dependent on the atomic number of the specimen and therefore SEMs normally have both backscattered and secondary electron detectors.

4.3.3 Image formation in the SEM

The scanning electron microscope (SEM) operates on a completely different principle than the TEM. In the TEM the electron beam passes through the specimen and an image is formed by focussing the beam through a series of lenses in a manner that is analogous to a light microscope. In the SEM on the other hand, the electron beam never passes through the specimen and the image is formed electronically through rastering the beam across the specimen surface and measuring the intensity of emitted

electrons at each position of the beam. Fig. 4.10 shows a schematic of the SEM column and specimen chamber.

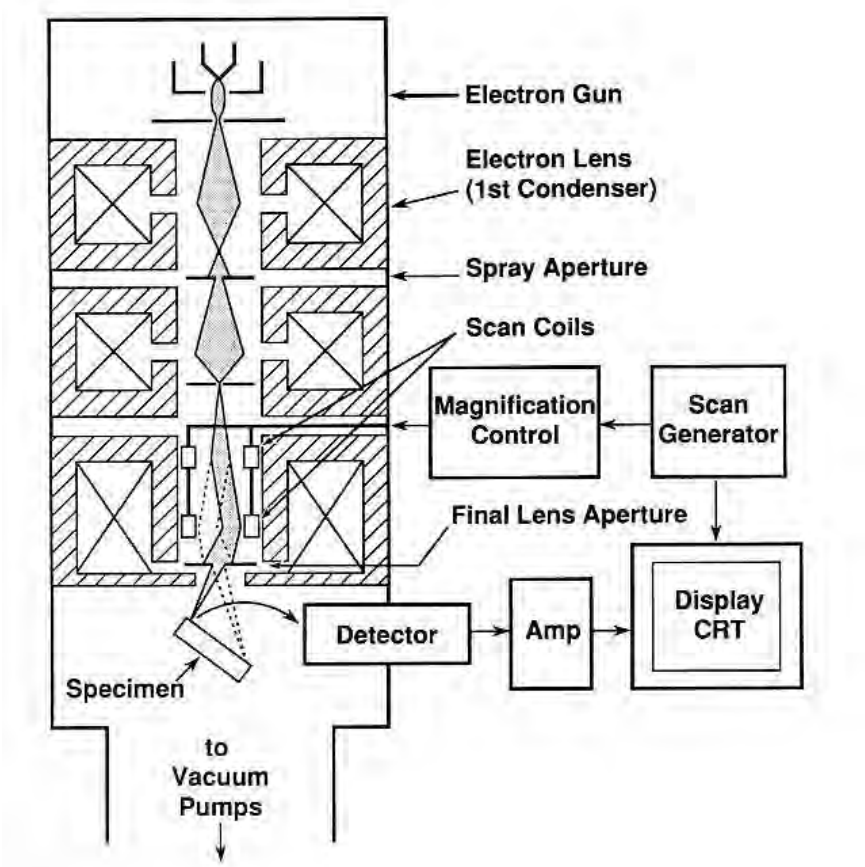

Fig. 4.10. Schematic representation of an SEM (Goldstein et al. (1992)).

The electron beam is focussed to a small spot on the surface of the specimen through the lens system and scanned across the specimen in a rectangular pattern. At each point during the scan, the intensity of either backscattered electrons (BSE) or secondary electrons (SE) is recorded and this intensity is mapped to the intensity of the pixel, corresponding to the position of the spot at that time, on the viewing screen in order to produce an image of the specimen surface.

4.4 Energy Dispersive X-ray Spectrometry (EDX)

The SEM is not limited to detecting only electrons. Any radiation produced during the interaction of the electron beam with the specimen may be detected if a suitable detector is installed in the system. One such type of radiation which is of great interest for elemental analysis is the characteristic X-rays generated by the material under electron bombardment. Elemental analysis based on these X-rays can be done using wavelength dispersive X-ray spectroscopy (WDS) or energy dispersive X-ray spectrometry (EDX). The latter technique was employed in the present study.

Apart from the X-ray background as a result of bremsstrahlung (see Goldstein *et al*. (1992)) caused by the deceleration of the incident electrons in the Coulombic field of the atoms in the target, high intensity characteristic peaks are also present in the X-ray spectrum. The positions of these peaks are unique to the element responsible for their generation and the spectrum can thus be used to determine the composition of a given specimen. Fig. 4.11 shows a typical X-ay spectrum obtained from an Ag-Pd deposit on SiC with the characteristic peaks of the different elements identified.

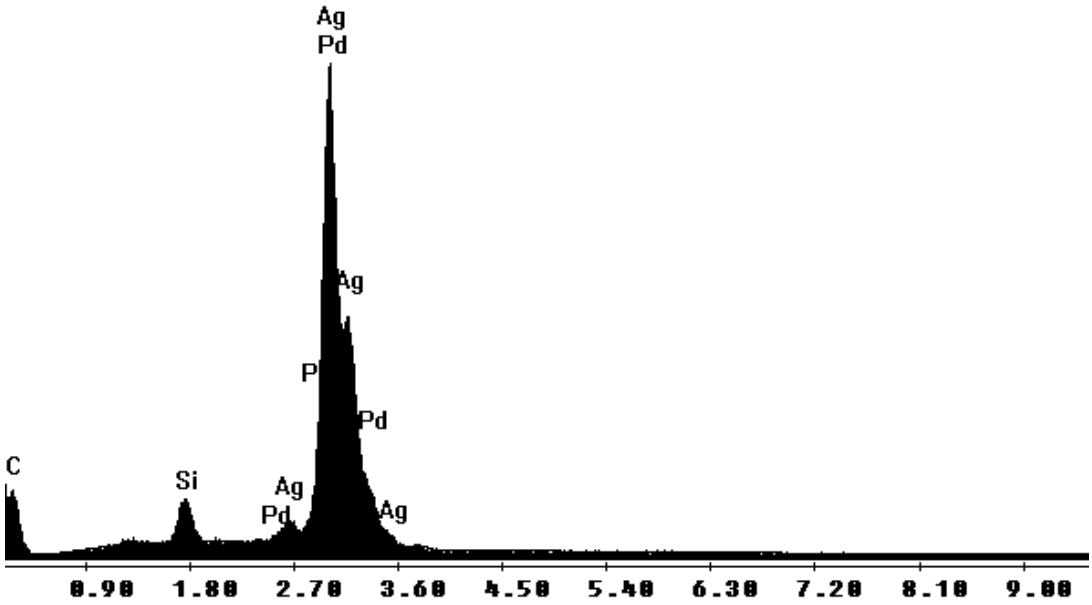

Fig. 4.11. EDX spectrum of Ag-Pd deposit on SiC.

Characteristic X-rays are produced when an energetic electron knocks an inner shell electron out of position and an electron from a higher energy shell falls into its place releasing a photon of energy equal to the difference in energy between its initial and final energy levels as shown in Fig. 4.12.

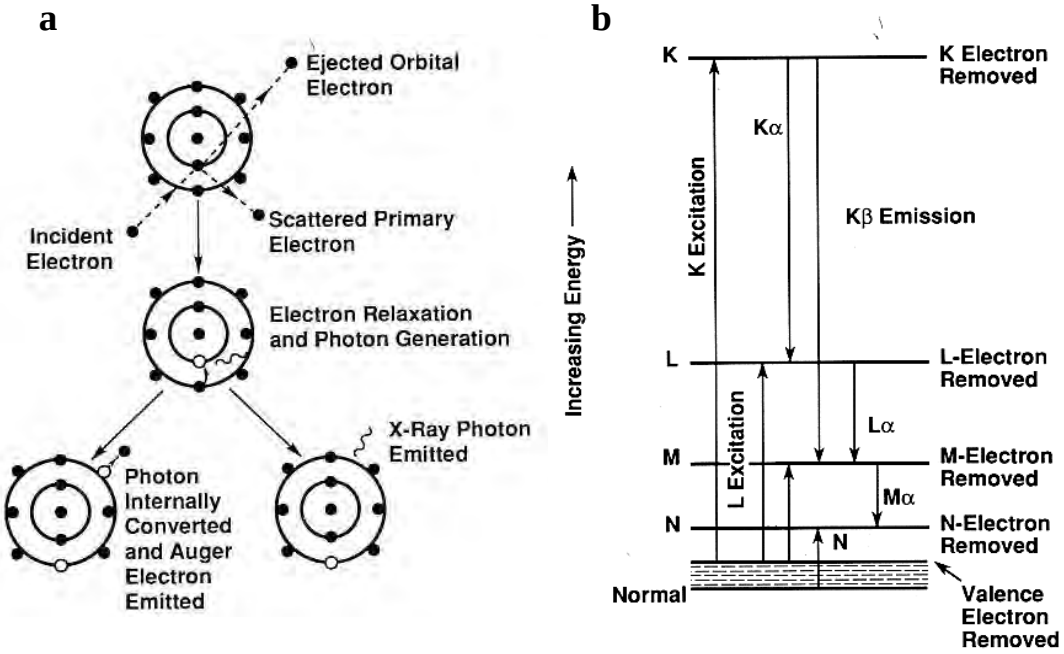

Fig. 4.12. Illustration of inner shell ionization and de-excitation with X-ray emission (a) as well as an energy level diagram (b) distinguishing between different families of electron transitions producing characteristic X-rays (Goldstein (1992)).

The wavelength of such an X-ray is given by Moseley's law (Goldstein (1992))

$$\lambda = \frac{B}{(Z-C)^2} \qquad \ldots(4.16)$$

where B and C are constants depending on the family of electronic transitions (K_α, L_β etc.).

4.5 Nanoindentation Hardness Tester

Hardness, the resistance of a material to plastic deformation, is measured on a variety of different scales which include Vickers, Rockwell, Martens etc. which differ in measurement procedure and method of calculation. These methods typically consist of indenting the surface of the specimen with a hard (usually diamond) indenter and measurement of the residual imprint left in the material after removal of the indenter. Instrumented hardness testing on the other hand relies on indenting the material surface with an indenter of which the geometry is known to a high precision while monitoring the applied load and penetration depth throughout the insertion and removal of the indenter. Having this data enables one to estimate properties such as material hardness, elastic modulus and fracture toughness (Doerner *et al*. (1986) and Oliver *et al*. (1992)) Fig. 4.13 shows a schematic of the nanoindenter head assembly used in this experiment. The diamond Berkovich indenter is pushed into the material through magnetic repulsion when a current is passed through the coil. The displacement of the indenter is measured with respect to the surface, through the reference ring and displacement sensor assembly which limits the compliance of the system to the few millimetres of material between the indenter tip and sensor arrangement.

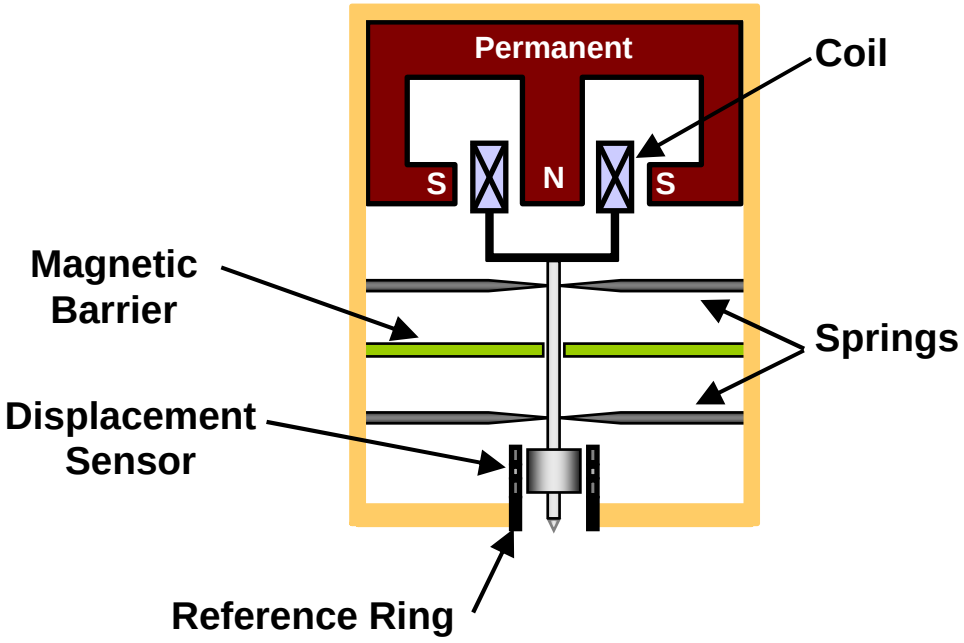

Fig. 4.13. Nano indenter head assembly (CSM Instruments presentation).

Nano indentation is an excellent technique for measuring mechanical properties of bulk materials as well as thin coatings. Fig. 4.14 shows a section through an indent illustrating the definition of different depths used to estimate the contact area between indenter tip and material as well as a typical indentation curve defining the same symbols. An accurate estimate of the contact area is crucial to obtaining meaningful hardness values. The maximum exerted force F_{max} and the maximum penetration depth h_m are read directly from the graph at the same data point. The hardness of the material, H_{IT}, is calculated through

$$H_{IT} = \frac{F_m}{A_p} \qquad \ldots(4.17)$$

where A_p is the projected contact area corresponding to the depth h_p. The elastic modulus of the material, E_{IT}, may also be calculated from

$$E_{IT} = \frac{1-\nu^2}{\frac{1}{E_{IT}^*} - \frac{1-\nu_i^{\,2}}{E_i}} \qquad \ldots(4.18)$$

where ν is Poisson's ratio for the material being indented, ν_i is Poisson's ratio for the indenter material, E_i is the elastic modulus of the indenter and $E_{IT}^{\,*}$ is the reduced modulus given by

$$E_{IT}^* = \frac{\sqrt{\pi}}{2}\frac{S}{\sqrt{A_p}} \qquad \ldots(4.19)$$

and $$\frac{1}{E_{IT}^*} = \frac{1-\nu^2}{E_{IT}} + \frac{1-\nu_i}{E_i} \qquad \ldots(4.20)$$

from which 4.18 is obtained. Here, S is the slope of the load versus displacement graph from maximum load during the start of the unloading cycle as shown in Fig. 4.14.

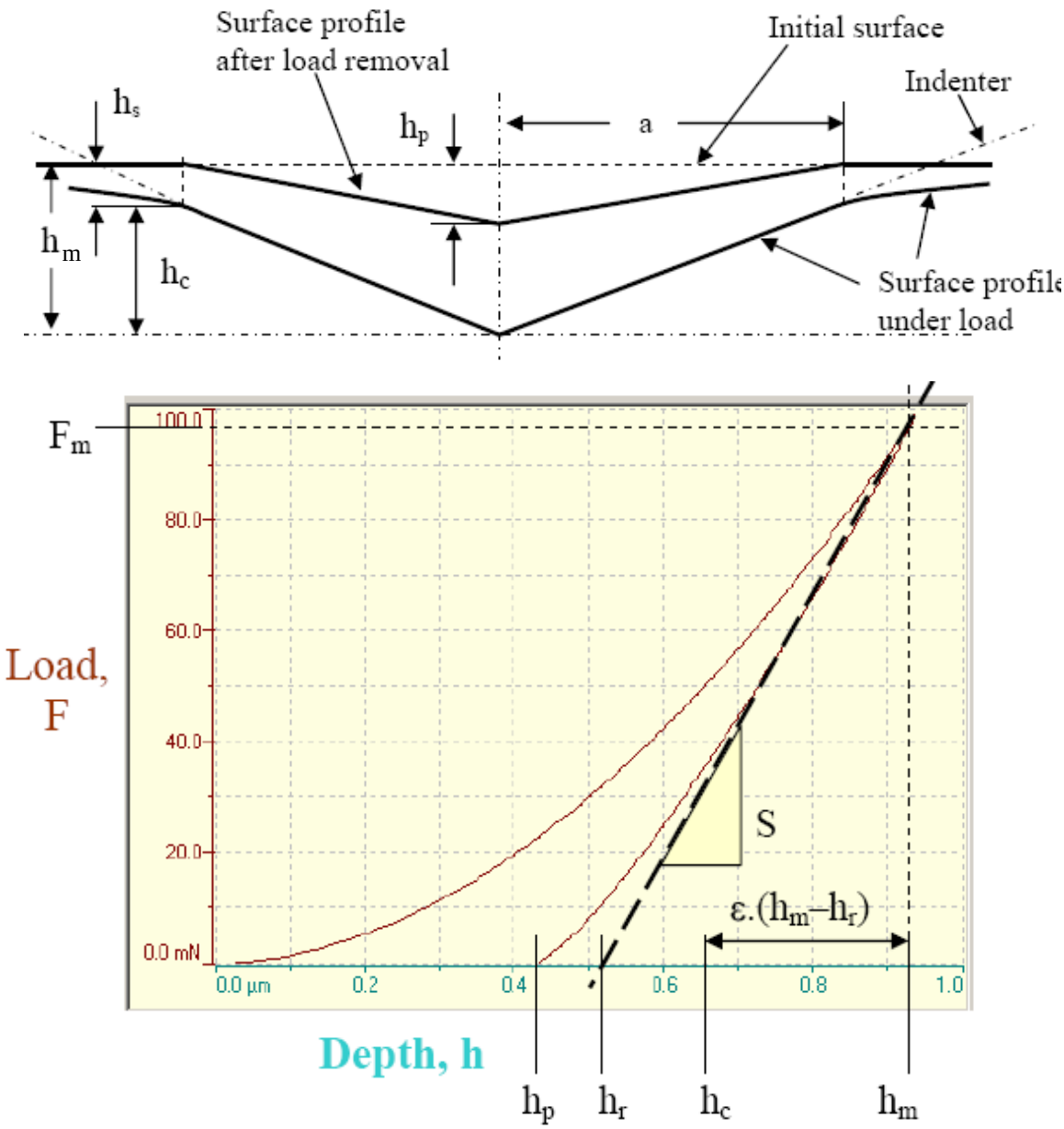

Fig. 4.14. Section through an indent (top) and typical indentation curve (bottom) defining different depths (CSM Instruments (2007)).

In calculating all these properties, the projected contact area A_p is required. The area of a pyramidal tip can be calculated from

$$A_p = C_0 h^2 \qquad \ldots(4.21)$$

where C_0 is a constant depending on the geometry of the tip in question and h is the height of the tip. In reality, no perfect tip exists because of rounding of the tip so instead the area is approximated by an expansion of the form

$$A_p = C_0 h^2 + C_1 h + C_2 h^{1/2} + C_3 h^{1/4} + \ldots \qquad \ldots(4.22)$$

where the constants C_n are obtained from a calibration curve using fused silica as specimen (Oliver *et al*. (1992)). Due to sink-in of the material surface, the projected contact area can not be calculated from the maximum penetration depth; instead the reduced depth h_c (see Fig. 4.14) is used. According to Oliver *et al*. (1992), the reduced depth can be calculated from

$$h_c = h_m - \varepsilon \frac{F_m}{S} \qquad \ldots(4.23)$$

where ε is a constant with value depending on the indenter shape. For many materials the projected contact area is a good approximation to the residual imprint area.

CHAPTER FIVE

EXPERIMENTAL PROCEDURE

5.1 Introduction

This chapter aims to explain the methods employed to prepare specimens for analysis by the various techniques used. The chapter starts off with a brief description of the parameters during growth of the SiC as well as the ion implantation. This is followed by a description of the furnaces used to anneal specimens as well as the specially made graphite containers in which they were annealed. Emphasis is placed on TEM specimen preparation as this technique is by far the most sensitive to specimen preparation of all the techniques used in the study. The chapter concludes with the preparation of specimens for nanoindentation hardness measurements.

5.2 Growth of SiC and Ion Implantation

SiC wafers were grown by NovaSiC in France. Polycrystalline 3C-SiC was grown on Si (001) at 1380 °C using H_2 as carrier gas with C_3H_8 and SiH_4 as precursors. The growth rate was 2 µm/h and the chamber pressure was maintained at 200 mbar. Single crystal 6H-SiC (0001) was grown using the sublimation method in which SiC powder is sublimated under low pressure and high temperature and allowed to crystallize on a seed crystal at the top of the chamber at a slightly lower temperature.

The SiC was cut into approximately 3-4 cm^2 pieces and sent to CORE in the USA for implantation (see Fig. 5.1). The 3C-SiC was implanted with H^+ at 100 keV to a total dose of 10^{17} ions/cm^2 and the 6H-SiC was implanted with 100 keV He^+ ions to a total dose of 10^{17} ions/cm^2

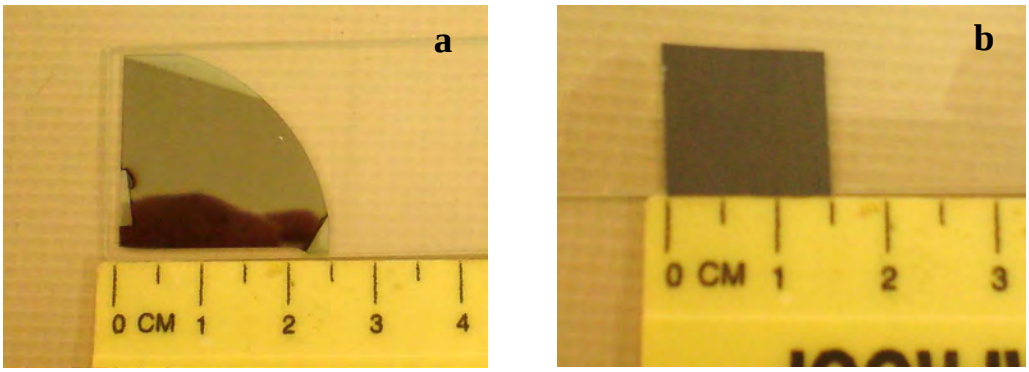

Fig. 5.1. Single crystal, hexagonal 6H-SiC (a) and polycrystalline 3C-SiC (b) after implantation. The reflective area on the 6H-SiC is the implanted area and the shielded areas on the corners are clearly visible where the sample was fixed with adhesive tape for implantation.

5.3 Specimen preparation

Strips of the implanted material with a width of approximately 2 mm were cut using a Well Precision Diamond Wire Saw. These strips were taken from the middle of the implanted area to ensure that the strips were implanted to the full dose since the dose may decrease towards the edge of the implanted area. Annealing up to 1000 °C was done in a resistively heated quartz tube furnace (see Fig. 5.2) in an argon atmosphere. The furnace was first heated up to the required temperature before the specimens were loaded. After the required time had elapsed, the quartz specimen holder was retracted from the heating element towards the end of the tube near the Ar inlet pipe and allowed to cool quickly while still in the inert atmosphere. This was done to freeze in any extended defects that might have formed inside the material during annealing.

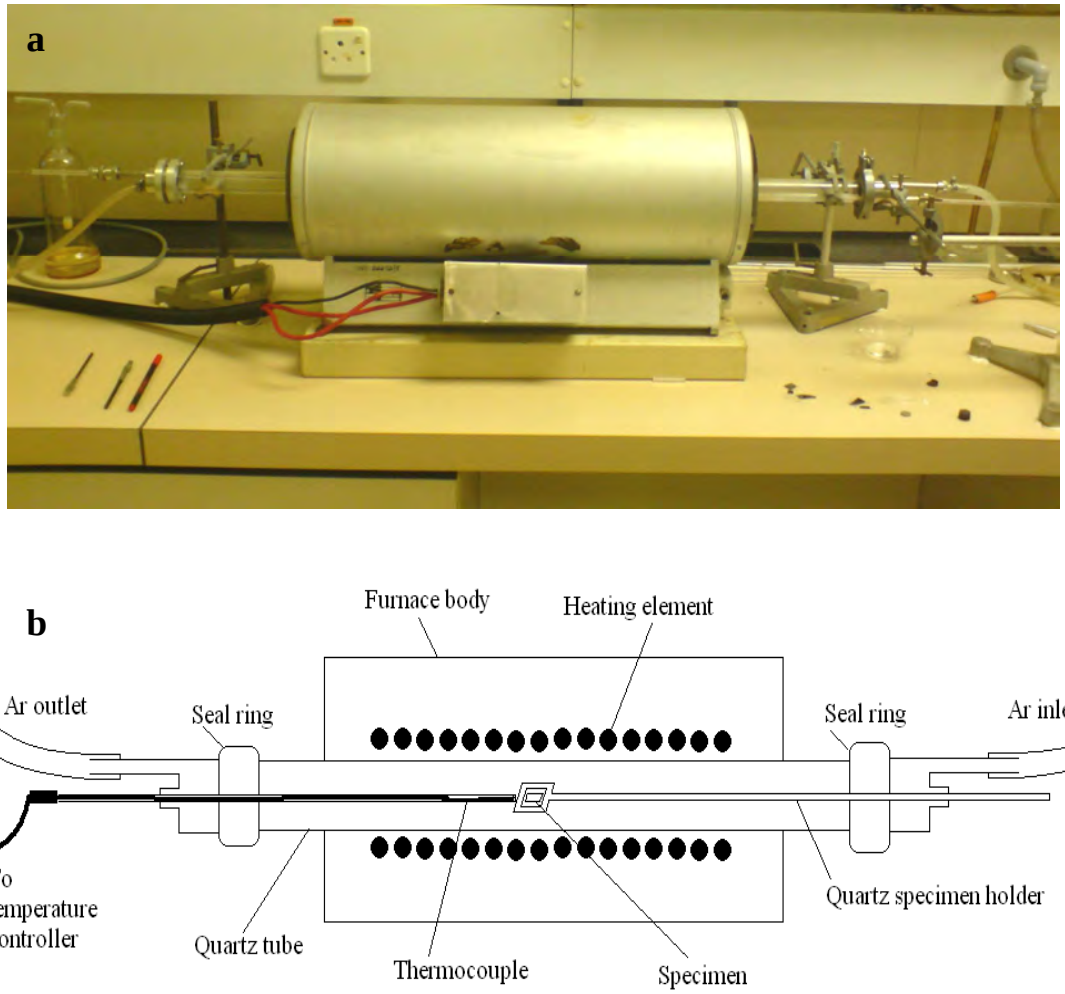

Fig. 5.2. The Quartz tube furnace (a) used in annealing experiments as well as a schematic of the furnace indicating the various parts (b). Specimens were placed implanted face down on a piece of Si with the Si resting on the quartz specimen holder. Ar gas flowed through the system throughout the procedure.

Annealing above 1000 °C was performed in a resistively heated Webb 89 vacuum furnace supplied by R.D. Webb Company (USA) (see Fig. 5.3) at a pressure of about 10^{-6} mbar. Due to the design of the furnace it was not possible to insert specimens once the furnace had reached the required temperature and thus specimens had to heat up along with the furnace at 25 °C per minute. Fast quenching of the specimens after annealing was impossible for the same reason and specimens were allowed to cool naturally inside the furnace under vacuum.

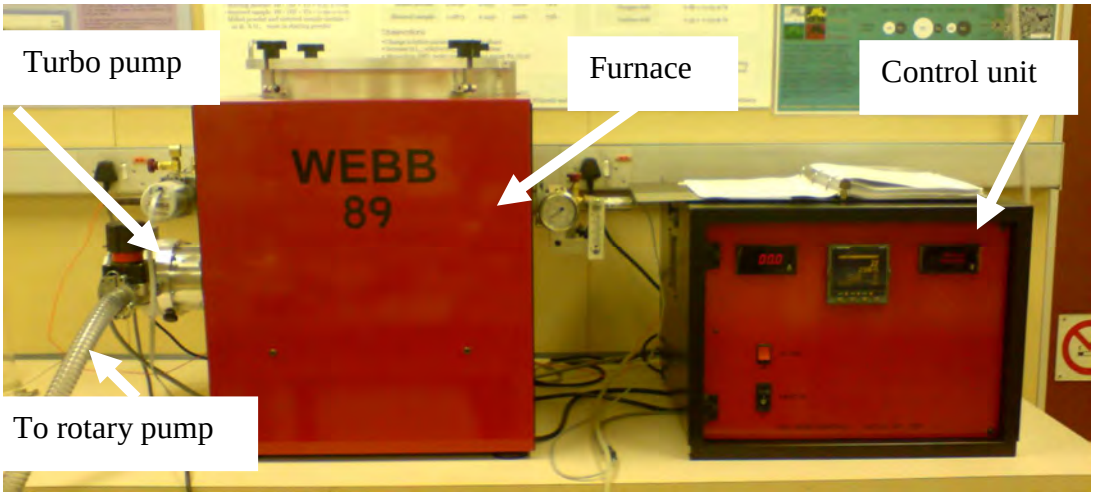

Fig. 5.3. Webb 89 furnace used in annealing experiments above 1000 °C.

Fig. 5.4 shows an example of a graphite container used to hold specimens during annealing in the above mentioned furnace. The purpose of the containers was twofold. Firstly, they enclose the specimens and in doing so prevent contamination of the inside of the furnace. Secondly, since the furnace uses both a thermocouple as well as a pyrometer to monitor the temperature and the pyrometer is calibrated for the emission spectrum of graphite; it simplifies experiments in the sense that the pyrometer did not have to be calibrated for different specimen materials.

Fig. 5.4. Graphite specimen holder used to contain specimens during annealing in the Webb 89 furnace.

5.4 TEM Specimens

Specimens observed in the TEM need to be extremely thin in order to be sufficiently electron transparent for an image to be formed on the viewing screen. The two basic types of TEM specimens namely planar and cross-sectional (XTEM) are prepared somewhat differently from one another. Since this work deals with damage created by implanted ions as well as diffusion from the specimen surface, cross-sectional specimens were prepared in order to be able to measure amongst others the range of the implanted species from the implanted surface. For each specimen, four wafers were cut to approximately 3 mm x 2 mm using a diamond wire saw. These wafers were then glued together with the implanted surfaces facing each other as shown in Fig. 5.5.

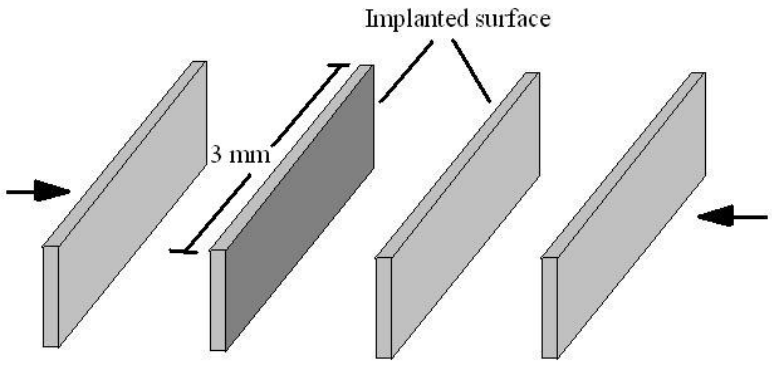

Fig. 5.5. Four wafers were stuck together with the implanted surfaces facing each other along the centre glue line.

The assembly was baked at 130 °C for 20 min in order for the glue to harden and then polished using a Buehler Beta polisher-grinder starting with a 30 µm grinding disc and moving down to 1 µm before sticking the polished surface onto a copper TEM grid as shown in Fig. 5.6. Each stage of the polishing was continued until all damage created by the previous stage was no longer visible under an optical microscope at 56x magnification. The specimen was thinned down to approximately 50 µm and again polished down to 1 µm as before.

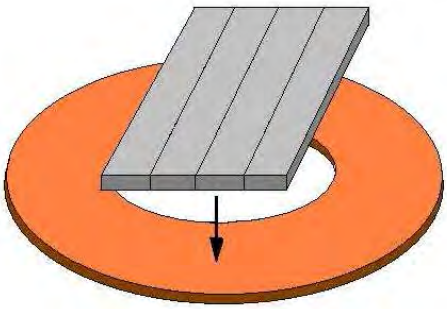

Fig. 5.6. The polished surface is fixed to a copper TEM grid.

The thinned specimen was then put in a Gatan Precision Ion Polishing System (PIPS) and ion polished at an angle of 4° with 5 keV Ar atoms at a rotation rate of 3 revolutions per minute until a small hole was formed along the centre glue line. Fig. 5.7 shows a photo of the Gatan PIPS while Fig. 5.8 shows a schematic of the inside of the PIPS. Fig. 5.9 shows the resultant hole that forms along the centre glue line, the area around this hole was then thin enough to examine in the TEM.

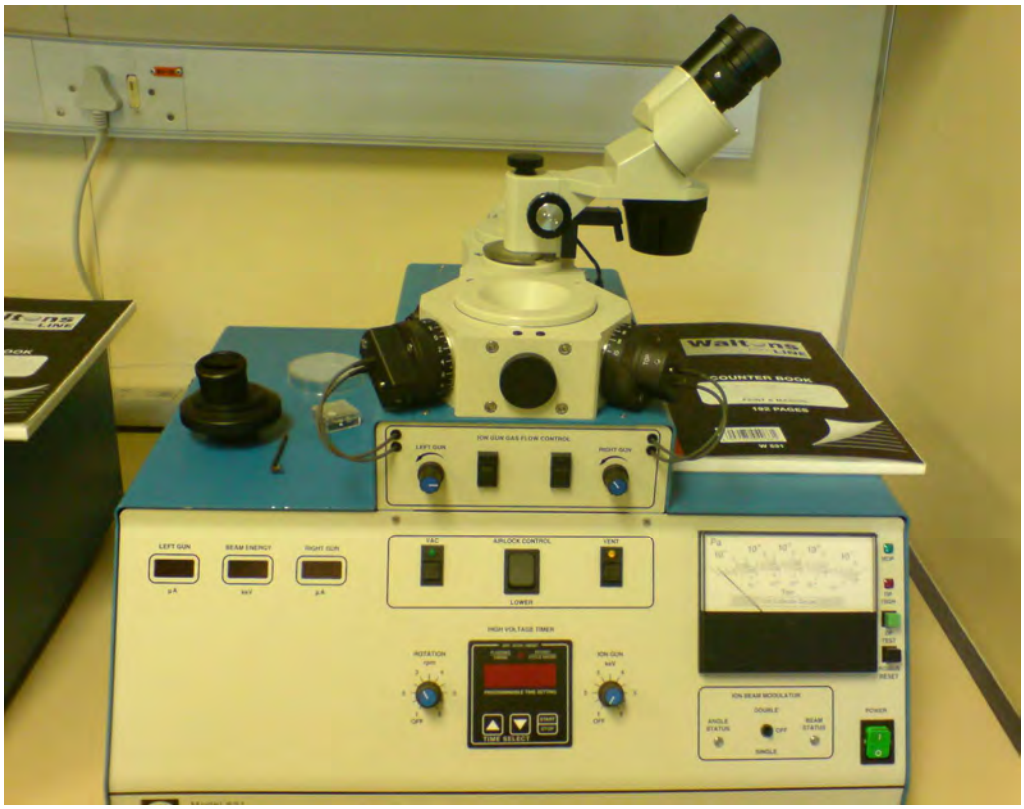

Fig. 5.7. A Gatan precision ion polishing system.

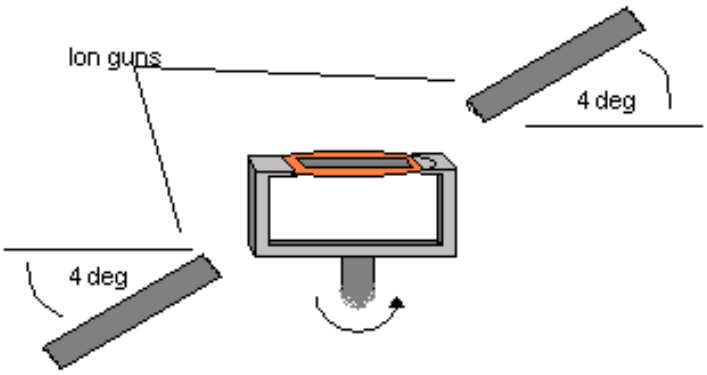

Fig. 5.8. Schematic representation of an ion mill, the ion beams are modulated to prevent excessive erosion of the metal specimen holder when the arms pass through the ion beam.

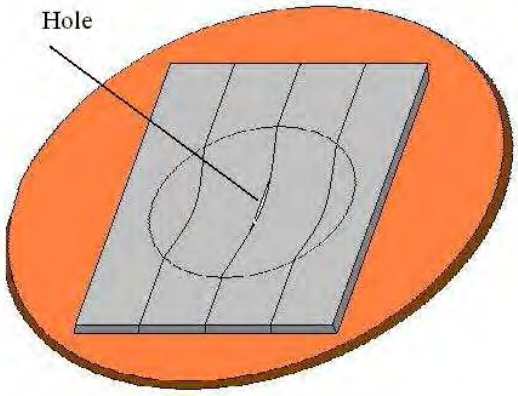

Fig. 5.9. Specimens were ion milled until a hole was formed along the centre glue line.

5.5 Nanoindentation Hardness Measurements

Specimens used for nanoindentation hardness measurements need to have a smooth surface with an average surface roughness of less than 1/20 of the penetration depth of the indenter tip (CSM Instruments (2007)). It was therefore not possible to perform nanoindentation hardness measurements on the polycrystalline 3C-SiC specimens and

measurements were made only on the single crystal 6H-SiC specimens. The aim of the nanoindentation hardness experiments was to compare the hardness of the implanted specimens as a function of depth beneath the surface to that of the virgin material. Implanted and virgin specimens were annealed for 20 min at 1000 °C in an inert Ar atmosphere in a quartz tube furnace as described earlier in the text in order for the point defects to be sufficiently mobile to form extendes defects in the material. The virgin material was annealed as well in order to ensure that any measured differences in hardness is as a result of the implantation only and not due to annealing. Hardness versus depth measurements were also performed on an as implanted specimen to compare with the other two specimens.

CHAPTER SIX

RESULTS AND DISCUSSION

6.1 Introduction

H and He are produced in the SiC layer of TRISO coated particles by neutron transmutation. The aim of this investigation was to determine whether high concentrations of H and He could effect the release of the fission products Ag and Pd from TRISO coated particles by enhancing their transport through the SiC layer. For this investigation, experiments were designed to investigate the effects of H and He on the microstructure of SiC and to detirmine whether it could enhance the transport of Ag or Pd through the creation of microcracks or void channels in the material. Heinisch *et al.* (2004) calculated the concentrations of elements produced in SiC by neutron irradiation in a PBMR (see chapter 2.10). The average concentration of H in SiC at the projected range for a dose of $1x10^{17}$ ions/cm^2 assuming a peak distribution width of 200 nm was calculated as about 50000 appm with that of He under the same fluence being very similar. These concentrations are far greater than the 8.0 appm and 5.8 appm calculated for H and He respectively by Heinisch *et al.* (2004). High concentrations were necessary however to ensure sufficient lattice damage creation for TEM analysis. The results obtained by studying these much higher concentrations are still applicable because of the high mobility of especially H in SiC which can lead to high concentrations of the element diffusing towards sinks such as grain boundaries, dislocation cores and cavities in coated particles. This might produce void channels which can enhance the transport of Ag and Pd through the material as mentioned above. TEM analysis was performed using a Philips CM20 TEM at 200 kV and SEM analysis was carried out on a Philips XL30.

6.2 Ion Ranges

In order to obtain a plot of the experimentally observed damage in the layers as a function of depth beneath the layer surface, a program was written in MATLAB. The program accepts a monochrome bitmap of the damaged region which was prepared by passing the relevant TEM micrographs through an edge detection filter and saving the resultant file as a 1-bit .bmp file as in Fig. 6.1.

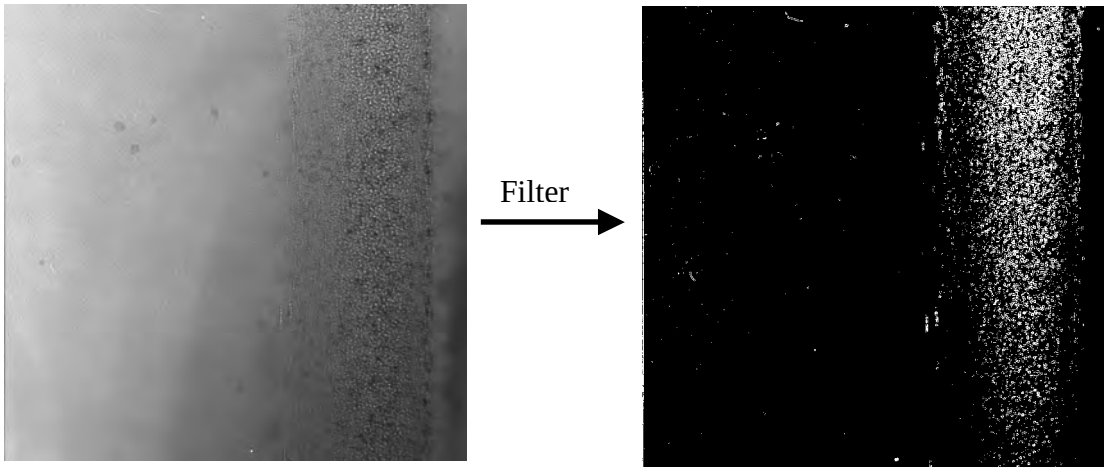

Fig. 6.1. The TEM micrograph on the left was passed through an edge detection filter and the resulting image was reduced to a 1-bit monochrome image for processing.

The program assumes that the white pixels in the resulting image are indicative of some sort of damage in the material since the voids were small enough to be completely highlighted by the edge detection filter and very few white pixels are seen outside the damaged area. The program requires the depth underneath the sample surface at the right-hand edge of the image and assumes that the sample surface lies in a vertical plane normal to the image plane and is at the left hand side of the image. It then counts the number of vertical pixels in the image as well as the number of white pixels in each vertical column of pixels in the image and stores the fraction of white-to-total number of pixels in a vector so that it may later be plotted as a function of depth beneath the sample surface. This depth is calibrated using the horizontal resolution of the image and the depth at the right-hand side of the image. A binning factor is included to avoid spikes and smooth out the damage profile somewhat. The largest observed voids cover an area of approximately 6x6 pixels in the original

micrograph and a binning value of 10 was used when processing the images meaning that ten consecutive pixel columns were averaged for each data point produced in the graph so that the effective sampling area was wide enough as not to produce any significant spikes in the plot as a result of individual features in the image.

The width of the error bars in the plot correspond to the width of these binned columns with the depth coordinate of the data points being equal to the depth of the middle of the corresponding columns. Vertical error bars were given the same length as the horizontal bars although they have little meaning in this case since the plotted graphs were scaled to have a maximum value of 1. This was done to better illustrate the relative positions of the maxima which were the quantities of interest. The peak heights were not used in any analysis since although they are representative of the peak damage concentration; it could not be guaranteed that all white pixels in the processed micrographs represent damage in the material. It was however assumed that the peak position of the processed micrographs would be very close to the actual damage peak position.

TRIM 2008 plots of both ion range and damage produced by vacancy generation were also plotted on the same set of axes as the experimental data in order to compare the observed range with that predicted by theory. A density of 3.215 g/cm^3 (Snead *et al*. (2007)) was used in the calculations as well as Si and C displacement energies of 35 eV and 22 eV respectively (Tromas *et al*. (2008)).

Fig. 6.2 shows the experimentally observed damaged region determined as discussed above for 100 keV He ions implanted into 6H-SiC to a total dose of 10^{17} ions/cm^2 and annealed for 20 min at 1000 °C in an Ar atmosphere as well as the ion range and damage due to vacancies produced predicted by TRIM 2008 for 100 keV He in SiC. Very good agreement between the predicted range and actual damage range can be observed. The peak labelled 1 in the figure is due to some contrast along the specimen surface on the left hand side of the micrograph and should thus be disregarded since it does not represent any implantation damage. Fig. 6.3 shows a similar plot for 100 keV H ions implanted in 3C-SiC to a total dose of 10^{17} ions/cm^2 and annealed at 1000 °C in an Ar atmosphere for 20 min. Again there is a peak labelled 1 at the far left of the graph due to contrast at the specimen surface that is of

no significance. The right-hand side of the main peak also decreases much slower than the left-hand side and there are numerous small peaks visible on the right as well. These features are a result of contrast around a relatively high concentration of loop-like defects (see Chapter 6.4) visible beyond the main damaged region in the micrograph shown in Fig. 6.4 and are therefore not significant as far as implantation range is concerned.

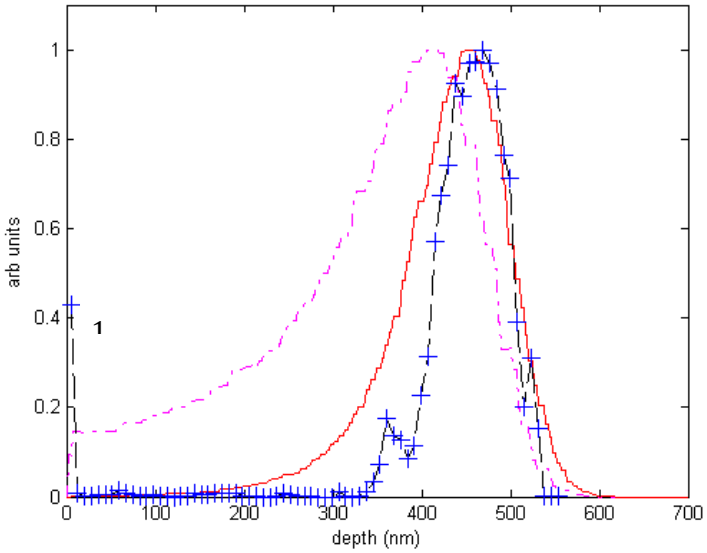

Fig. 6.2. Plots of TRIM calculated vacancy damage (dotted line), TRIM calculated ion range (solid line) and experimentally determined damage range (dotted line with data markers) for 100 keV He ions in 6H-SiC with a total dose of 10^{17} ions/cm^2 .

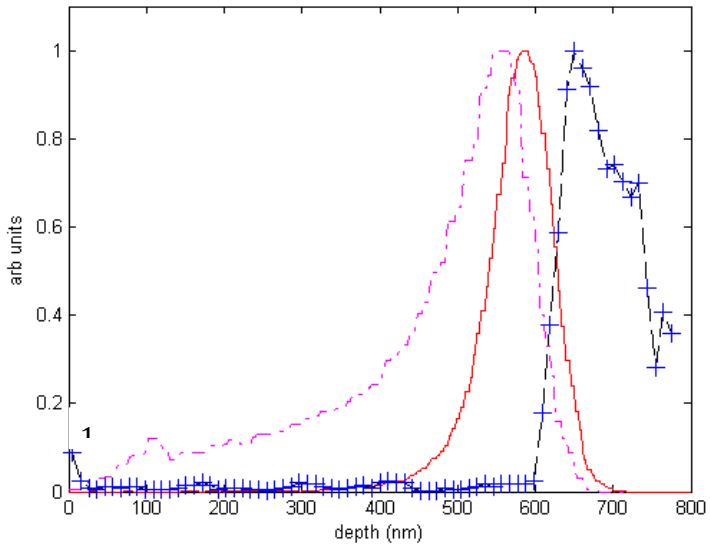

Fig. 6.3. Plots of TRIM calculated vacancy damage (dotted line), TRIM calculated ion range (solid line) and experimentally determined damage range (dotted line with data markers) for 100 keV H ions in 3C-SiC with a total dose of 10^{17} ions/cm^2.

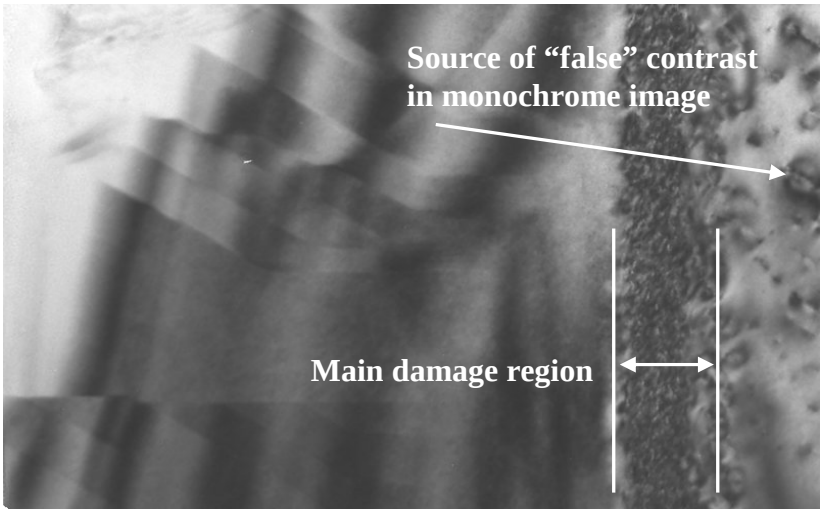

Fig. 6.4. Cross-sectional BF TEM image showing the loop-like defects to the right of the main damaged region produced contrast in the monochrome image that was not related to the main damaged region.

6.3 Implantation Damage

6.3.1 He Implanted 6H-SiC

Fig. 6.5(a) shows a BF TEM micrograph of unannealed 6H-SiC implanted with 100 keV He^+ ions to a fluence of $1x10^{17}$ ions/cm^2. The selected area diffraction (SAD) pattern (b) taken over the damaged region indicates that no amorphization has taken place since no ring patterns were observed. Other authors such as Nakata *et al*. (1991) observed amorphization of 6H-SiC when implanted with 400 keV He^+ to a fluence of $1x10^{16}$ ions/cm^2 at 300 K (see chapter 2.10). Sasase et al. (2003) found no amorphization after implanting 6H-SiC with 3 MeV He^{2+} ions to a fluence of $1x10^{17}$ ions/cm^2 at 300 K and suggested that the critical fluence required for amorphization increases with implantation energy. If this is true then it is reasonable to assume that the specimens used in the current investigation heated up considerably during implantatioin which annealed the specimen while being implanted. CORE confirmed that no attempt was made to maintain specimen temperature at room temperature during implantation but could not confirm the actual implantation temperature as the

system did not provide a means to measure it. However CORE believes that the temperature was in the range 200 – 300 °C.

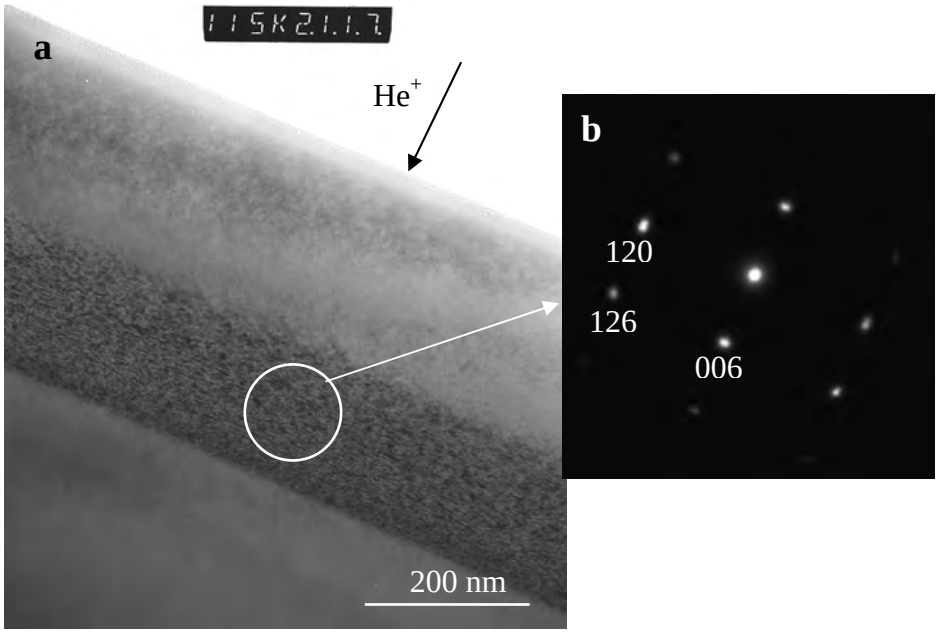

Fig. 6.5. Unannealed 6H-SiC implanted with 100 keV He^+ ions to a dose of 10^{17} ions/cm^2 remains crystalline in the damaged region (a) as can be deduced from the SAD pattern in (b).

Fig. 6.6 shows a BF TEM micrograph of 6H-SiC implanted with 100 keV He^+ ions to a total dose of 1 x 10^{17} ions/cm^2, and annealed at 1000 ºC for 20 min. A high density of small voids is clearly visible in the damaged region corresponding to the projected range of the He ions. The voids are visible under kinematical diffraction conditions when the strain contrast images of small lattice defects are invisible. Similar observations have been made by Hasegawa *et al*. (1999) and Sasase *et al*. (2003). When the damaged region is observed under dynamical diffraction conditions, a high density of strain contrast images of lattice defects, including resolvable loop-like defects, are present throughout the damaged region as shown in Fig. 6.7. A defect resembling a He-platelet (or dislocation loop) lying on a {0001} plane is viewed edge-on in Fig 6.7 indicated by a thick arrow. The differentiation between loops and platelets is discussed in Chapter 6.3.2 (page 76). No evidence of cracking or exfoliation was observed in He implanted 6H-SiC.

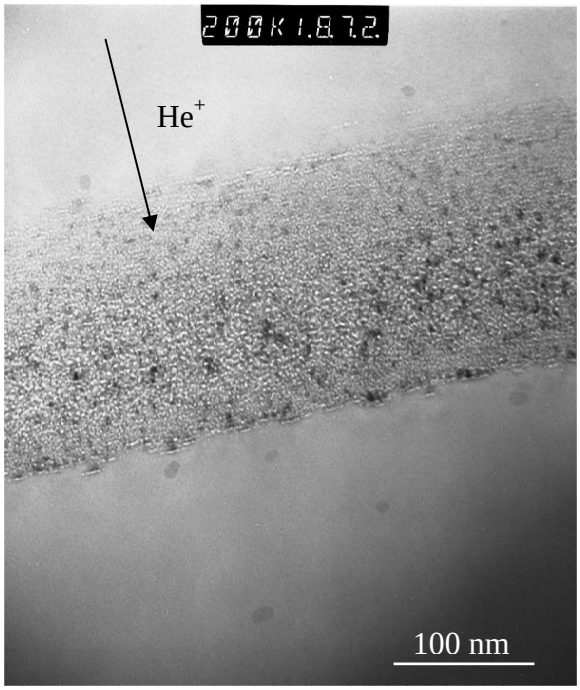

Fig. 6.6. Cross-sectional BF TEM image of 6H-SiC implanted with 100 keV He^+ ions to a dose of 10^{17} ions/cm^2 and annealed for 20 min at 1000 °C in an Ar atmosphere.

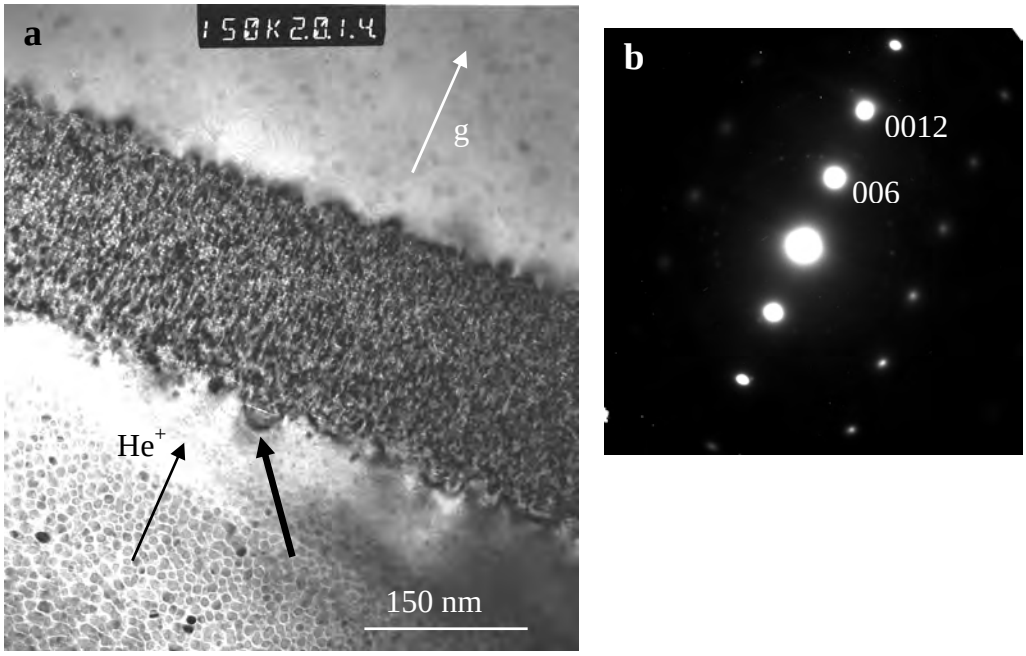

Fig. 6.7. (a) Cross-sectional BF TEM image illustrating that changing the diffraction condition causes the strain contrast to become visible. The SAD pattern in (b) indicates the diffraction condition used.

The calculated He projected range (from TRIM 2008) and associated vacancy concentration profile are superimposed on the BF TEM micrograph of the He range in Fig. 6.8. Excellent agreement between the experimental damage layer range and calculated He projected range is observed.

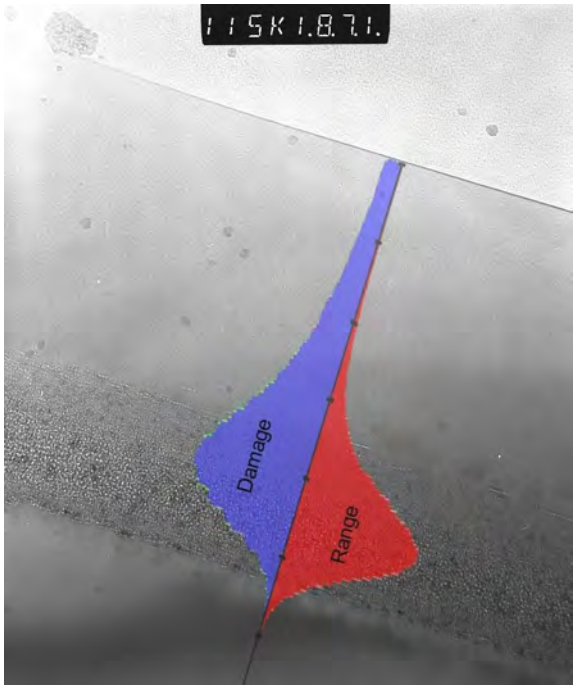

Fig. 6.8. Cross-sectional BF TEM image of 6H-SiC implanted with 100 keV He^+ ions to a dose of 10^{17} ions/cm^2 and annealed for 20 min at 1000 °C in an Ar atmosphere. The TRIM calculated vacancy concentration profile (labelled "Damage") and range plots are superimposed for comparison. Markings on the plot indicate 100 nm.

6.3.2 H Implanted 3C-SiC

Fig. 6.9(a) shows a bright-field TEM micrograph of unannealed 3C-SiC implanted with 100 keV H^+ ions to a fluence of $1x10^{17}$ ions/cm^2. As in the case of He implanted into 6H-SiC, no amorphization occurred in the damaged region as shown by the SAD pattern in Fig. 6.9(b). This however is not surprising since H has such a low mass making it highly improbable to cause any amorphization.

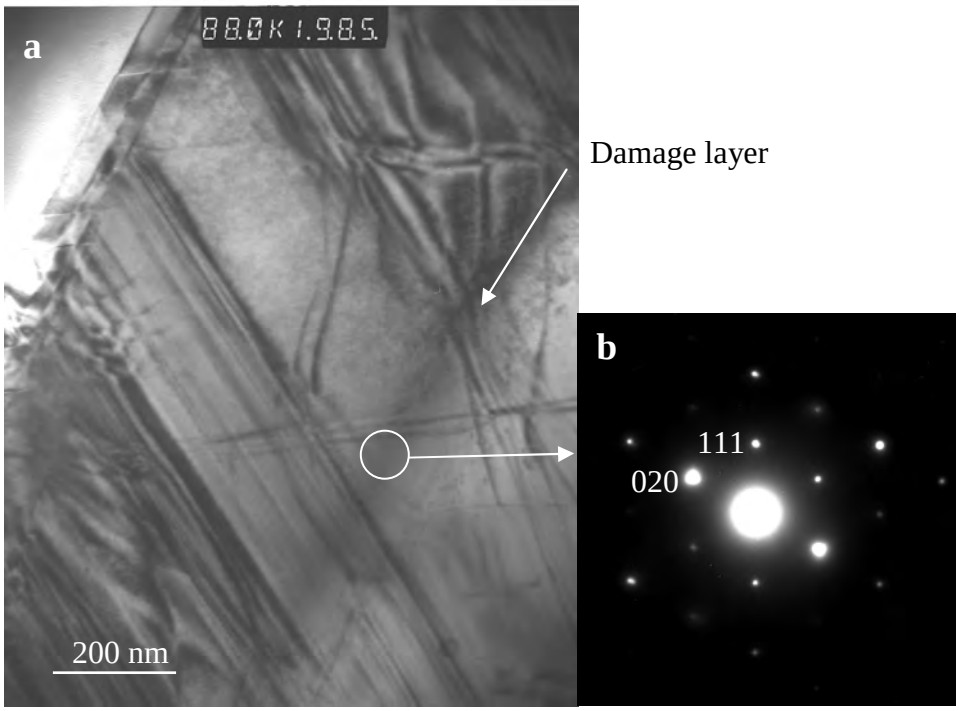

Fig. 6.9. (a) Cross-sectional BF TEM image of unannealed 3C-SiC implanted with 100 keV H^+ ions to a dose of 10^{17} ions/cm^2. No amorphization has taken place as shown by the SAD pattern in (b).

Fig. 6.10 shows a BF TEM image of a void that was presumably grown into the material since it is located some distance away from the implantation damaged region. Voids like these could act as sinks for gas accumulation during annealing.

Fig. 6.10. BF TEM image of a void grown into 3C-SiC.

Fig. 6.11 shows a BF TEM micrograph of the damaged region in H implanted 3C-SiC after annealing at 1000 °C for 20 min in an Ar atmosphere. The TRIM 2008 calculated ion range and vacancy concentration is overlaid for comparison. The agreement in this case is not as good as with He implanted 6H-SiC but the TRIM calculated range remains a relatively close approximation. A difference of approximately 9 % exists between the observed damage range and that predicted by TRIM. Neethling (1985) observed an 11 % discrepancy between simulated ranges of 300 keV H^+ ions implanted into GaAs using LSS theory and the Boltzmann transport equation (Giles (1983)). The projected range of H determined by SIMS agreed well with the prediction of the Boltzmann equation while the LSS theory underestimated the ion range. TRIM predicted an ion range of 2.46 µm which underestimates the actual range of 2.72 µm by about 9 %. The TRIM predicted range agrees well with the LSS prediction of 2.42 µm obtained by Neethling (1985) (using tables of previously computed values) which is to be expected since it is based on the LSS theory.

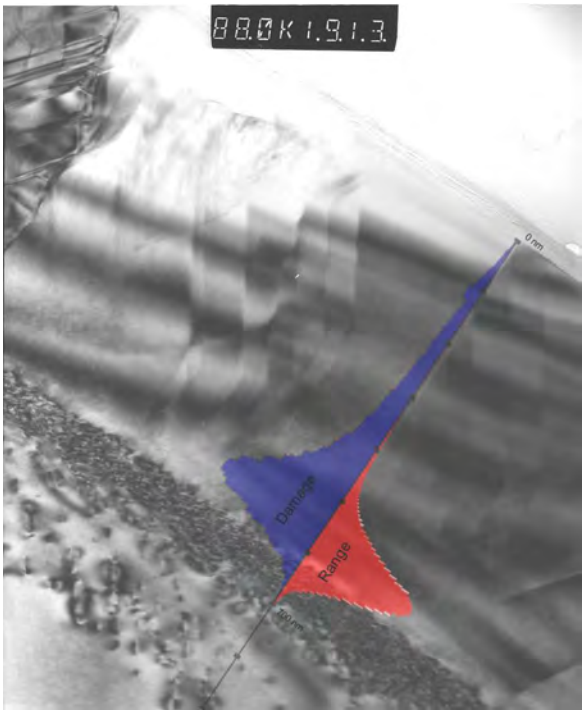

Fig. 6.11. Cross-sectional BF TEM image of 3C-SiC implanted with 100 keV H^+ ions to a dose of 10^{17} ions/cm^2 and annealed for 20 min at 1000 °C in an Ar atmosphere. The TRIM calculated vacancy concentration profile (labelled "Damage") and range plots are superimposed for comparison. Markings on the plot indicate 100 nm.

Higher magnification BF TEM images of the damaged region is shown in Fig. 6.12. The image in Fig. (a) was recorded under kinematical viewing conditions and a crack running along the damage layer is clearly visible along with a number of smaller bubbles on either side of the microcrack. The ion implantation damage is out of contrast in (a) but is clearly visible in the image in (b) taken under a dynamical two-beam viewing condition. By changing the electron diffraction conditions, the defects forming the damage layer can be made visible or invisible.

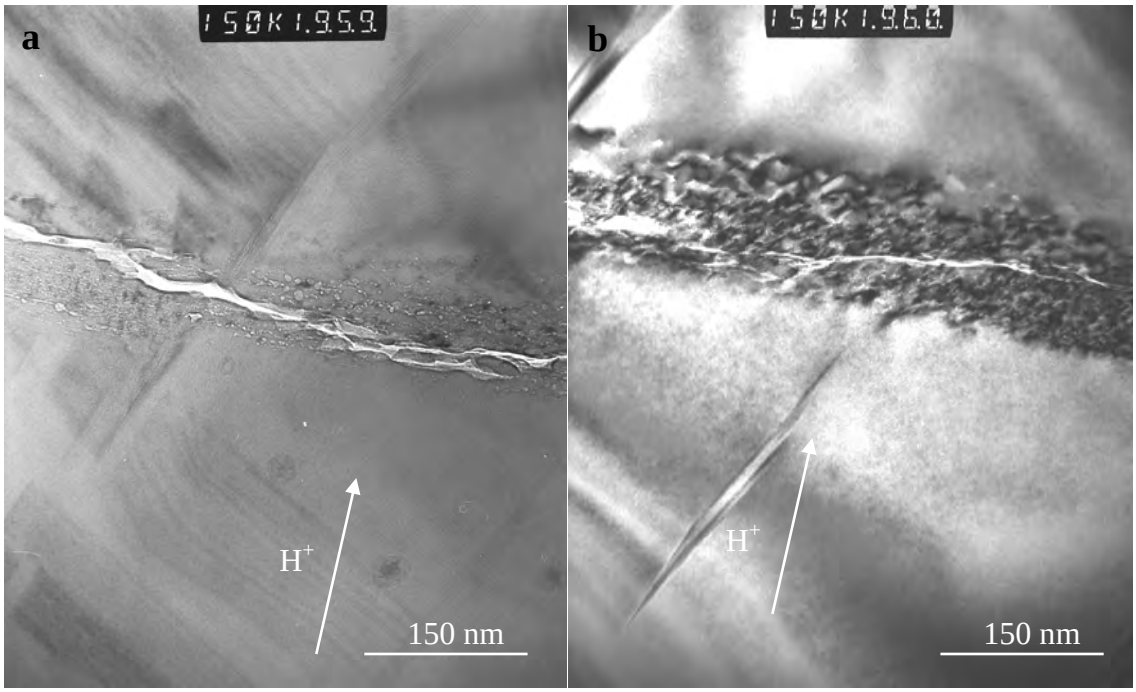

Fig. 6.12. (a) Cross-sectional BF TEM image of long cracks inside the damaged region of H implanted 3C-SiC after post implantation annealing. Small bubbles are still visible adjacent to the crack under kinematical viewing conditions. (b) A nearby area imaged under dynamical conditions clearly shows the strain contrast from the damaged region surrounding the crack.

Beyond the main damage layer, a second damaged band consisting of closely spaced loop-like defects were observed as shown by the black arrows in Fig. 6.13. Based on earlier reports on hydrogen platelets in H implanted GaAs by Neethling *et. al*. (1998) and Kroon *et. al.* (1998), it is suggested that the loop-like defects on {111} planes forming a second damage band in the H implanted SiC are most likely hydrogen platelets. Two-beam strain contrast TEM image calculations, as were reported by

Kroon *et al.* (1998), are however required to distinguish between interstitial loops and hydrogen platelets on {111} planes and this is beyond the scope of this dissertation.

Linnarsson *et al.* (1999) have found that the average diffusion distance of deuterium in 6H-SiC annealed at 600 ºC for 15 min is about 0.6 µm. In this investigation the average distance of the furthest platelet from the peak of projected range (calculated by TRIM) was found to be 375 nm, which is much smaller than the 0.6 µm distance that H can diffuse at 600 ºC during 15 min. Furthermore, the implanted samples in this investigation were annealed at a 1000 ºC for 20 min, which would result in an even higher diffusion distance of H compared to the value measured by Linnarsson *et al*. (1999). The hydrogen is therefore mobile enough during the annealing process to diffuse from the main damaged region deeper into the SiC and precipitate on {111} planes as was observed.

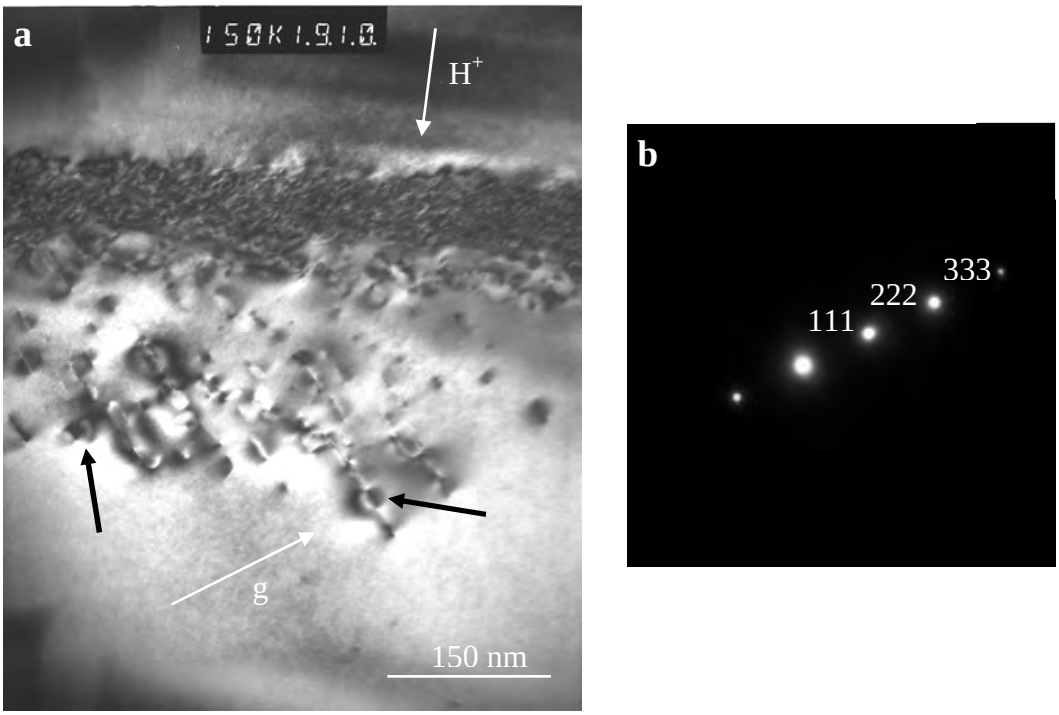

Fig. 6.13. (a) Cross-sectional BF TEM image of hydrogen platelets beyond the main damage layer. The platelets lie on the {111} planes and only those platelets on the (111) planes perpendicular to the operating 111 reflection are visible. (b) Corresponding SAD pattern with electron beam close to the 110 direction.

Fig. 6.14(a) is a BF TEM image of the same H implanted 3C-SiC annealed for 20 min at 1300°C under vacuum in order to increase the average size of the platelets for analysis. The image shows two large platelets viewed edge-on as well as a SAD pattern (b) indicating the orientation of the crystal. The platelet close to the surface does not exhibit the characteristic strain contrast since the foil is too thin.

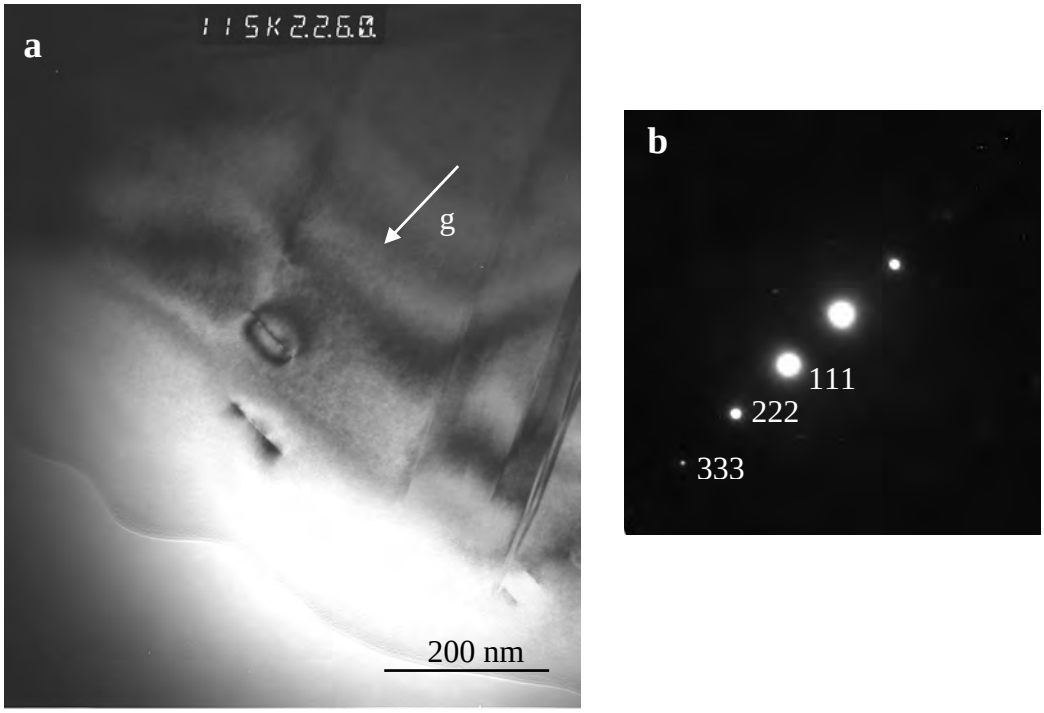

Fig. 6.14. (a) BF TEM image of two large hydrogen platelets seen edge-on after annealing for 20 min at 1300 °C with (b) showing the diffraction condition used.

Fig. 6.15 shows the same platelets viewed from a different direction with opposite sign 202 type $\overline{g}$ vectors and $s > 0$ as indicated by their corresponding SAD patterns. The platelet appears noticeably smaller in (a) than in (b). By employing the method of inside-outside contrast described in chapter 4.2.5, it was concluded that the loop-like defects were of interstitial nature and it was concluded that these loop-like defects are most likely hydrogen-platelets for the reasons given earlier on page 76. For the method of inside-outside contrast, the inclination of the platelets was determined by tilting away from the edge-on orientation.

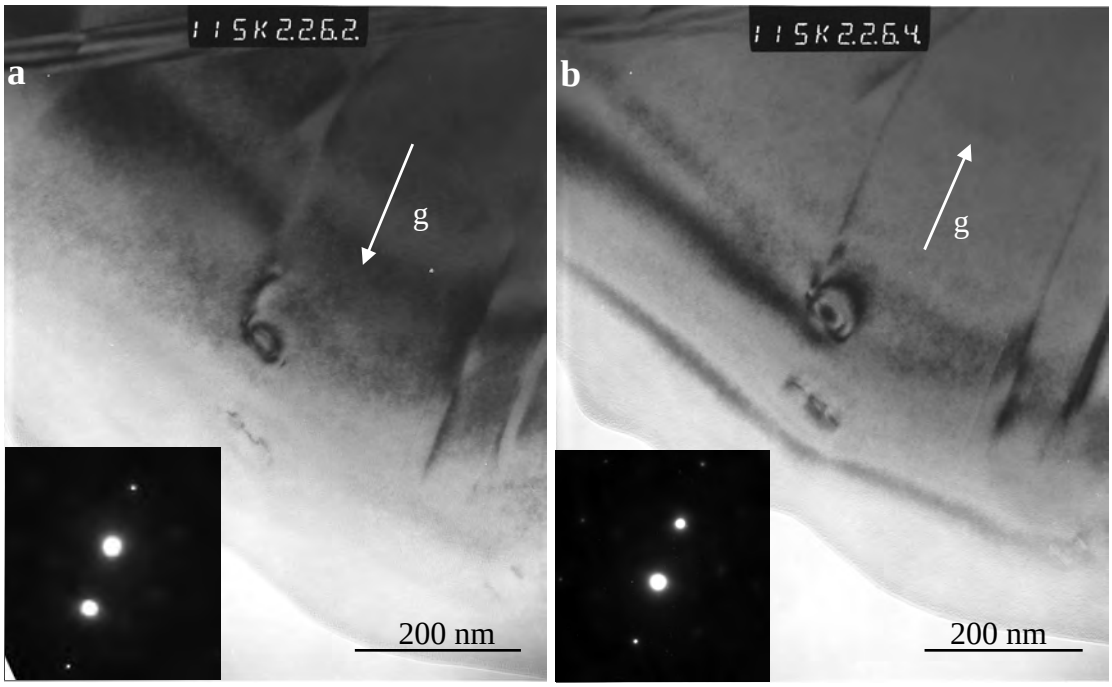

Fig. 6.15. BF TEM images showing an inclined platelet viewed with g = ±202 in (a) and (b). The inset SAD patterns show the operating reflections in (a) and (b).

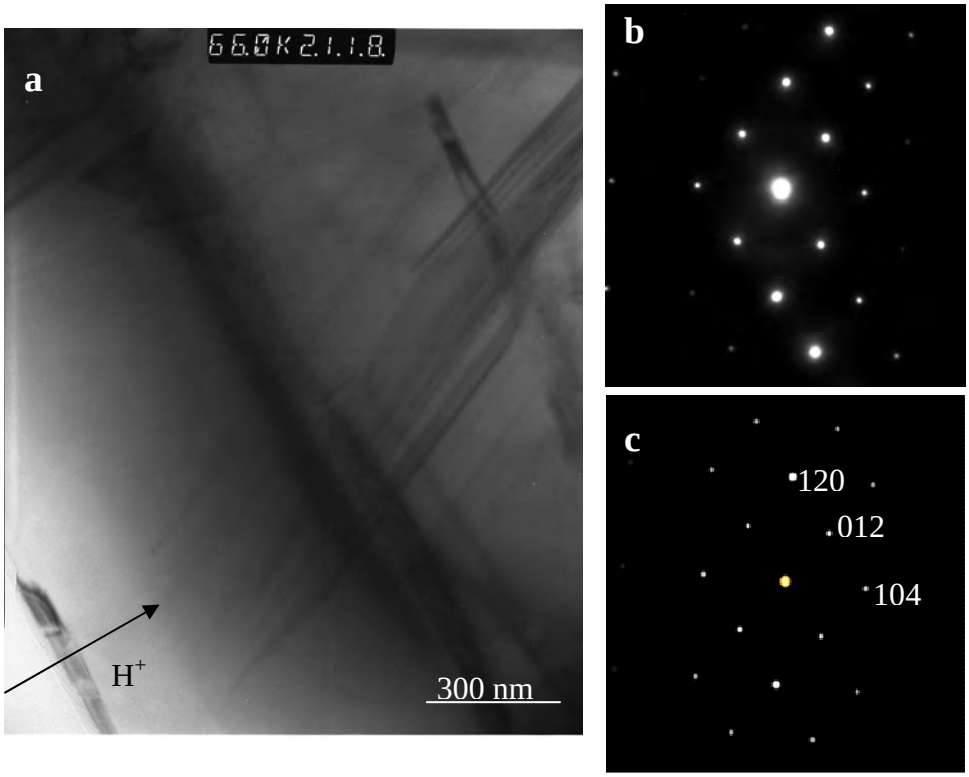

Fig. 6.16. (a) BF TEM image of 4H-SiC grain found in a 3C-SiC specimen. (b) The SAD pattern does not match that of 3C-SiC but rather that of 4H-SiC viewed along a [421] direction (c).

Fig. 6.16(a) shows a BF TEM image of a grain found in the implanted 3C-SiC before annealing where the diffraction pattern (b) does not match any 3C-SiC patterns but rather that of 4H-SiC viewed along a [421] direction as can be seen by comparing the SAD pattern with the simulated pattern in (c). The presence of the 4H-SiC phase in 3C-SiC material is probably due to the low temperature used for the CVD growth (see Chapter 5.2).

6.4 Reaction of Ag and Pd with SiC

Fig. 6.17 shows an optical micrograph of the He implanted 6H-SiC annealed for 67 hours at 1000 °C under vacuum and in contact with a 2:1 by volume mixture of Ag and Pd powder. This ratio was chosen since similar experiments performed previously with 1:1 ratios showed very little Ag in the remaining mixture, possibly due to evaporation at the low pressure. At atmospheric pressure, the melting points of Ag and Pd are 962 °C and 1552 °C respectively but will be significantly lower under high vacuum. As can be seen from the image, the wettability of the SiC surface by the mixture is extremely low and the metal mixture does not adhere to the surface of the SiC.

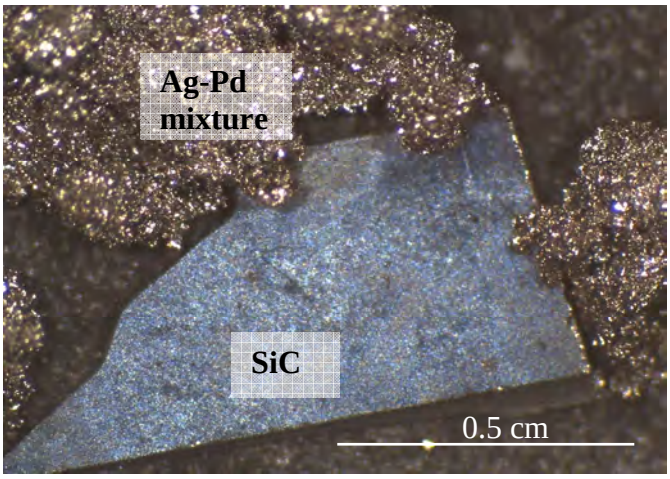

Fig. 6.17. Optical micrograph of He implanted 6H-SiC surface annealed for 67 hours at 1000 °C under vacuum and in contact with a 2:1 by volume mixture of Ag and Pd powder (placed next to specimen for photo).

Fig. 6.18 shows a BSE SEM micrograph of the surface of the above mentioned specimen after annealing. At this magnification small droplets are visible on the surface. The inset shows that at higher magnification the surface appears rough while it had a mirror finish prior to annealing.

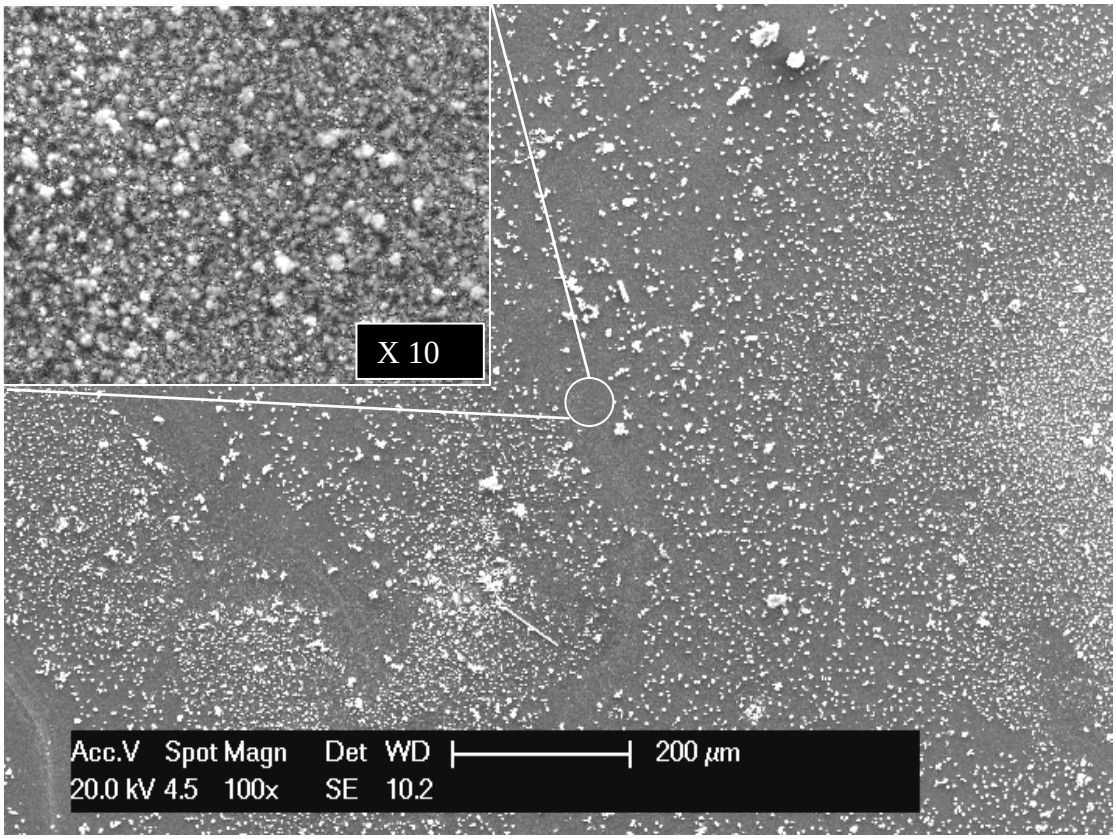

Fig. 6.18. SE SEM image of the surface of He implanted 6H-SiC annealed for 67 hours at 1000 °C under vacuum and in contact with a 2:1 by volume mixture of Ag and Pd powder.

Fig. 6.19 shows a cross-sectional BF TEM micrograph of the SiC/Pd interface. Severe etching of the SiC well beyond the He damaged region is observed. EDX analyses detected no Ag on the surface up to the detection limit of about 0.3 at. %.

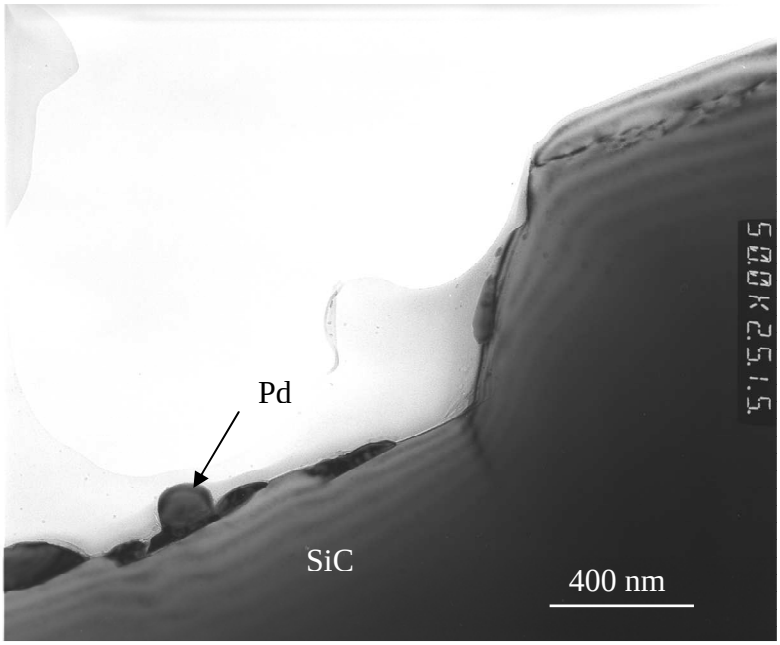

Fig. 6.19. Cross-sectional BF TEM image of the SiC/Pd interface. Severe etching of the SiC surface is visible.

Fig. 6.20 shows a BF TEM micrograph of an inclusion inside the SiC containing Pd. The image at the bottom left is a magnified view of the inclusion showing Moiré fringes running perpendicular to the $\bar{g}$ vector. The spacing between fringes was measured as 1.6 nm ± 0.1 nm.

Using equation 4.10 and a d_{120} spacing of 0.15403 nm for SiC, the interplanar spacing of the inclusion was calculated as 0.171 nm ± 0.001 nm which agrees with the d_{002} spacing of hexagonal Pd_2Si which is 0.17165 nm. Micro-diffraction patterns as well as EDX spectra over the Pd and Ag K lines of the indicated areas are also shown. The K lines were chosen since there is considerable overlap of the Ag and Pd L lines which makes the differentiation between Ag and Pd difficult. No Ag was detected in the inclusion but a Pd concentration of at least 2 at. % was detected. This value is a lower limit since the inclusion represented only a fraction of the total specimen thickness while the electron beam interacted with the entire volume under the illuminated area.

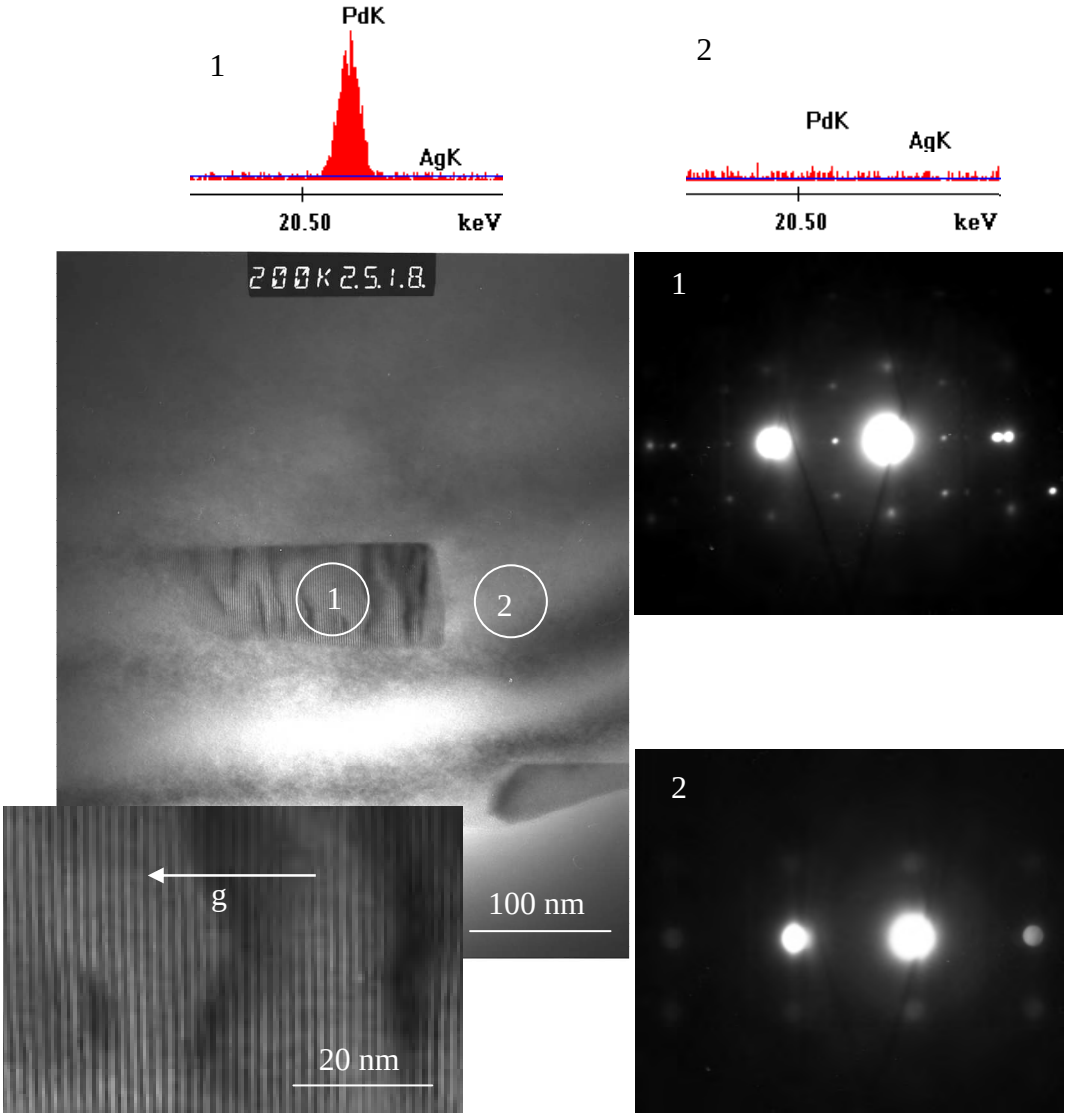

Fig. 6.20. BF TEM image of a Pd_2Si inclusion in 6H-SiC. The inclusion is indicated by (1) and the corresponding microdiffraction patterns of the inclusion (1) and SiC matrix (2) are shown, together with EDX spectra of regions (1) and (2). The Moiré fringes in the inclusion are shown in the inset at higher magnification.

Fig. 6.21 shows the same microdiffraction patterns as well as their simulated counterparts. The pattern in (1) consists of the [210] 6H-SiC pattern, shown in (2) and simulated in (4), with the [210] Pd_2Si pattern simulated in (3) superimposed on it.

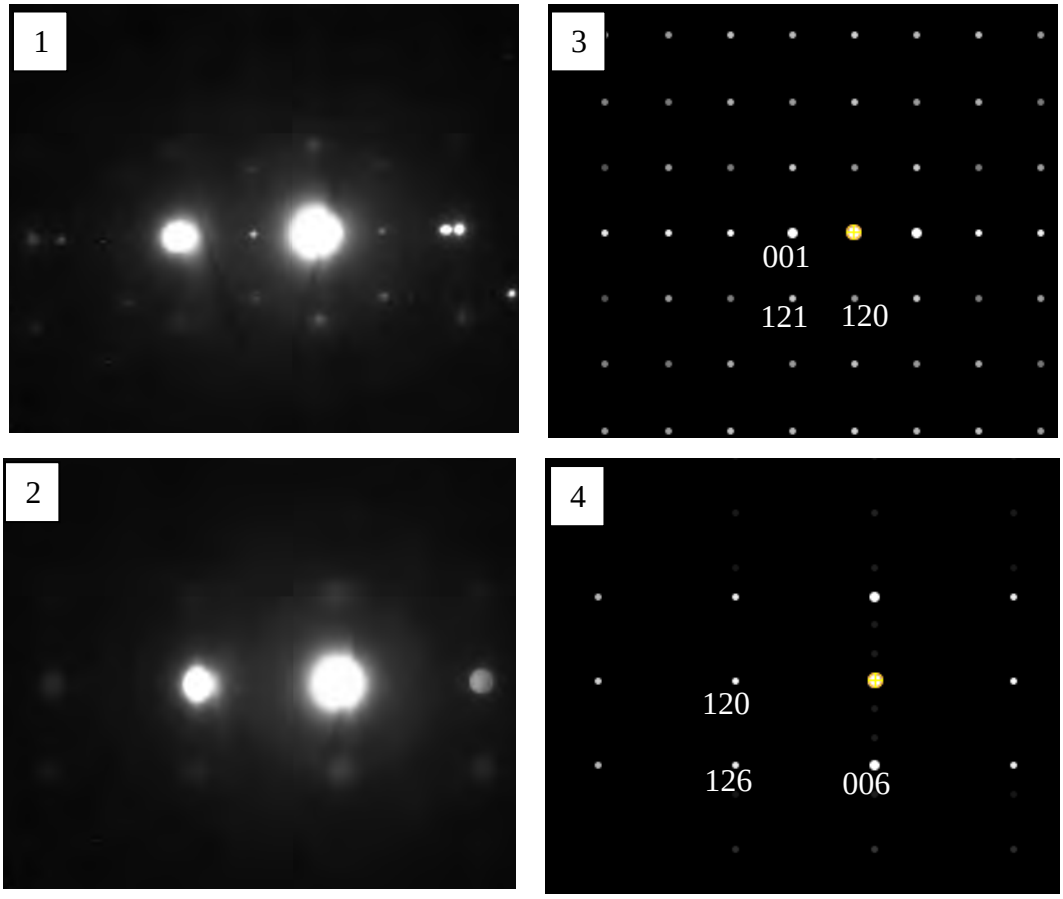

Fig. 6.21. Microdiffraction patterns from the Pd_2Si inclusion (1) and SiC matrix (2) shown in Fig. 6.20 with corresponding simulated patterns (3) and (4) respectively. The extra reflections in (1) matches the simulated diffraction pattern (3) of Pd_2Si viewed along the [210] direction. The microdiffraction pattern (2) matches the simulated diffraction pattern (4) of 6H-SiC with the beam along the [210] direction.

Fig. 6.22 shows an optical micrograph of unimplanted 6H-SiC annealed at 1000 ºC for 67 h under vacuum and in contact with a 2:1 by volume mixture of Ag and Pd. The specimen was placed in the same graphite container and next to an unimplanted 3C-SiC specimen with the same mixture of Ag and Pd on its surface. During annealing the Si substrate of the 3C-SiC dissolved in the Ag-Pd mixture and mixed with the Ag-Pd mixture on the 6H-SiC.

The wettability of the SiC by the Ag-Pd mixture was significantly improved through the absorption of Si into the mixture as can be seen by comparing Fig. 6.22 with Fig. 6.17. All other parameters were kept constant; the specimens were annealed during

the same run in their respective graphite containers. The only difference was the presence of the Si substrate on the 3C-SiC specimen.

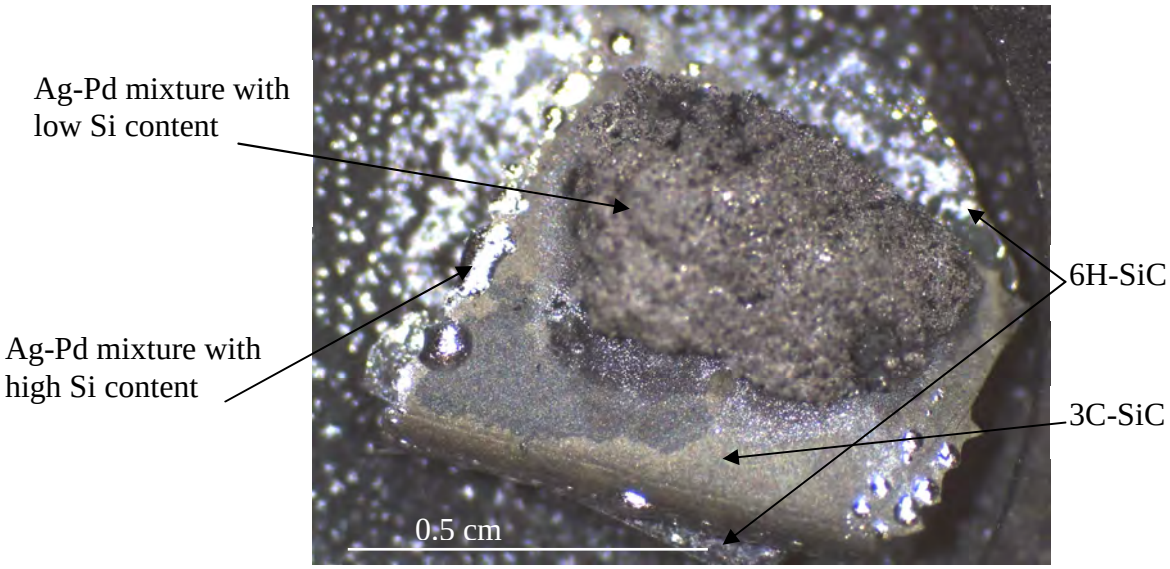

Fig. 6.22. Optical micrograph of 3C-SiC and 6H-SiC annealed for 67 hours in contact with a mixture of Ag and Pd showing a drastic increase in wettability of SiC by the Ag-Pd mixture after addition of Si.

Fig. 6.23(a) shows a high magnification BSE SEM micrograph of the surface of the 6H-SiC shown in Fig. 6.22. Comparing this image with Fig. 6.18, the drastic increase of wettability of SiC by this mixture is evident. The remaining Pd-Ag mixture that is visible on the surface was Ag-rich with an Ag:Pd ratio of about 60:1 atomic.

Fig. 6.23(b) shows a magnified SE SEM image of the region indicated in Fig. 6.23(a). A density of faceted crystals is clearly visible. EDX analysis revealed that these crystals consist of SiC with an atomic concentration ratio of 1:1. Traces of Ag were also found but this was most likely generated by the scattered beam interacting with the surrounding Ag-rich mixture.

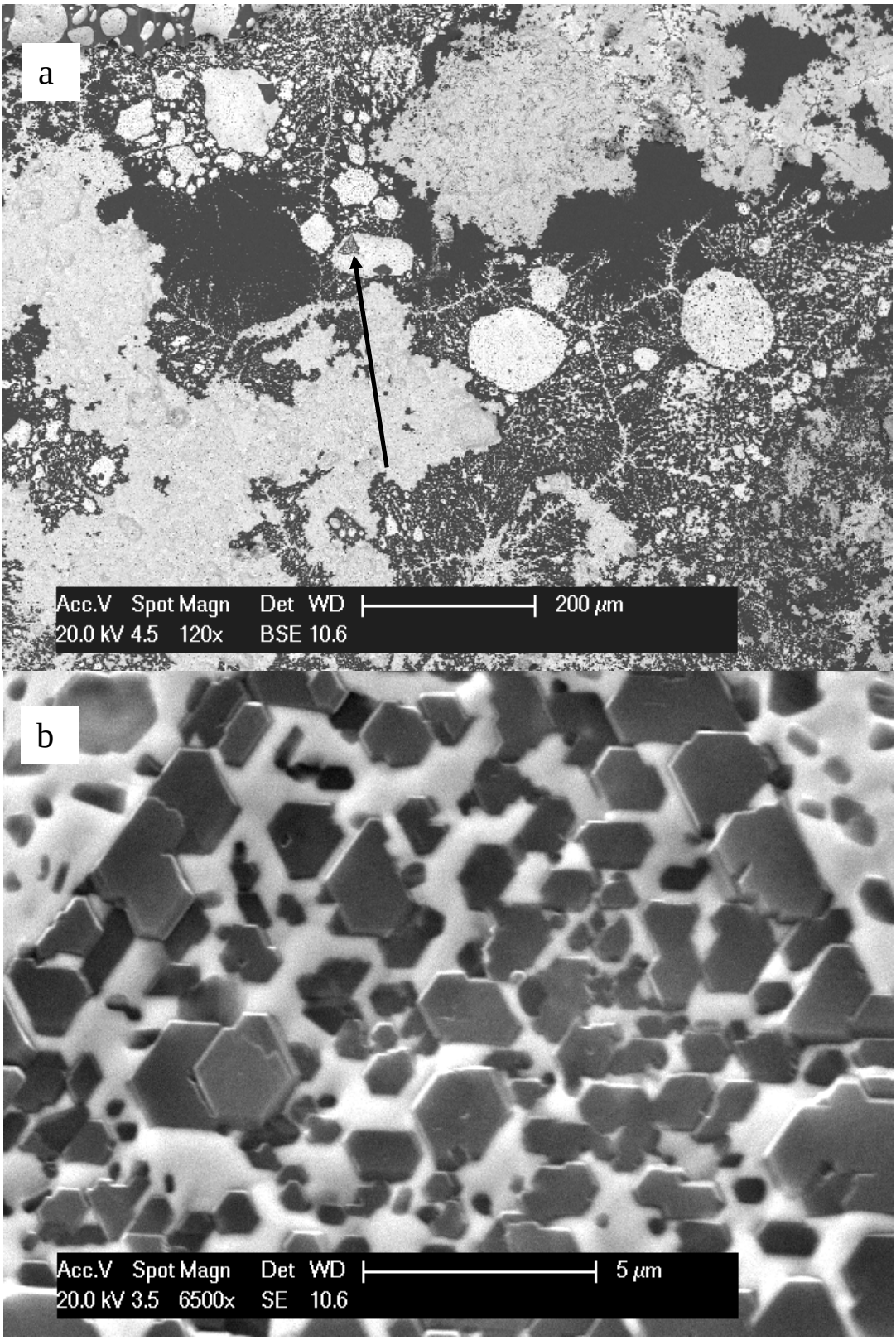

Fig. 6.23. (a) BSE SEM micrograph of the surface of Pd-Ag reacted unimplanted 6H-SiC after annealing for 67 h at 1000 °C. The remaining mixture had an Ag:Pd ratio of about 60:1 atomic. (b) A magnified SE SEM image of the marked area in (a) showing SiC crystals precipitated on top of the Ag-rich drops.

Fig. 6.24 is a BSE SEM image of the surface of the 3C-SiC showed in Fig. 6.22. The same Ag-rich mixture covers the 3C-SiC surface as did the 6H-SiC. The dark spots visible on the larger drops (indicated by the arrow) were of the same composition as the crystals in Fig. 6.23(b).

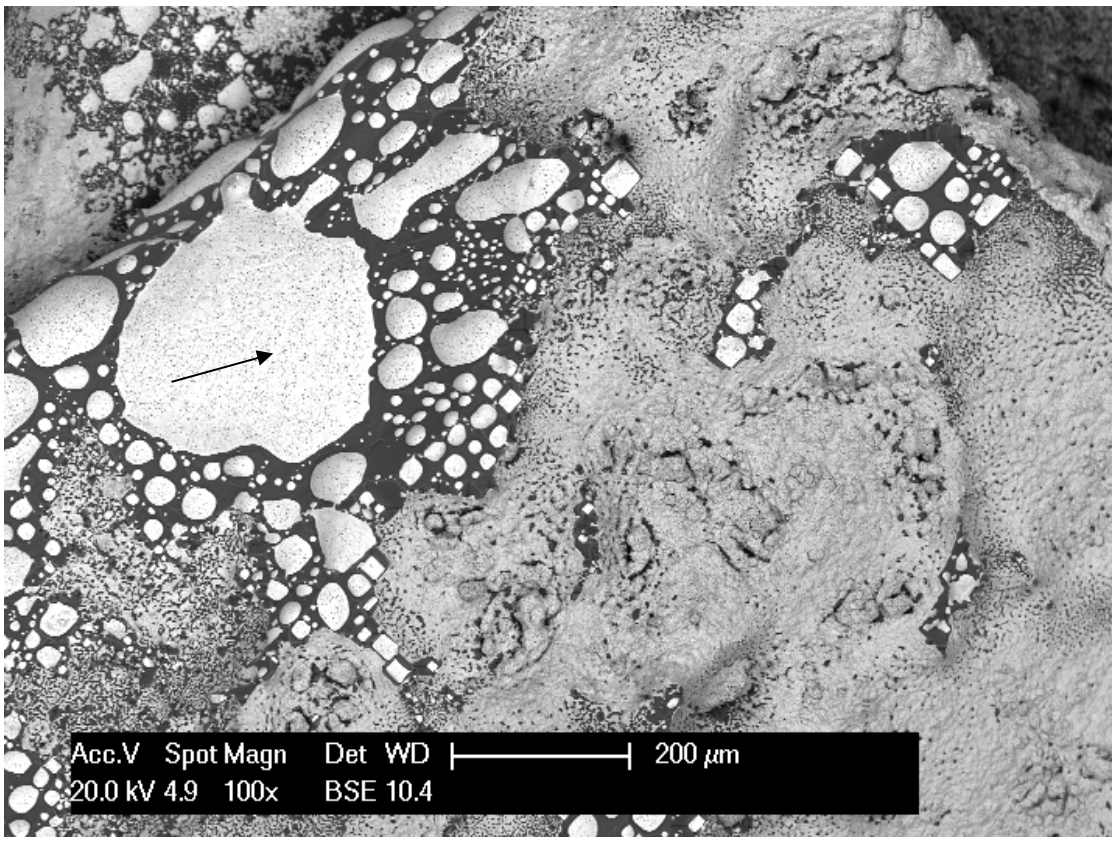

Fig. 6.24. BSE SEM image of the surface of the 3C-SiC showed in Fig. 6.22. The same Ag-rich mixture covers the 3C-SiC surface as did the 6H-SiC.

Fig. 6.25 is a BF TEM micrograph of the interface between 3C-SiC and the Ag-Pd mixture after annealing for 67 h at 1000 ºC under vacuum. EDX analysis showed that the Ag:Pd ratio is about 1:30 for the mixture. The SAD pattern taken over the Ag-Pd mixture (1), matches that of Pd_2Si along a [001] zone axis supporting the observations of Veuillen *et al.* (1999) who found that Pd reacts with SiC to form Pd_2Si on the interface. The SAD pattern taken over the SiC (3) corresponds to that of 4H-SiC viewed along a [001] direction. This was the second observation of the presence of the hexagonal 4H-SiC phase in a mostly 3C-SiC layer. (2) and (4) show simulated SAD patterns of Pd_2Si viewed along a [001] direction and 4H-SiC viewed

along a [001] direction respectively. The inclusion indicated by the arrow was found to contain about 0.5 at. % Pd and 1.5 at. % Ag. These values should be considered as a lower limit instead since the inclusion covered only a fraction of the area illuminated by the electron beam.

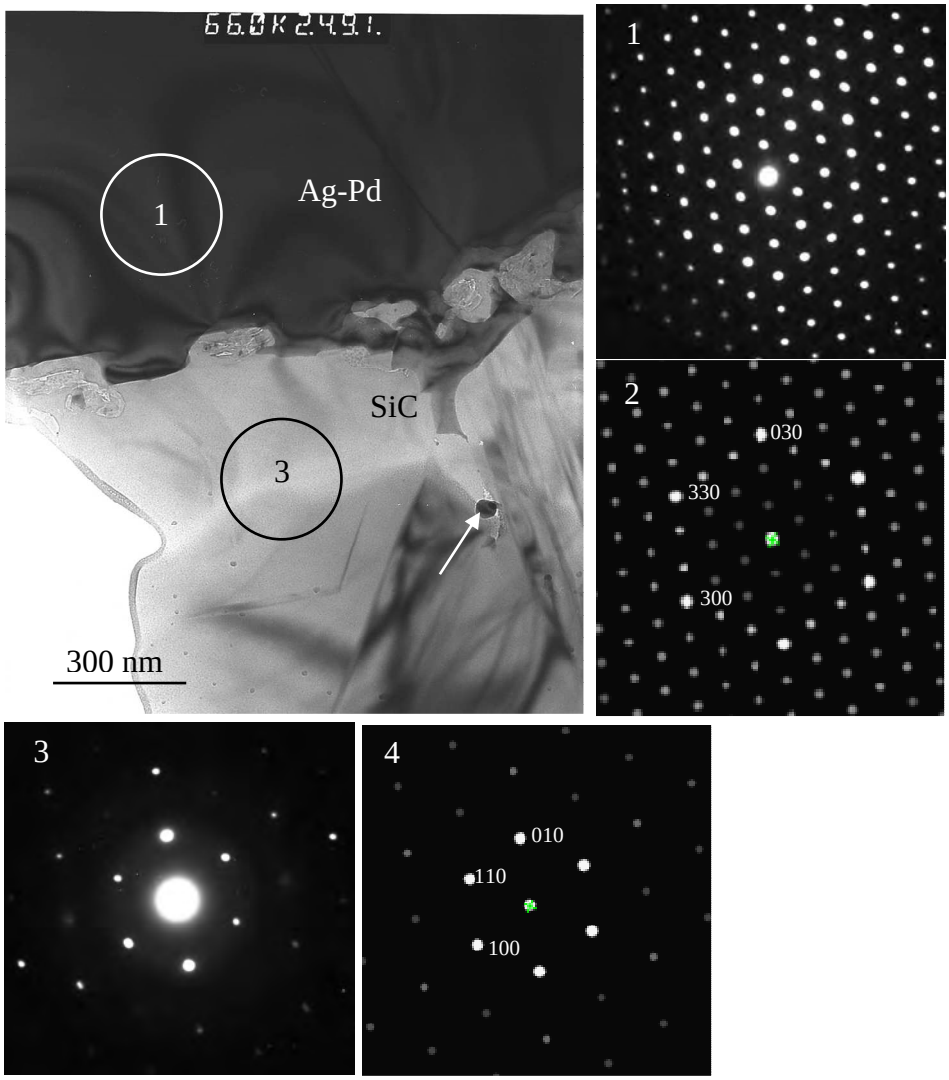

Fig. 6.25. BF TEM micrograph of the Ag-Pd/SiC interface with the associated SAD patterns (1) and (3) as well as their simulated counterparts (2) and (4) respectively. The arrow points to an Ag/Pd containing inclusion.

Fig. 6.26(a-c) shows different Ag and Pd containing nodules that have travelled some distance into the 3C-SiC along grain boundaries.

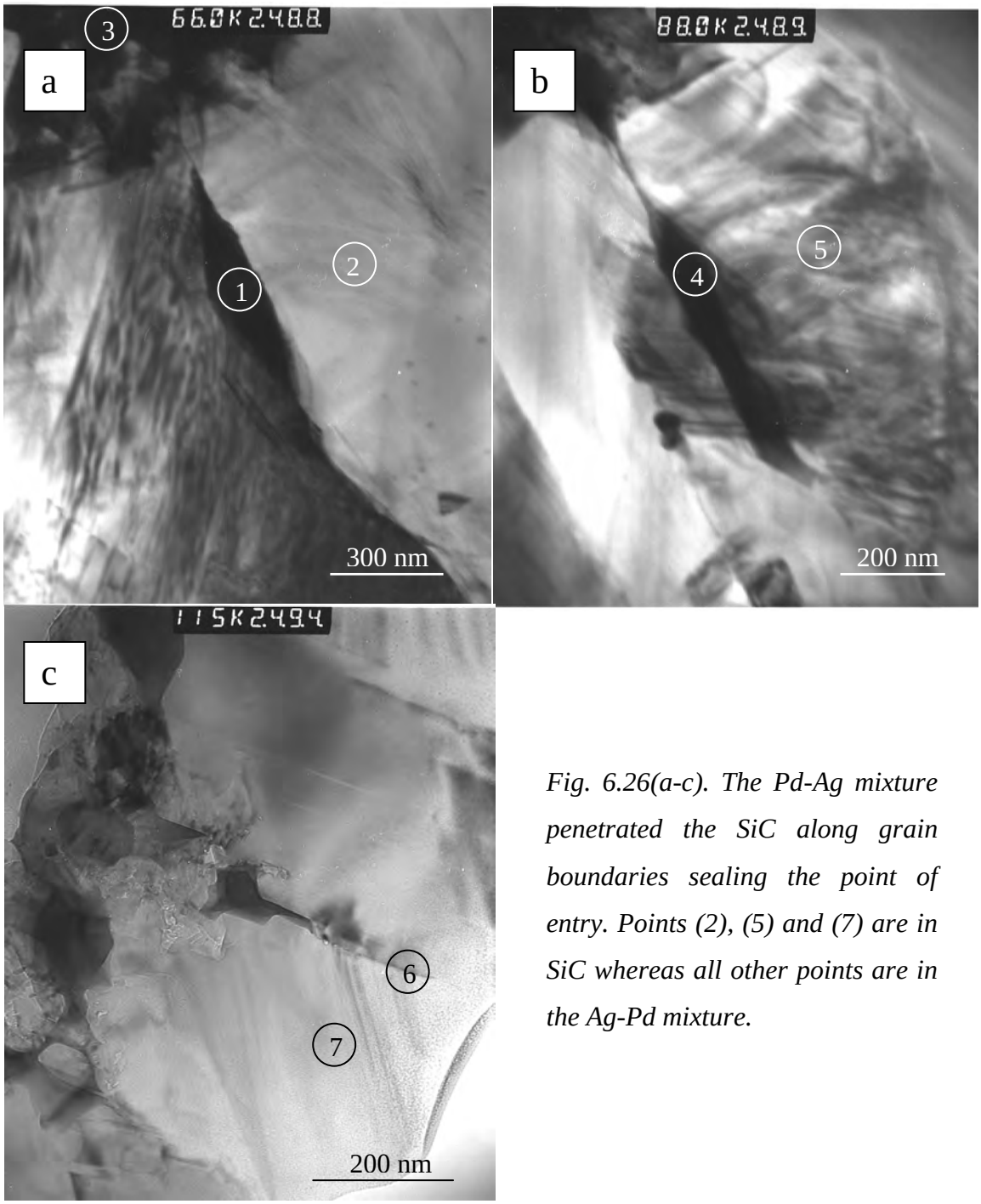

Fig. 6.26(a-c). The Pd-Ag mixture penetrated the SiC along grain boundaries sealing the point of entry. Points (2), (5) and (7) are in SiC whereas all other points are in the Ag-Pd mixture.

It is evident in (a) and (b) that the point of entry has been sealed again suggesting a mechanism of transport similar to that proposed by Pearson *et al.* (1982) where the SiC is dissolved in the metal mixture at the leading edge and recrystallised at the trailing edge in order to seal the point of entry. Further evidence for this mode of

transport is supplied by the observation of SiC crystals on top of Ag and Pd containing drops as mentioned earlier (see Fig. 6.23(b)) which confirms the transport of both Si and C through the metal. The results of EDX analysis of the indicated areas are shown in Table 6.1. Once more it should be stressed that the indicated values are not exact but rather a lower limit since the spot was not small enough to illuminate the nodules only and a considerable area of SiC was illuminated as well.

Table 6.1. Ag and Pd content (in at. %) for the areas numbered in Fig. 6.26.

Area	**1**	**2**	**3**	**4**	**5**	**6**	**7**
Ag	3	0	1	1	0	0	0
Pd	5	0	49	12	0	6	0

Fig. 6.27 shows a BF TEM micrograph of various layers of different composition that formed on top of the SiC close to the interface between the SiC and Ag-Pd-Si mixture. This observation is similar to that reported by Veuillen *et al.* (1999). The EDX spectra for the indicated areas are also shown for the energy range of the Ag and Pd K lines. The intensity scale has been adjusted for each spectrum individually in order to identify the peaks and should thus not be compared. These spectra only serve to confirm the presence of the elements Ag and Pd. The first spectrum (1) had to be scaled substantially in order to recognise the Ag peak. Although quantitative analysis indicated 0.1 at. % Ag, the lower limit for reliable detection by the instrument is normally taken as 0.3 at. % and thus the Ag peak was ignored. It is evident from the spectrum that the Ag peak is not significantly higher than the background. Table 6.2 lists the concentrations of Ag and Pd for the indicated regions.

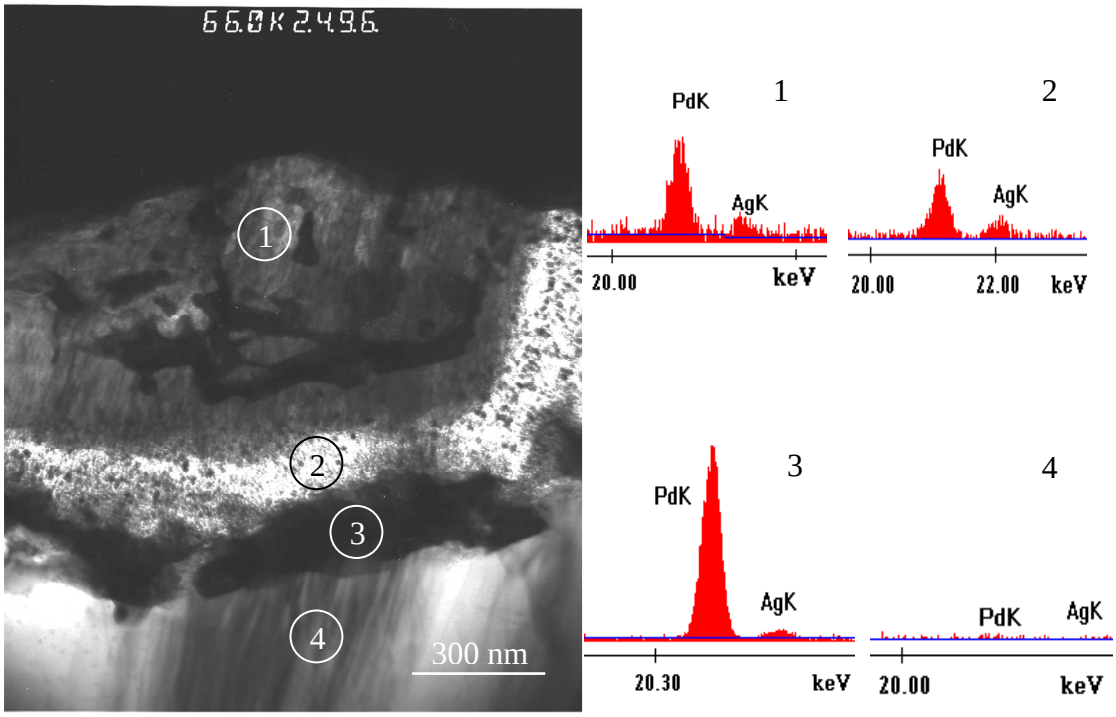

Fig. 6.27. BF TEM image showing various layers of Pd and SiC on the surface of 3C-SiC.

Table 6.2. Ag and Pd content (in at. %) for the areas indicated with numbers in Fig. 6.27.

Area	**1**	**2**	**3**	**4**
Ag	0	0.5	1	0
Pd	1	1	10	0

Fig. 6.28 shows a BSE SEM image of 100 keV H implanted 3C-SiC annealed at 1000 °C for 67 h with a 2:1 by volume mixture of Ag and Pd powder respectively on the surface. Once again the mixture dissolved the Si substrate and the resultant mixture crystallized in two distinct phases with varying concentrations of Ag, Pd and Si.

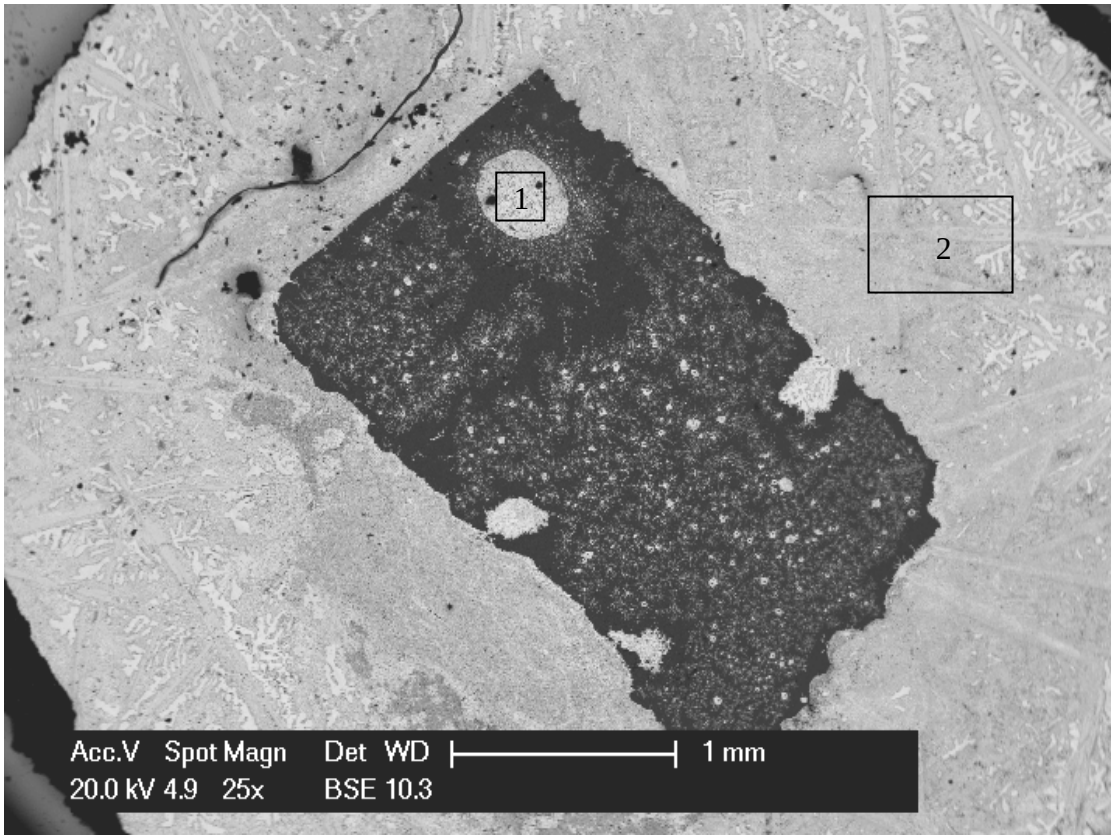

Fig. 6.28. BSE SEM micrograph of H implanted 3C-SiC annealed at 1000 °C for 67 h with a 2:1 by volume mixture of Ag and Pd powder respectively on the surface. The powder dissolved the Si substrate and crystallized in two distinct phases with varying concentrations of Ag, Pd and Si.

Fig. 6.29 is a magnified view of the area indicated by (1) in the above figure. EDX analysis revealed that the dark regions indicated by arrow 1 consist of 43 at. % C, 53 at. % Si, 1 at. % Ag and 3 at. % Pd. The BSE SEM image shows some lighter areas in these dark areas which are believed to be the beginning of SiC formation with excess Si and metal precipitates. These dark areas tend to form inside Ag-rich regions indicated by arrow 2 which has an Ag:Pd ratio of about 50:1 atomic. Large Pd-rich areas indicated by arrow 3 are also visible and the Ag:Pd ratio in these areas were found to be about 1:10.

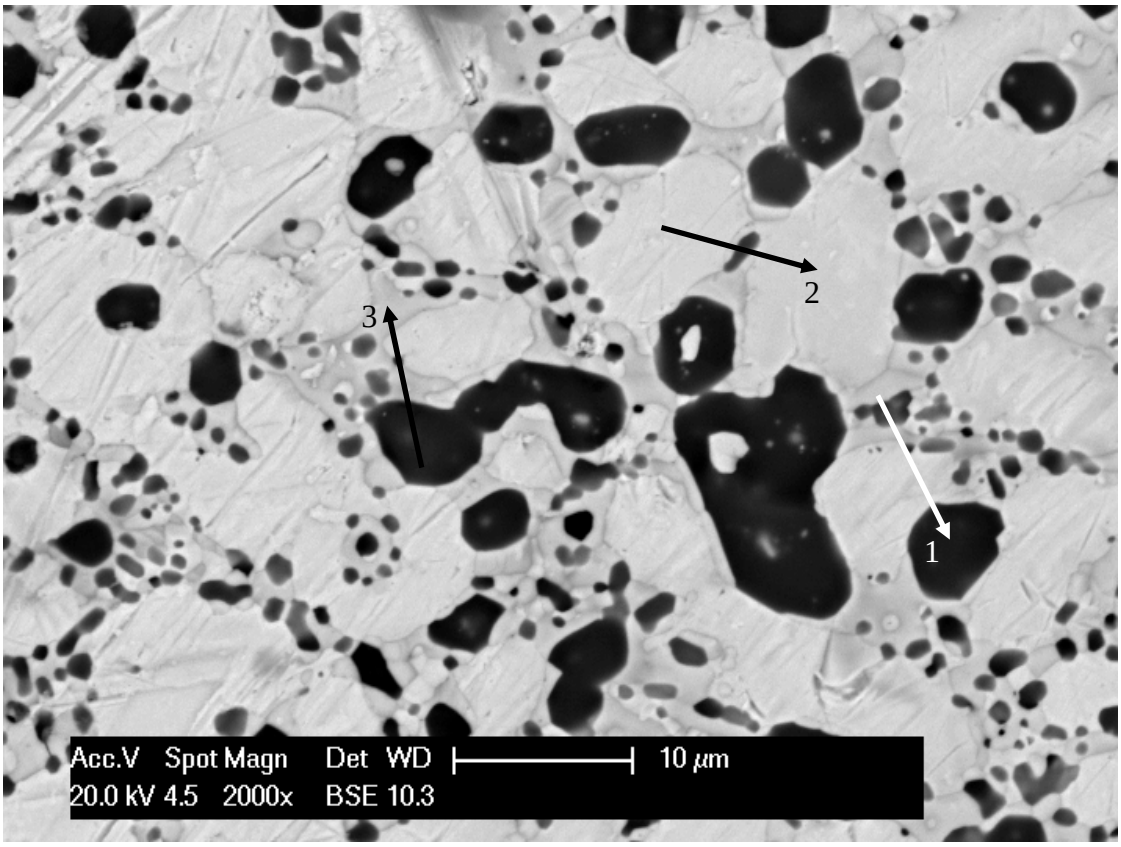

Fig. 6.29. Higher magnification BSE SEM micrograph of the area marked 1 in Fig. 6.28. Two distinct phases with varying concentrations of Ag and Pd is visible as well as a third phase which might well be the onset of SiC crystal nucleation similar to that observed in Fig. 6.23(b).

Fig. 6.30 is a magnified view of the area marked 2 in Fig. 6.28. The Ag-Pd-Si mixture formed a porous phase with a ratio of about 6:1:2 atomic Ag, Pd and Si respectively as well as veins with a 1:6:3 atomic ratio of Ag, Pd and Si respectively.

Fig. 6.31 shows a BF TEM micrograph of interface between 100 keV H implanted 3C-SiC and Si substrate. The substrate has been almost completely dissolved by the Ag-Pd mixture and only sparse nodules of it remain scattered through the mixture. No effect of implantation damage on the reaction of the Ag-Pd mixture with SiC was observed on the opposite surface of the SiC and it was concluded that the free Si was mainly responsible for the interaction between the mixture and the SiC.

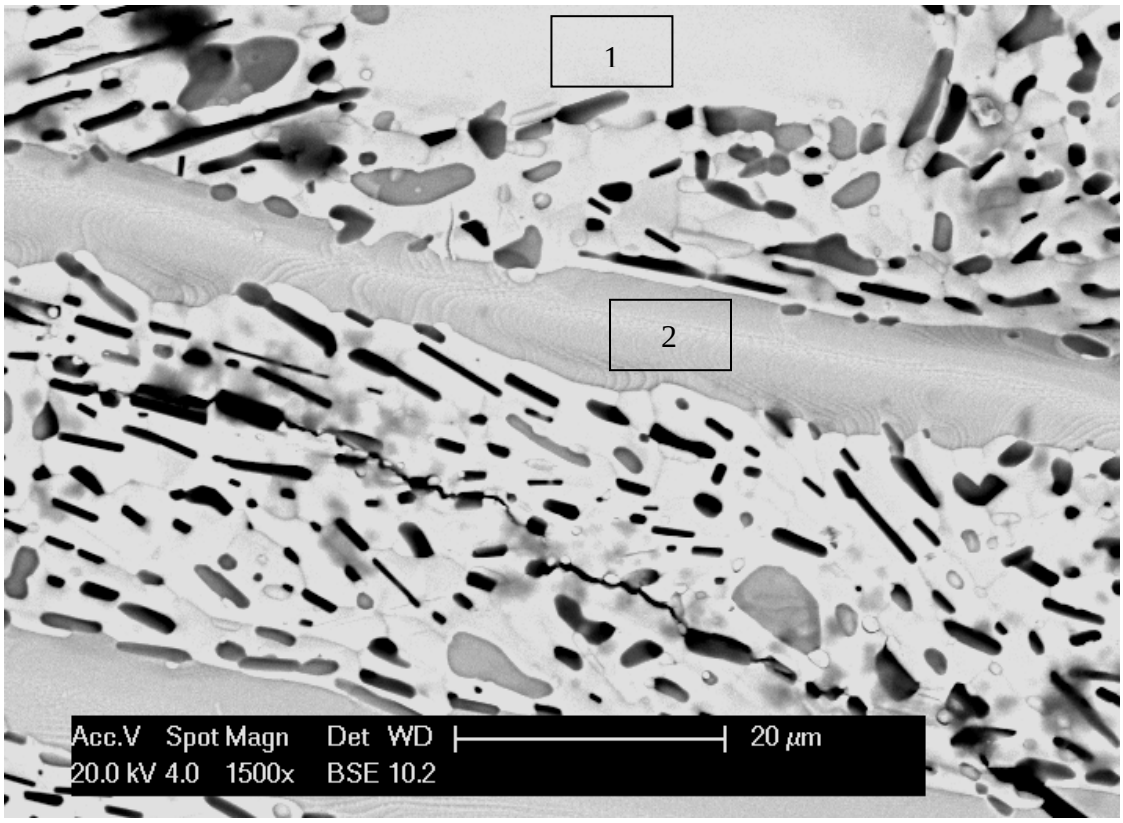

Fig. 6.30. *Higher magnification BSE SEM micrograph of the area marked 2 in Fig. 6.28. Again two distinct phases are visible, one with a high concentration of Ag (1) and the other (2) with a high Pd content.*

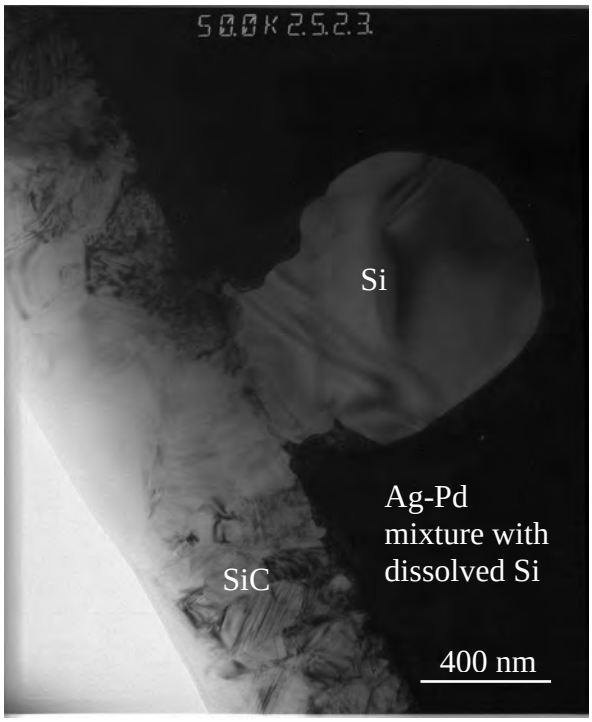

Fig. 6.31. Cross-sectional BF TEM image of the Si substrate which was almost completely dissolved except for some scattered nodules.

6.5 Nanoindentation Hardness Measurements

Nanoindentation hardness measurements were performed using a CSM nano-indentation hardness tester shown in Fig. 6.32. The device also has an AFM attachment as well as an optical microscope for locating the desired area to indent and also for post indentation direct observation of the indents.

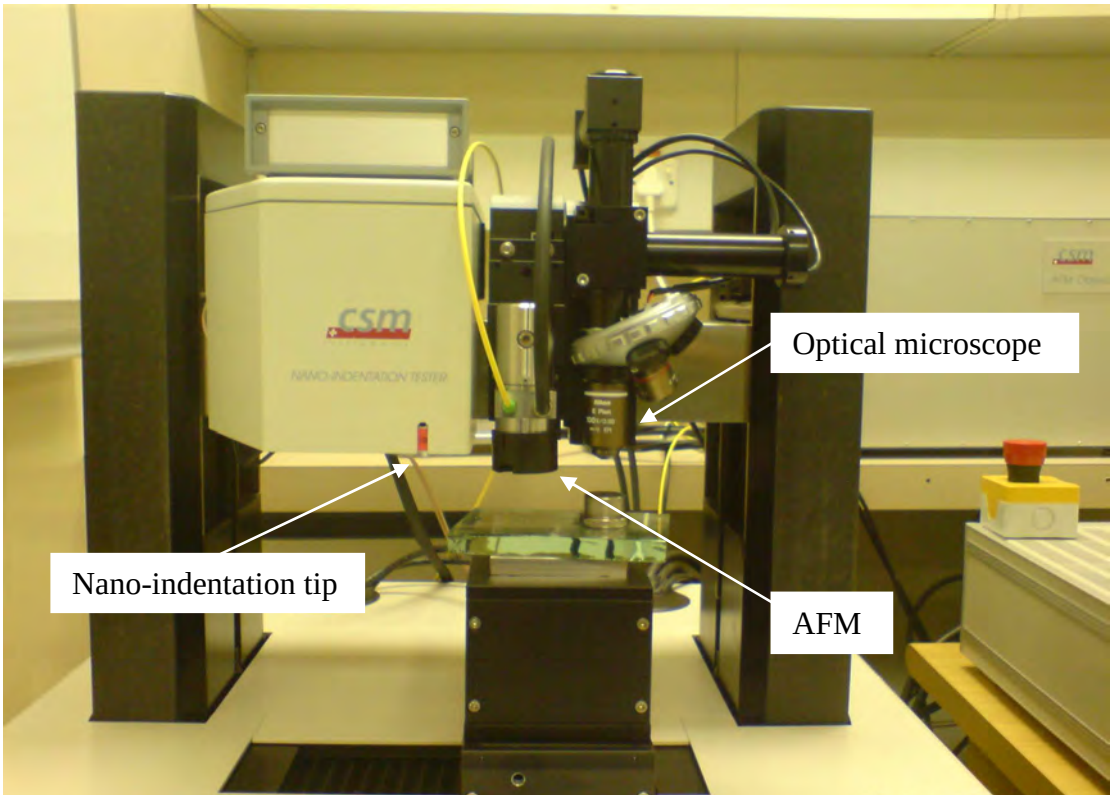

Fig. 6.32. CSM nanoindentation tester with AFM and optical microscope.

Indentations were performed in sets of nine indentations in a regular 3x3 grid with individual indents spaced about 10 µm apart to prevent indents affecting each other. Indents were performed at depths of 100 nm up to 500 nm in steps of 50 nm in order to obtain a depth resolved hardness curve for both implanted and virgin specimens. For each indent the loading and unloading rates were kept constant at 100 mN per minute each. When the desired depth was achieved the load was maintained for a further 15 seconds before unloading. Force and penetration depth was monitored throughout the indentation procedure at a sampling rate of 10 Hz. Fig. 6.33 shows a

plot of the depth resolved nanoindentation hardness measurements (Hit) obtained for the implanted and virgin material.

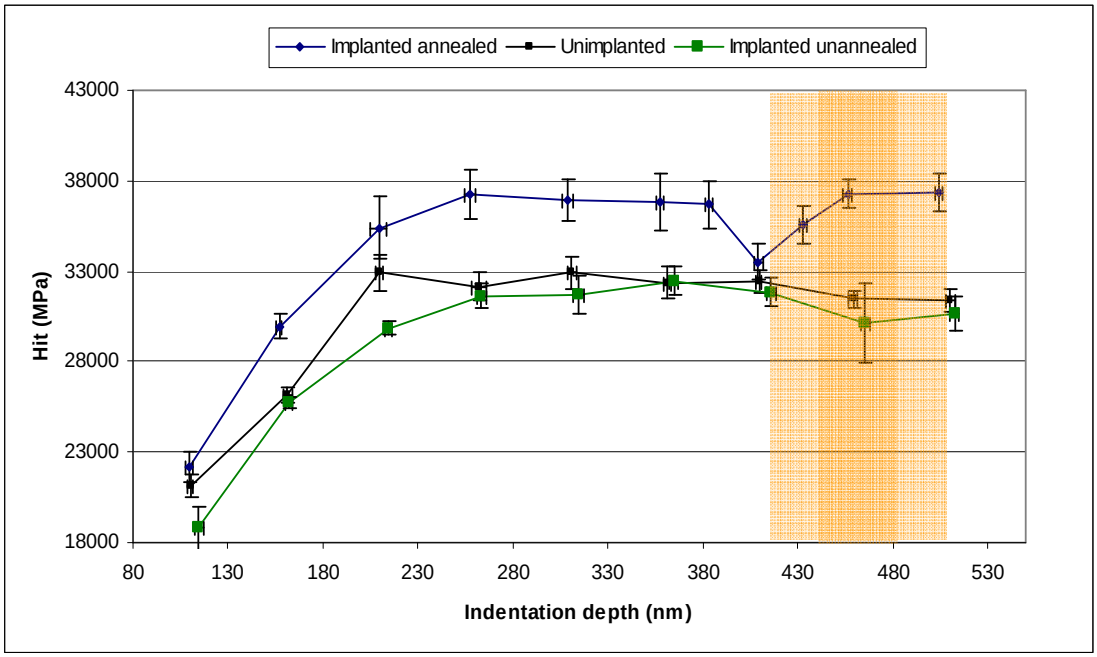

Fig. 6.33. Depth resolved nanohardness measurements for 100 keV He implanted 6H-SiC annealed at 1000 °C for 20 min (blue), unimplanted and annealed (black), implanted but not annealed SiC(green) and the experimentally observed damage distribution (orange shaded region).

The orange shaded region represents the damage distribution obtained from processing a TEM micrograph as explained earlier in the text. Vertical error bars on the indentation data represent the standard deviation of the nine data points collected at each depth, horizontal error bars correspond to the standard deviation of the nine actual measured depths at each chosen depth.

As can clearly be seen from Fig. 6.33, there is a noticeable increase in hardness for the implanted and annealed specimen at all depths. The hardness levels off at approximately 37 GPa and this increase in hardness above that of the unimplanted specimen was ascribed to point defects forming inside the material during implantation. The point defects combine during annealing to form larger defect

structures that inhibit the slipping of the crystal planes, thus reducing the ability of the material to plastically deform. A similar effect was observed for by Park *et al*. (2002) who reported on radiation induced hardening of β-SiC implanted with Si and He, and by Brookes (1992) who reported on reduced plastic deformation of diamonds with low levels of nitrogen impurities inhibiting interplanar slip. The sudden drop in hardness in the implanted sample near the peak of the damaged region was ascribed to the high porosity of the material in this region after annealing due to the formation of He bubbles. Since the plastic deformation front leads the indenter tip by an appreciable amount (Feng *et. al.* (2007)) as can be seen in Fig. 6.34, one would expect the porosity of the damaged region to start influencing the hardness measurements of the material above the damage layer even before the tip of the indenter actually reaches the damaged region. This effect is indeed observed in the measured hardness and is believed to be responsible for the hardness decreasing some distance before the damage peak. For this exact same reason, CSM Instruments recommend not to indent deeper than 10% of the layer thickness when making nanoindentation hardness measurements on thin films on substrates in order to avoid substrate effects on the measured values.

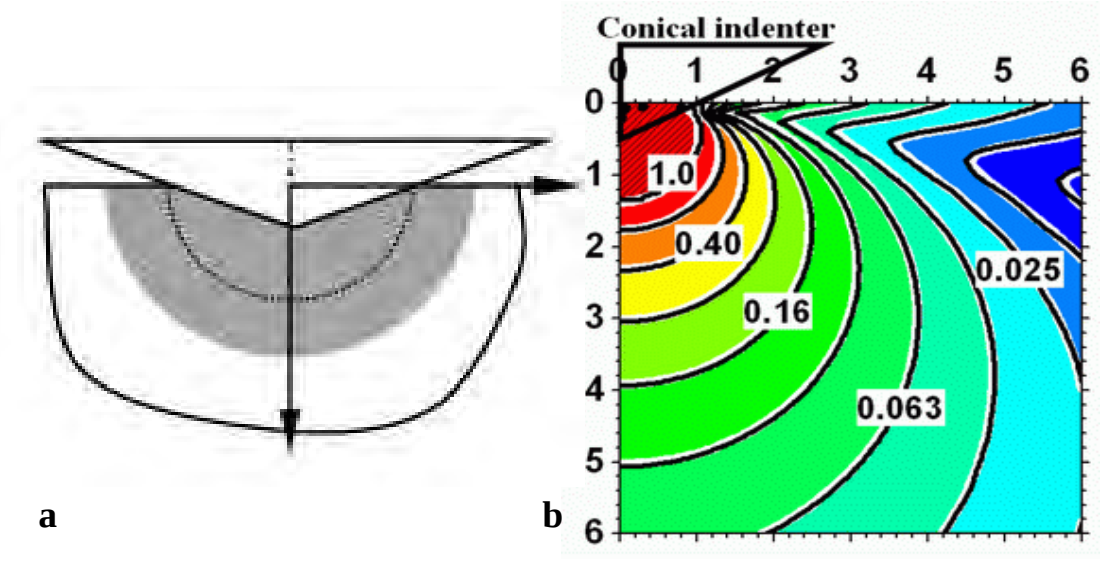

Fig. 6.34. (a) The region of plastic (shaded) and elastic deformation around the indenter tip. (b) The result of theoretical von Mises stress/yield strength calculations by Feng et. al. (2007) In this image, the indenter tip is assumed to be at the top left corner of the image.

Fig. 6.35 and Fig. 6.36 show two situations where nanoindentation hardness measurements are made on a thin film on a substrate. In each case the indentation is performed much deeper than the recommended 10 % of the film thickness and the corresponding hardness versus indentation depth/film thickness plots are shown next to each illustration. In Fig. 6.35, the film is composed of a softer material than the substrate. From the hardness versus depth plot it is evident that a higher hardness than that of the film is obtained as the tip approaches the interface between the film and substrate and some deformation of the substrate start to occur.

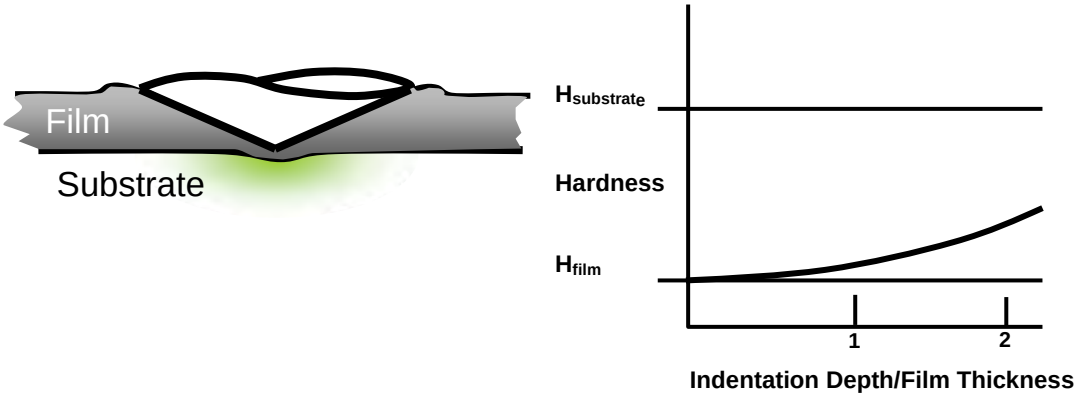

Fig. 6.35. Indentation performed on a soft film on a hard substrate (CSM instruments presentation).

Fig. 6.36 shows the reverse situation where the film is composed of a harder material than the substrate. Again, as the tip approaches the interface between the film and substrate and the region of plastic deformation extends into the substrate, the hardness markedly differs from that of the film and quickly approached that of the substrate. Also note that the slope in this situation is much steeper than in the above mentioned scenario of a soft film on a hard substrate. The shape of the “dip” observed in the hardness measurements of the implanted SiC sample agrees qualitatively with the two situations mentioned above. As the depth approaches that of the bubble filled peak damaged region there is a sudden drop in measured hardness as the porous bubble filled region plastically deforms much more readily than the denser, bubble free region above it. The steep drop in hardness corresponds to the steep slope in the

hardness versus depth curve of the hard film on the soft substrate illustrated in Fig. 6.36. As the indentation depth increases further, the hardness increases once again but the slope is not as steep as the initial drop. This region corresponds to the situation depicted in Fig. 6.35 where the indentation is made through a soft film on a harder substrate as the porous region acts like a soft film on the harder, denser region below it.

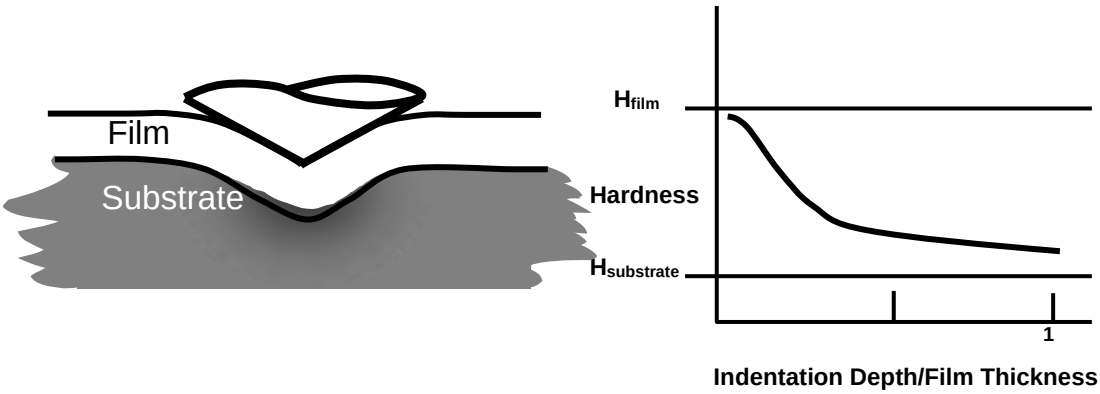

Fig. 6.36. Indentation performed on a hard film on a soft substrate (CSM instruments presentation).

A slight drop in hardness for the implanted, unannealed specimen was observed near the peak of the implantation damaged region although it was not nearly as pronounced as for the annealed specimen where bubble formation has taken place. It may however be possible that small voids are already present in this region before annealing but because of their small size they are not resolvable by TEM.

The hardness versus depth curves of the unannealed implanted specimen and the unimplanted specimen are very close and levels out at about 31 GPa and 32 GPa respectively. This could be because the point defects created during the implantation have not yet migrated sufficiently through the material to form defect clusters and the scattered defects are not effective in preventing interplanar slip of the crystal. The hardness obtained for the unimplanted specimen agrees with the hardness of 32 GPa obtained by Ling (2001) for (0001) orientated 6H-SiC demonstrating the reproducibility of measurements made with nanoindentation.

CHAPTER SEVEN

CONCLUSIONS

7.1 Ion Ranges

The range of the main damaged regions visible in TEM for both the H implanted 3C-SiC and He implanted 6H-SiC agree closely with the TRIM 2008 predicted ion ranges using the Kinchen and Pease model. The He implanted 6H-SiC specimen range agreed more closely with the theoretical predictions possibly since the protons implanted into the 3C-SiC specimens represented the extreme limit of small stopping cross section leading to an underestimation of the ion range by TRIM.

7.2 He Implanted 6H-SiC

No amorphization of the SiC was observed suggesting that some specimen heating occurred during implantation. Before annealing strong contrast is visible in the damaged region but the individual features are too small to be resolved. After annealing at 1000 °C for 20 min in an Ar atmosphere small bubbles can be resolved in the damaged region under kinematical diffraction conditions while dynamical diffraction conditions reveal a high density of strain contrast images of lattice defects, including resolvable gas filled platelets throughout the damaged region. No evidence of exfoliation or crack formation in the damage region was observed.

7.3 H Implanted 3C-SiC

No amorphization of the SiC was expected under H irradiation and none was observed during subsequent analysis. Faint contrast was visible in the damaged region prior to annealing but again no detail could be resolved. It is believed that the contrast is due to a high density of point defects produced in the damaged region. After annealing at 1000 °C for 20 min in an Ar atmosphere significant cracking was observed in the damaged region although no exfoliation took place. Small bubbles were visible on either side of the cracks throughout the damaged region. Under dynamical diffraction conditions a high density of extended defects were observed throughout the damaged region as well as an area beyond the main damaged region which had a high density of hydrogen platelets. Some voids in the SiC structure were also observed and were presumably grown into the material since they are located some distance away from the implantation damage. Analysis of SAD patterns from the 3C-SiC specimen revealed the presence of a second phase namely that of hexagonal 4H-SiC in two grains.

7.4 Reaction of Ag and Pd with SiC

The wettability of the surface of 6H-SiC by a 2:1 by volume ratio of Ag and Pd at 1000 °C was found to be extremely low with very little metal adhering to the surface after annealing for 67 hours. TEM analysis revealed severe etching of the surface by small islands of Pd remaining on the surface. No Ag was detected on the surface up to the detection limit of 0.3 at. %. An epitaxially orientated Pd containing inclusion was found in the SiC and SAD produced a diffraction pattern consistent with that of Pd_2Si. Moiré fringe analysis confirmed a lattice parameter of 0.171 ± 0.001 nm corresponding to that of Pd_2Si.

It was found that the addition of Si to the Ag-Pd mixture (through dissolution of the Si substrate of the 3C-SiC) significantly increased the wettability of both 6H-SiC and 3C-SiC by the mixture. The Si substrate of the 3C-SiC was almost

completely dissolved except for some sub-micron sized nodules that remained dispersed throughout the mixture. An Ag-rich mixture was present on the surface of both the 6H-SiC and the 3C-SiC after annealing with small crystals forming on the surface of the metal drops. The crystals consisted of 1:1 at. % Si and C suggesting that they were indeed SiC crystals however due to the small size of the crystals (<3 µm across) it was not possible to determine the exact phase of these crystals.

It was found that the Ag-Pd-Si mixture migrated along grain boundaries in the 3C-SiC resealing the point of entry as the nodule moves into the material. The presence of Si appears to enhance this process although future studies where the experiment is repeated for different concentrations of Si will be necessary to confirm this.

The metal mixture reacts with the SiC to form layers with different Ag and Pd content along the interface of the SiC and mixture. The upper most layer in contact with the Ag-Pd mixture consisted of SiC containing traces of Pd but no detectable Ag. Below this layer was another with 0.5 at. % Ag and 1 at. % Pd. The last layer before the bulk SiC contained 1 at. % Ag and 10 at. % Pd. This was not a continuous layer however but rather a layer of closely spaced impurity containing globules in the SiC.

No effect of the implantation damage on the interaction of the mixture with the SiC was observed. The He implanted 6H-SiC surface was etched away beyond the damage region by the Pd and thus no conclusion about the possible effect of implantation on the Pd reaction rate with SiC is possible. For the H implanted 3C-SiC most of the mixture reacted with the opposite surface of the SiC where the Si substrate was dissolved and therefore no observations could be made regarding the influence of the implantation damage on the interaction with the metal. Future studies in this area should focus on shorter annealing periods and comparing the depth of interaction for a given time for implanted and virgin SiC. Future studies should also focus on reacting Ag, Pd, Ag-Si, Pd-Si and Ag-Pd separately in an attempt to isolate the element (or combination of elements) responsible for the migration of the mixture into SiC.

7.5 Nanoindentation Hardness Measurements

Nanoindentation hardness values for virgin 6H-SiC and unannealed He implanted 6H-SiC were the same within experimental error. The unannealed implanted specimen exhibited a relatively high standard deviation in hardness as well as a slight decrease in hardness at a depth around 460 nm corresponding to the damaged region. The reduction in hardness could be as a result of small unresolvable He bubbles in this region.

The implanted and annealed specimen exhibited a considerable increase in hardness compared to the other two specimens at around 37 GPa which was attributed to the coalescence of point defects under annealing which inhibit the slipping of atomic planes over each other. It also displayed a marked decrease in hardness around the damaged region and the shape of the graph around this region is indicative of a constrained coating effect where the porous SiC in the damage region plays the role of firstly a soft substrate below a hard coating and secondly of a soft coating on a hard substrate.

REFERENCES

IN ALPHABETICAL ORDER

Audren, A., Benyagoub, A., Thomé, L. and Garrido, F. (2007), Nucl. Inst. and Meth., B 257, 227-230.

Balog, M., Šajgalĭk, P., Hnatko, M., Lenčéš, Z., Manteverde, F., Kečkéš, J. and Huang, J.L. (2005), J. European Ceramic Society, 25, 529-534.

Beaufort, M.F., Oliviero, E., David, M.L., Nomgaudyte, J., Pranevicius, L., Declémy, A. and Barbot, J.F. (2002), Nucl. Inst. and Meth., B 186, 218-222.

Bollmann, W. (1970), Crystal Defects and Crystalline Interfaces, Springer-Verlag, New-York.

Bragg, W.H. (1915), Phil. Mag., 215, 253-274.

Brookes, E.J. (1992), The Plasticity of Diamond, PhD Dissertation, University of Hull.

Carter, G. and Grant, W.A. (1976), Ion Implantation of Semiconductors, Edward Arnold.

Casey, H.C. and Pearson, G.L. (1975), Point Defects in Solids, Vol. 2, Plenum Press, New York.

CSM Instruments Indentation Software User's Guide, Version: R0.0.5 (2006).

De Graef, M. (2003), Introduction to Conventional Transmission Electron Microscopy, Cambridge University Press.

Doerner, M.F. and Nix, W.D. (1986), J. Mater. Res., 1, 601-609.

Edington, J.W. (1975), Interpretation of Transmission Electron Micrographs, Practical Electron Microscopy in Materials Science, Monograph Three, Macmillan Phillips Technical Library.

Fedina, L.I. and Aseev, A.L. (1986), Phys. Stat. Sol., (a) 95, 517.

Feng, G., Qu, S., Huang, Y. and Nix, W.D. (2007), Acta Materialia v.55, 2929-2938.

Fisher, G.R. and Barnes, P. (1990), Philos. Mag. B 61, 217.

Frangis, N., Van Landuyt, J., Grimaldi, M.G. and Calcagno, L. (1996), Nucl. Inst. and Meth., B 120, 186-189.

Giles, M.D., and Gibbons, J.F. (1983), Nucl. Instr. And Meth., 33, 209-210.

Girifalco, L.A. (1964), Atomic Migration in Crystals, Blaisdell publishing company, New York.

Goldstein, J.I., Newbury, D.E., Echlin, P., Joy, D.C., Romig, A.D., Jr., Lyman, C.E., Fiori, C. and Lifshin, E. (1992), Scanning Electron Microscopy and X-Ray Microanalysis, Second Edition, Plenum Press, New York.

Griffiths, L.B. (1966). J. Phys. Chem. Solids, 27, 257.

Hasegawa, A., Saito, M., Nogami, S., Abe, K., Jones, R.H. and Takahashi, H. (1999), J. Nucl. Mater., 246, 355-358.

Heinisch, H.L., Greenwood, L.R., Weber, W.J. and Willford, R.E. (2004), J. Nucl. Mater., 327, 175-181.

Heinrich, K.F.J. (1966), Proc. 4th Int. Conf. on X-ray Optics and Microanalysis, Hermann, Paris, p. 159.

Helary, D., Dugne, O., Bourrat, X., Jouneau, P.H. and Cellier, F. (2006), J. Nucl. Mater., 350, 332-335.

Hirsch, P.B., Howie, A., Nicholson, R.B., Whelan, M.J. and Pashley, D.W. (1965), Electron Microscopy of Thin Crystals, Butterworths, London.

Hirth, J.P. and Lothe, J. (1986), Theory of Dislocations, McGraw-Hill, New-York.

Hull, D. and Bacon, D.J. (1984), Introduction to Dislocations, 3rd Edition, Volume 37, Butterworth Heinemann

Iwami, M. (2001), Nucl. Inst.. and Meth., A 466, 406.

Jepps, N.W. and Page, T.F. (1983), J. Cryst. Growth Charact., 7, 259.

Kelly, B.T. (1966), Irradiation Damage to Solids, Pergamon Press, Oxford.

Kinchen, G.H. and Pease, R.S. (1955), Reports on Progress in Physics, 18, 1.

Kittel, C. (1976), Introduction to Solid State Physics, Wiley, New-York

Knippenberg, W.F. (1963), Philips Research Reports, 18, No. 3, 161-274

Kordina, O. (1994), Linköping Studies in Science and Technology, Dissertations. No. 352, Linköping University.

Kroon, R.E. and Neethling, J.H. (1998), Proc. 14th Int. Congr. Electron Micros, Cancum, Vol. 3, 451-452.

Lebedev, O.I., Van Tendeloo, G., Suvorova, A.A., Usov, I.O. and Suvorov, A.V. (1997), J. Electron Microscopy, 46(4), 271-279.

Li, J.G. (1994), Materials Letters, 19, 291-298.

Ling, Y. (2001), Low-Damage Grinding/Polishing of Silicon Carbide Surfaces, SIMTech Technical Report (PT/01/001/PM).

Linnarsson, M.K., Janson, M.S., Karlsson, S., Schöner, A., Nordell, N. and Svensson, B.G. (1999), Materials Science and Engineering, B61-62, 275-280.

MacLean, H.J. (2004), Silver Transport in CVD Silicon Carbide, Ph.D. Thesis, MIT, Department of Nuclear Engineering.

MacLean, H.J., Ballinger, R.G., Kolaya, L.E., Simonson, S.A., Lewis, N. and Hanson, M.E. (2006), J. Nucl. Mater., 357, 31-47.

McDonnel Douglas Aerospace Team. (1992), Inertial Fusion Energy Reactor Design Studies – Final Report, Vol. I, II and III, DOE/ER-54101 MDC92E0008.

Minato, K., Ogawa, T., Fukuda, K., Sekino, H., Miyanishi, H., Kado, S. and Takahashi, I. (1993), J. Nucl. Mater., 202, 47-53.

Nabielek, H., Brown. P.E. and Offermann, P. (1977), Silver Release from Coated Particle Fuel, Nuclear Technology, Vol. 35.

Nabielek, H., Goodin, D. and Scheffel, W. (2001), Criteria for a High Performance particle, HTR-TH International HTR Fuel Seminar, Brussels, Belgium.

Nagasawa, H., Yagi, K. and Kawahara, T. (2002), J. Crys. Growth, 237-239, 1244-1249.

Nakata, K., Kasahara, S., Shimanuki, S., Katano, Y., Ohno, H. and Kuniya, J. (1991), J. Nucl. Mater., 403, 179-181.

Neethling, J.H. (1980), Radiation Damage in Proton Bombarded Galluim Arsenide, M.Sc. Dissertation, University of Port Elizabeth.

Neethling, J.H. (1985), Radiation Damage in Implanted Galluim Arsenide, Ph.D. Thesis, University of Port Elizabeth.

Neethling, J.H. and Phillipp, F. (1998), Proc. 14th Int. Congr. Electron Micros, Cancum, Vol. 3, 413-414.

Oliver, W.C. and Pharr, G.M. (1992), J. Mat. Res., 7(6), 1564-1583

Oliviero, E., Beaufort, M.F., Pailloux, F. and Barbot, J.F. (2004), Nucl. Inst. and Meth., B 218, 391-395.

Park, K.H., Katoh, Y., Kishimoto, H. and Kohyama, A. (2002), J. Nucl. Mater., 307-311, 1187-1190

Pearson, R.L., Lauf, R.J. and Lindemer, T.B. (1982), The Interaction of Palladium, the Rare Earths and Silver with Silicon Carbide in HTGR Fuel Particles, Oak Ridge National Laboratory, Chemical Technology Division, Contract no. W-7405-eng-26.

Pirouz, P. and Yang, J.W. (1993), Ultramicroscopy 51, 189.

Reuter, W. (1972), Proc. 6th Int. Cong. On X-ray Optics and Microanalysis, University of Tokyo Press, Tokyo, p. 121.

Sasase, M., Ito, Y., Yasuda, K., Ishigami, R., Hatori, S. and Yamamoto, A. (2003), Nucl. Inst. and Meth., B 209, 179-183.

Sawa, K. and Ueta, S. (2004), Nucl. Eng. Design, 233, 163-172.

Seitz, F. and Koehler, J. (1956), Solid State Physics, 2, 305.

Shaffer, P.T.B. (1968), Acta Cryst., B 25, 477.

Snead, L.L., Nozawa, T., Katoh, Y., Byun, T.S., Kondo, S. and Petti, D.A. (2007), J. Nucl. Mater., 371, 329–377

Streitwolf, H.W. (1959), Ann. Phys., Leipzig, 3, 183.

Tong, Q.Y., Gutjahr, K., Hopfe, S., Gösele, U. and Lee, T.H. (1997), App. Phys. Lett., 70, 11.

Tromas, C., Audurier, V., Leclerc, S., Beaufort, M.F., Declémy, A. and Barbot, J.F. (2008), Nucl. Inst. and Meth. (Article in Press).

Veuillen, J.Y., Nguyen Tan, T.A., Tsiaoussis, I., Frangis, N., Brunel, M. and Gunnella, R. (1999), Diamond and Related Materials, 8, 352-356.

Weltner Jr., W. (1969), J. Chem. Phys., 51, 2469.

Williams, D.B. and Carter, C.B. (1996), Transmission Electron Microscopy, Volume 1 Basics, Plenum Press, New York.